Advances in Polymer Technology

Organic-Inorganic Hybrid Polymers: Experiment, Simulation, and Application

Lead Guest Editor: Zhiwei Qiao
Guest Editors: Hong Liang and Yongwei Chen

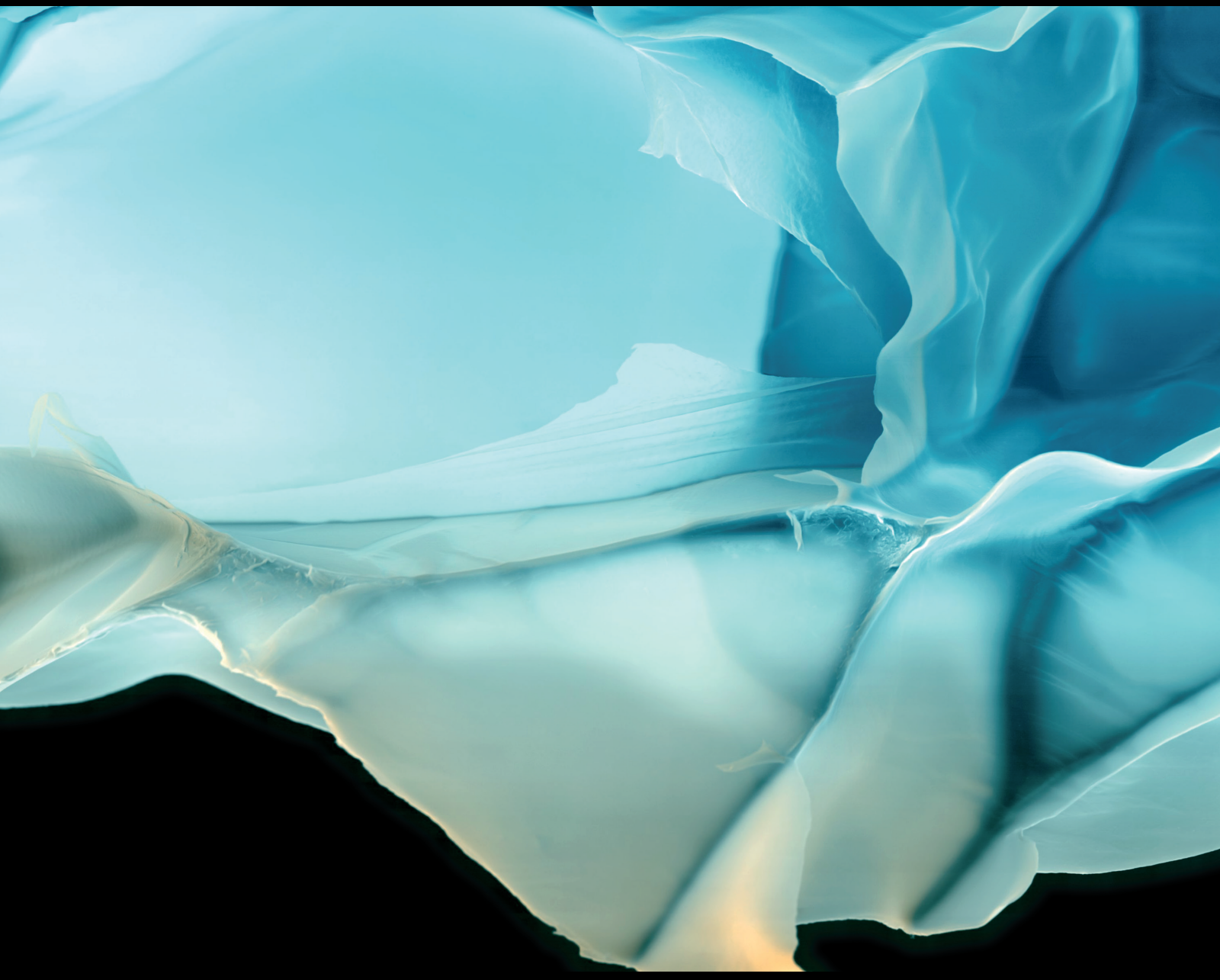

Organic-Inorganic Hybrid Polymers: Experiment, Simulation, and Application

Advances in Polymer Technology

Organic-Inorganic Hybrid Polymers: Experiment, Simulation, and Application

Lead Guest Editor: Zhiwei Qiao
Guest Editors: Hong Liang and Yongwei Chen

Contents

Hindawi
Advances in Polymer Technology
Volume 2020, Article ID 3892694, 8 pages
https://doi.org/10.1155/2020/3892694

Research Article

In Situ Synthesis and Characterization of ZnO/Chitosan Nanocomposite as an Adsorbent for Removal of Congo Red from Aqueous Solution

Nhu Thanh Nguyen,[1] Ngoc Thinh Nguyen ,[1] and Van Anh Nguyen [2]

[1]*School of Chemical Engineering, Hanoi University of Science and Technology, Hanoi 100000, Vietnam*
[2]*Faculty of Natural Sciences and Technology, Hanoi Metropolitan University, Hanoi 100000, Vietnam*

Correspondence should be addressed to Ngoc Thinh Nguyen; thinh.nguyenngoc@hust.edu.vn

Received 13 September 2019; Revised 19 November 2019; Accepted 30 November 2019; Published 17 January 2020

Guest Editor: Yongwei Chen

ZnO/chitosan nanocomposite was successfully synthesized by in-situ precipitation method. The material was characterized by XRD, FESEM, TEM, FTIR, BET, and TGA. Results show that ZnO/chitosan nanocomposite has spherical shape with the average size of 20–25 nm. BET surface area and the average pore size of ZnO/chitosan nanocomposite are 2.2436 (m^2/g) and 12.2 nm, respectively. The material was applied as an adsorbent for congo red removal from aqueous solutions. The congo red adsorption is better described by the Langmuir model ($R^2 = 0.996$) than by the Freundlich model ($R^2 = 0.962$). Therefore, it can be presumed that congo red was adsorbed in a single monolayer with the theoretical maximum adsorption capacity of 227.3 (mg/g). This is comparable to other available adsorbents. It can be suggested that ZnO/chitosan nanocomposite could serve as promising adsorbent for congo red in wastewater treatment technology.

1. Introduction

Despite of the fact that water resource is critical for the survival of living organisms, it is facing unprecedented challenges. Water pollution has become one of the most serious global issues. One of the leading sources of water pollutions is without doubt industrial activities. Every day, huge amounts of industrial wastewater are discharged into water body, and this severely affects not only the health of all living forms but also the quality of the whole ecosystem. Particularly, wastewaters from textile, pharmaceutical, food, cosmetics, plastics, photographic, paper industries, etc. are releasing large quantities of organic dyes into the environment. It was estimated that the world production of dyes in 1990s was 1,000,000 tons. For decades, it has rapidly increased with more than 100,000 types of commercial dyes. Approximately, the amount of 8–20% of the used dyes entered water environment. Numbers of them are toxic or are carcinogenic substances that are resistant to environmental degradation [1–3]. This results in the essential needs of effective and eco-friendly methods to remove these toxic chemicals from water.

Congo red dye, a benzidine-based anionic bisazo dye [1-napthalenesulfonic acid, 3,3-(4,4-biphenylene bis (azo) bis (4-amino-) disodium salt, is an interest subject to researchers due to its high toxicity to humans and its stability in the environment. In addition, after entering human bodies congo red can be metabolized into benzidine, a well-known carcinogen and mutagen in human [3, 4].

Several methods have been proposed in order to remove organic dyes from aqueous solutions such as adsorption, chemical coagulation, biodegradation, and advanced oxidation processes [5–8]. Compared to others, adsorption is considered as one the most popular methods with the advantages of being simple and cost-effective [9, 10]. Variety of materials have been investigated to be used as adsorbents for congo red, such as carbon-based materials, silica composites, cellulosic materials, and chitosan related materials [11–14]. Among them, chitosan would be a suitable candidate for producing the desirable adsorbents for congo red. Chitosan is an abundant biopolymer in nature. Its application as an adsorbent of heavy metal ions or colorants derives from its functional groups such as ($-NH_2$), ($-OH$). Nonetheless, chitosan has

several limitations such as poor adsorption capacity, low mechanical strength, low water solubility, and ease of decomposition under acidic conditions [15]. For this reason, chitosan is usually combined with other substances such as hydroxyapatite, TiO_2, ZnO, Fe_3O_4 to form composites in order to overcome these disadvantages [15, 16]. In this study, the aim was to synthesize ZnO/chitosan nanocomposite in situ from Zn^{2+} by a simple and cost-effective precipitation method that allows to prepare the material in a large-scale. The material was thoroughly characterized and applied to remove congo red in aqueous solutions.

2. Materials and Methods

2.1. Materials and Method. Chitosan flakes (molecular weight Mw = 32 kDa and degree of deacetylation DD = 85%) were prepared and characterized in our laboratory [17]. All other chemicals including $Zn(NO_3)_2.6H_2O$, CH_3COOH, and NaOH were of analytical grade and used without further purification.

Chitosan solutions were prepared by completely dissolving 0.5 g of chitosan flakes in 100 mL of CH_3COOH 1% solution. ZnO/chitosan nanocomposite was produced by in situ precipitation method. The weight ratio of $m_{chitosan}/m_{ZnO}$ reported in former publications varies in a wide range from 0.084 to 1.0 [18–20]. In this study, the weight ratio of about 0.3 was selected. The amount of 6.246 g of $Zn(NO_3)_2.6H_2O$ was added to 100 mL of chitosan solution. The mixture was stirred at 80°C for 30 min. The pH of the obtained solution was adjusted to 10 using sodium hydroxide solution 0.1 M. The mixture was additionally stirred for 2 hours at 80°C. The white precipitate was collected by centrifugation (Hettich Mikro 22R Centrifuges), washed with distilled water, and dried at 60°C overnight (8 hours). ZnO nanoparticles was synthesized by using similar procedure. However, $Zn(NO_3)_2.6H_2O$ was mixed in 100 mL of distilled water instead of chitosan solution.

2.2. Characterization Methods. The synthesized ZnO/chitosan nanocomposite was characterized by X-ray diffraction (XRD, Bruker D8 advanced X-ray diffractometer) with Cu Kα radiation (λ = 1.54 Å) and the scan rate of 0.02 s^{-1} from 20° to 70°. Morphology of ZnO/chitosan nanocomposite was analyzed by Field Emission Hitachi S-4800 Scanning Electron Microscope (FE-SEM) and a transmission electron microscope (TEM), JEOL JEM-1010. Fourier transform infrared spectra (FT-IR) were obtained on a Nicolet iS10 Thermo Scientific spectrometer (USA). The thermal properties were studied by TGA (DSC131, Labsys TG/DSC1600, TMA, and Setaram, France). The nitrogen adsorption–desorption isotherms of the adsorbents (i.e. chitosan, ZnO nanoparticles and ZnO/chitosan nanocomposite) were recorded by the TriStar II 3020 nitrogen adsorption apparatus (Micromeritics Instruments, USA) at 77 K. The pore size distribution and the BET specific surface area (S_{BET}) of the samples were determined by the Barrett–Joyner–Halenda (BJH) method.

2.3. Adsorption Experiments. Chitosan used in adsorption experiment was prepared as the following: chitosan flakes were completely dissolved in CH_3COOH 1% solution and then re-precipitated by increasing the pH of the solution using NaOH 0.1 M. The mixture was stirred for 60 min. The precipitate was collected by centrifugation, washed with distilled water, and dried at 60°C overnight (8 hours).

The stock solution of congo red was prepared by disolving 1 g congo red in 1000 mL distilled water. Desired congo red solutions were obtained by diluting the stock solution (1000 mg/L). Congo red concentrations of the solutions were confirmed by Agilent 8453 UV Vis-spectrophotometer at 497 nm before every adsorption experiment.

Batch experiments were carried out by mixing 0.02 g of the adsorbents with 40 mL of congo red solutions in 50 mL-centrifuge tubes. The mixtures were ultrasonicated at 30°C (Elmasonic S100H Ultrasonic Bath) and then centrifuged at 6000 rpm. Congo red concentrations of supernatants were measured.

In order to find the equilibrium time of the congo red adsorption by ZnO/chitosan nanocomposite, the initial congo red concentration of 100 mg/L was applied. The supernatant was sampled at definite time intervals and measured for congo red concentration until negligible change in the congo red concentration was observed, signalling the equilibrium of the adsorption process. During the experiment, samples of supernatant were returned to the centrifuge tube after every measurement [21].

A series of solutions with different congo red concentrations varying from 100 to 550 mg/L was employed to determine the maximum congo red adsorption capacity of ZnO/chitosan nanocomposite. The reaction time was the equilibrium time of the congo red adsorption by ZnO/chitosan nanocomposite found in the previous experiment.

The congo red removal efficiencies of the three adsorbents were also compared by carrying out adsorption experiments with the initial congo red concentration of 100 mg/L.

The adsorbed amount of congo red per unit of weight of adsorbent, q_t (mg/L), was calculated from the mass balance equation:

$$q_t = \frac{(C_0 - C_t)}{m}, \tag{1}$$

and percent of congo red removal:

$$R\% = \frac{(C_0 - C_e)}{C_0} \times 100, \tag{2}$$

where C_0, C_t and C_e (mg/L) are initial congo red concentration, the congo red concentration after time t, and the congo red concentration at equilibrium, respectively; V (L) is the volume of the solutions; and m (g) is the mass of the adsorbents.

3. Results and Discussion

3.1. Characterization of ZnO/Chitosan Nanocomposite. XRD patterns of ZnO/chitosan nanocomposite are shown in Figure 1. The major peaks at scattering angles (2θ) of 31.8°, 34.4°, 36.2°, 47.5°, 56.6°, 62.8°, 66.3°, 68.1°, and 69.3° correspond to the lattice planes of (100), (002), (101), (102), (110), (103), (200),

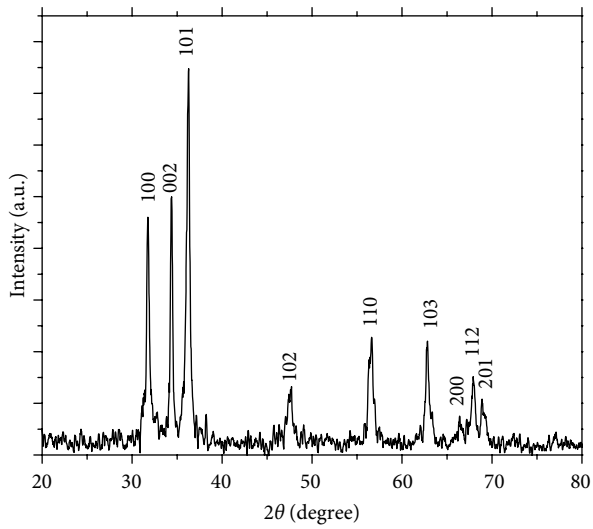

Figure 1: XRD patterns of ZnO/chitosan nanocomposite.

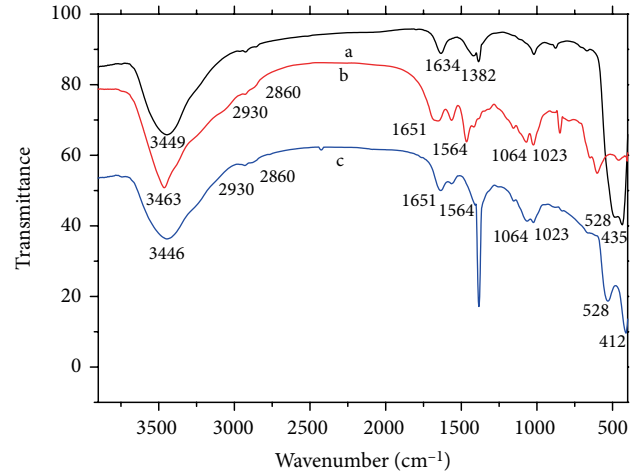

Figure 3: The FTIR spectra of ZnO nanoparticles (a), chitosan (b), and ZnO/chitosan nanocomposite (c).

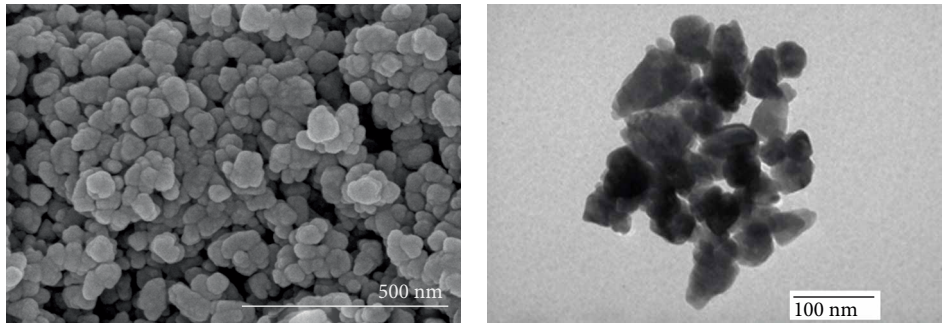

(a) (b)

Figure 2: FE-SEM image (a) and TEM image (b) of the ZnO/chitosan nanocomposite.

(112), and (201), respectively. These represent the wurtzite hexagonal phase of ZnO, confirming the formation of ZnO particles. The observed diffraction reflections are well-matched with the reported literature as well as standard JCPDS data card No. 36–1451 [18, 19, 22, 23]. Other diffraction peaks referring to any impurities were not detected, suggesting that precipitated $Zn(OH)_2$ was completely decomposed to ZnO.

The crystal size of ZnO/chitosan nanocomposite was calculated from the broadening of diffraction peaks using Debye–Scherer formula [5]:

$$D = \frac{k\lambda}{\beta\cos\theta}, \quad (3)$$

where D is crystal size, k is constant (0.94), $\lambda = 0.154$ nm represents the wavelength of X-ray radiation, β is the full width at half maximum of diffraction peaks (FWHM) in radian, and θ is the Bragg's angle. The crystal size of the ZnO/chitosan nanocomposite was evaluated by measuring the FWHM of the most intense peak (101) because it has a relatively strong intensity and does not overlap with other diffraction peaks. Approximately, the average crystal size of ZnO/chitosan nanocomposite is of 22 nm.

Figure 2 shows the FE-SEM (a) and TEM (b) images of the ZnO/chitosan nanocomposite. As can be seen, the spherical particles appear to be quite distinct and uniform, and the size of the particles ranges from 20 to 25 nm.

Figure 3 shows the FTIR spectra of ZnO nanoparticles, chitosan, and ZnO/chitosan nanocomposite. In the FTIR spectrum of ZnO nanoparticles (Figure 3(a)), the peak at 3449 cm^{-1} corresponds to the O–H stretching vibration of H_2O in ZnO; the peak at 1634 cm^{-1} may be due to the O–H bending vibration; the H–O–H bending vibration or the absorbed CO_2 bands may be responsible for the peak at 1382 cm^{-1}; and the band in the range of 528–435 cm^{-1} refers to the stretching mode of Zn–O [24–26]. In the spectrum of chitosan (Figure 3(b)), the broad peak at 3463 cm^{-1} is due to the –OH/–NH_2 stretching vibration; the peaks at 2930 and 2860 cm^{-1} are attributed to the C–H stretching vibration; the peak at 1651 cm^{-1} corresponds to the amino group bending vibrations; the peak at 1564 cm^{-1} may be due to the deformation of amide II; and the peaks at 1064 and 1023 cm^{-1} may refer to the C–O stretching vibration [27–31]. Compared to the spectrum of chitosan, a new band from 528 to 412 cm^{-1} referring to the Zn–O stretching appears in the spectrum of ZnO/chitosan

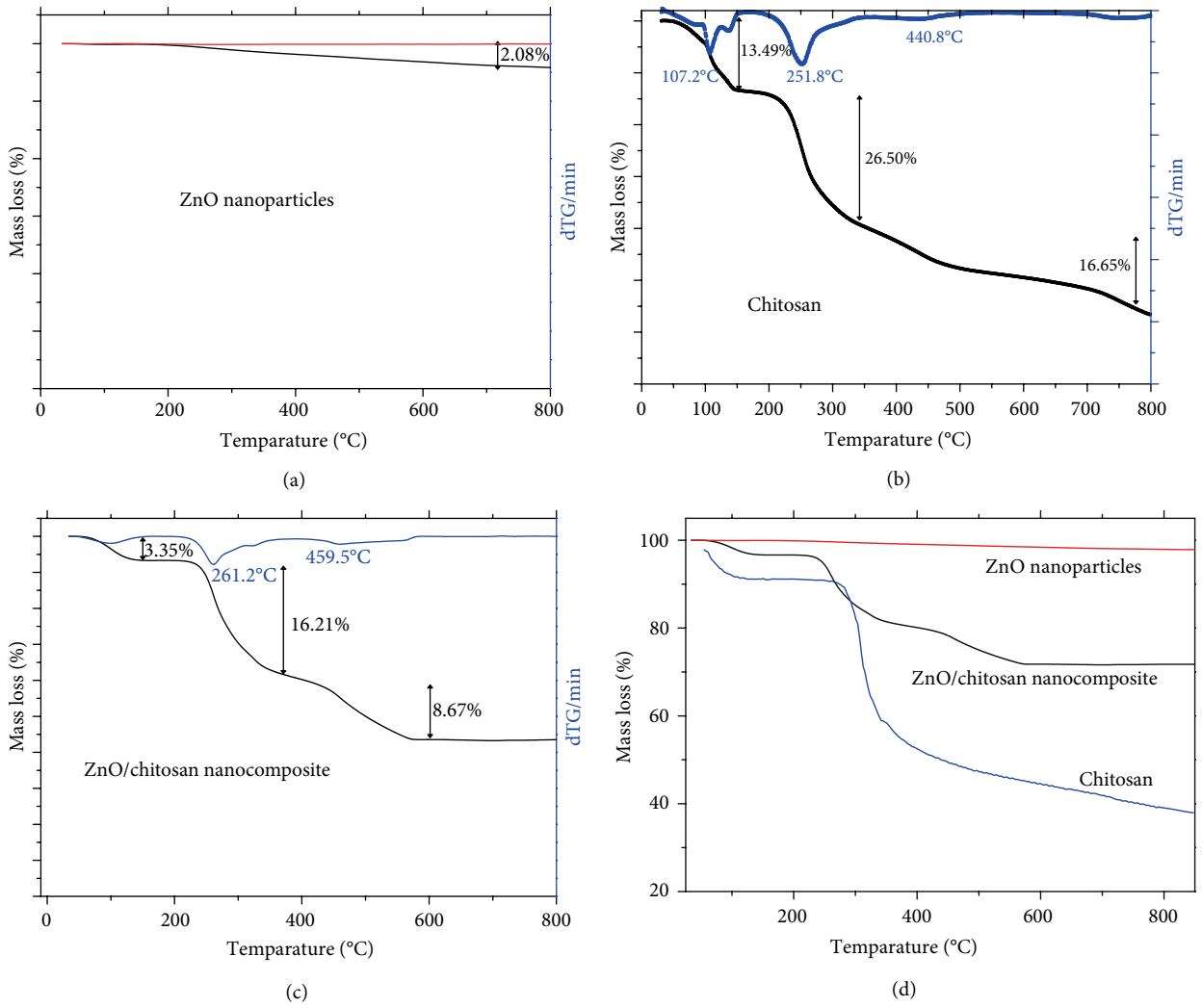

Figure 4: Thermo-gravimetric curves of ZnO nanoparticles (a), chitosan (b), and ZnO/chitosan nanocomposite (c).

Table 1: BET surface areas, pore volume, and pore size in the ZnO nanoparticles, chitosan and ZnO/chitosan nanocomposite.

Sample	S_{BET} (m^2/g)[a]	Pore volume (cm^3/g)[b]	Average pore size (nm)[c]
ZnO nanoparticles	9.7852	0.031169	11.3386
Chitosan	1.7461	0.010181	21.6846
ZnO/chitosan nanocomposite	2.2436	0.007779	12.2102

[a]BET surface area calculated from the linear part of the BET plot. [b]BJH adsorption cumulative volume of pores between 17.0 Å and 3000.0 Å diameter. [c]Adsorption average pore diameter (4 V/A by BET).

Table 2: Parameters of the Langmuir and Freundlich adsorption isotherms.

Temperature (K)	Langmuir adsorption isotherm			Freundlich adsorption isotherm		
	q_m (mg/g)	K_L (L/mg)	R^2	K_F (mg/g).$(L/mg)^{1/n}$	n	R^2
303	227.3	0.048	0.996	101.3	7.91	0.962

nanocomposite (Figure 3(c)). This indicates the existence of ZnO in the structure of the nanocomposite. In addition, the peak relating to the –OH/–NH_2 stretching vibration in chitosan (at 3463 cm^{-1}) is broader and shifted to the lower wavenumber (3446 cm^{-1}) in the nanocomposite, suggesting the strong intermolecular hydrogen bonding interaction between chitosan and ZnO [32].

The thermogravimetric (TG) curves of chitosan, ZnO nanoparticles and ZnO/chitosan nanocomposite were recorded (Figure 4). The TG curve of ZnO nanoparticles slightly went down as the temperature was increased from 25 to 800°C. The mass loss of 2.08% corresponds to the loss of absorbed water (Figure 4(a)). In the TG curve of chitosan,

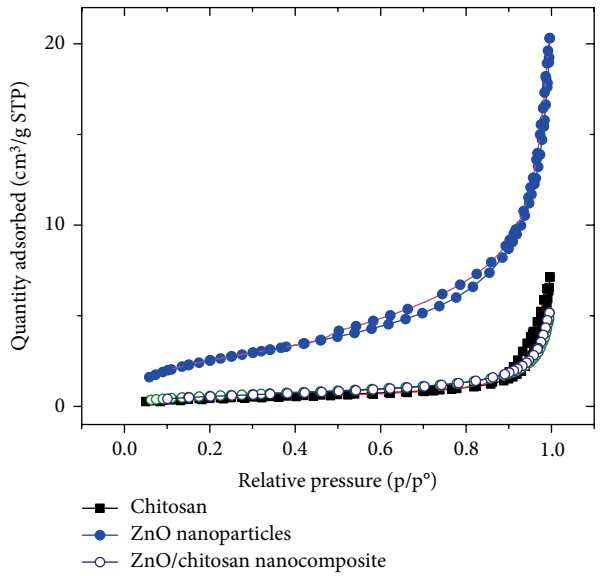

Figure 5: Nitrogen adsorption–desorption isotherms of ZnO nanoparticles, chitosan, and ZnO/chitosan nanocomposite.

Table 3: Maximum congo red adsorption capacity of several adsorbents.

Adsorbents	q_m (mg/g)	References
Fe_3O_4/Bi_2S_3 microspheres	92.24	[39]
MWCNTs/calcined eggshell	136.99	[40]
Magnetic CS/carrageenan ampholytic microspheres	212.7	[41]
Chitosan coated magnetic Fe_3O_4 particle	42.62–56.66	[42]
Zinc peroxide nanomaterial	208	[43]
ZnO microspheres	304	[44]
Mg-doped ZnO NPs	125	[45]
Hierarchical porous ZnO	334	[46]
ZnO/chitosan nanocomposite	227.3	This study

there are three stages of mass loss (Figure 4(b)). The first stage occurs from 50 to 120°C and reaches to the maximum degradation rate at 107.2°C with 13.49% mass loss, referring to the dehydration process. The second stage (from 220 to 350°C) with 26.50% mass loss may be due to the degradation and decomposition of the backbone chain of volatile fraction. The last stage (from 350 to 800°C) with 16.65% mass loss may relate to the decomposition of the backbone chain of residual chitosan [33]. A noticeable three-stage mass loss was also observed in the TG curve of ZnO/chitosan nanocomposite (Figure 4(c)). The first stage at the temperature from 50°C to 150°C is accounted for the thermal dehydration. The last two stages with the approximate total mass loss of 16.21% (from 220 to 350°C) and 8.67% (from 350 to 600°C) are presumed to be the thermal decomposition of volatile and residual chitosan in the nanocomposite, respectively. The maximum degradation rate of volatile chitosan is shifted from 251.8°C in chitosan to 261.2°C in the nanocomposite, while that of residual chitosan is shifted from 440.8°C in chitosan to 459.5°C in

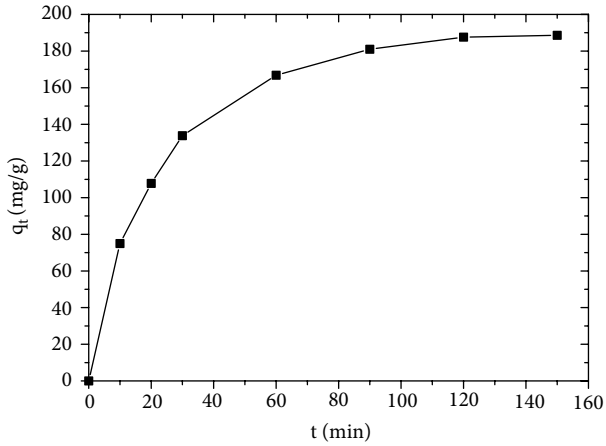

Figure 6: The relationship between adsorption capacity of ZnO/chitosan nanocomposite and adsorption time (volume: 40 mL; adsorbent dose: 0.02 g; initial congo red concentration: 100 mg/L).

the nanocomposite. The formation of hydrogen bonding between chitosan and zinc oxide in the composite may be responsible to this phenomenon [21].

Nitrogen adsorption–desorption isotherms of ZnO nanoparticles, chitosan, and ZnO/chitosan nanocomposite are displayed in Figure 5. The three materials have type IV isotherm (IUPAC classification) [34]. Moreover, the very narrow hysteresis loops at high (chitosan and nanocomposite) and moderate relative pressure (ZnO nanoparticles) indicate the presence of mesopores in their structure [34–36]. The similarity between the isotherms of chitosan, and ZnO/chitosan nanocomposite shows the similar porous structures of the two materials. BET surface areas of ZnO nanoparticles, chitosan, and ZnO/chitosan nanocomposite are 9.7852, 1.7461, and 2.2436 (m^2/g), respectively (Table 1). The average pore size of the nanocomposite is 12.2 nm.

3.2. Congo Red Adsorption by ZnO/Chitosan Nanocomposite. The relationship between adsorption capacity of ZnO/chitosan nanocomposite and adsorption time is illustrated in Figure 6. The adsorption capacity sharply rises within the first 30 minutes and negligibly changes after 120 minutes. Therefore, the reaction time in other adsorption experiments is selected to be 120 minutes.

The two most common adsorption isotherms including the Langmuir and Freundlich adsorption isotherms were applied to characterize the adsorption of congo red by ZnO/chitosan nanocomposite. The Langmuir model assumes monolayer adsorption of the adsorbate with no interaction among adsorbate molecules, whereas the Freundlich model assumes multilayer adsorption of the adsorbate.

Corresponding mathematical expressions of the Langmuir and Freundlich adsorption isotherms are written as [37, 38]:

$$\frac{C_e}{q_e} = \frac{C_e}{q_m} + \frac{1}{q_m.K_L}, \tag{4}$$

$$\log q_e = \log K_F + \frac{1}{n}\log C_e, \tag{5}$$

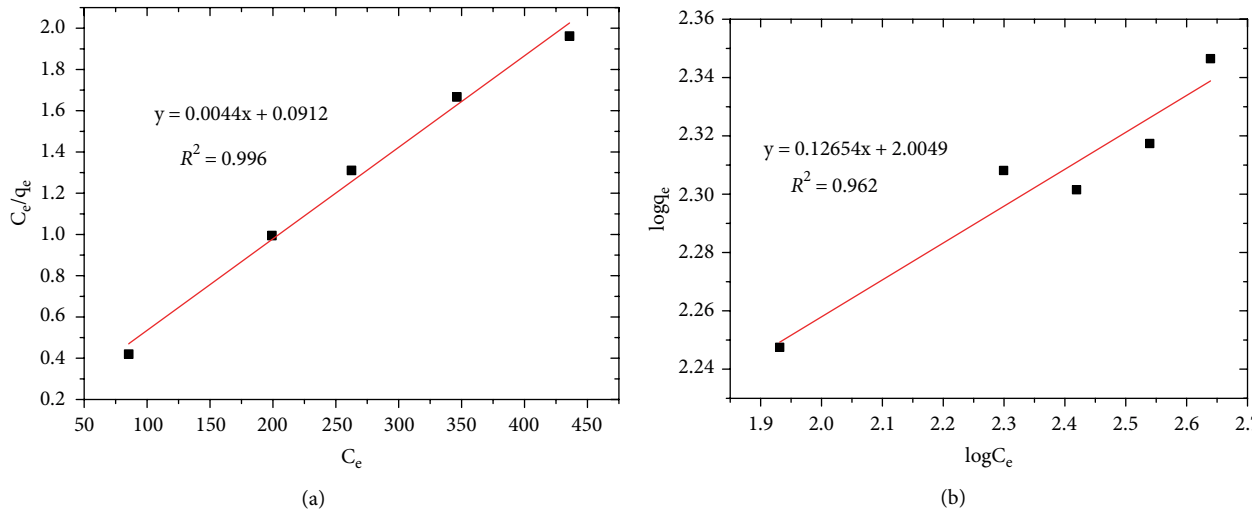

Figure 7: Adsorption isotherm for congo red adsorption by ZnO/chitosan nanocomposite: (a) Langmuir and (b) Freundlich.

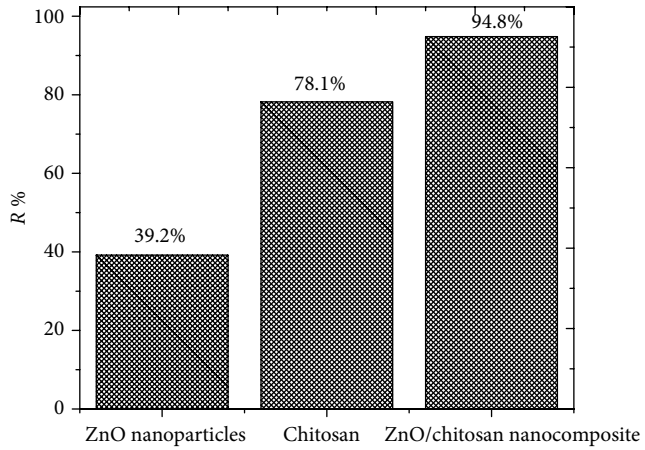

Figure 8: Congo red removal efficiencies of ZnO nanoparticles, chitosan and ZnO/chitosan nanocomposite (volume: 40 mL; adsorbent dose: 0.02 g; initial concentrations: 100 mg·$L^{-1;}$ pH values at equilibrium: about 6.5).

where: q_e (mg/g) is the amount of congo red adsorbed at equilibrium, q_m (mg/g) is the theoretical maximum amount of congo red adsorption, C_e (mg/L) is congo red concentration at equilibrium, and K_L (L/mg), K_F ((mg/g).(L/mg)$^{1/n}$) are the Langmuir and Freundlich constants, respectively.

The linear plots of the Langmuir and Freundlich models for congo red adsorption by ZnO/chitosan nanocomposite are presented in Figure 7. Table 2 summarizes calculated values of Langmuir and Freundlich model's parameters. Obtained results suggest that the congo red adsorption is better described by the Langmuir model with the significant coefficient correlation R^2 of 0.996 than by the Freundlich model (R^2 = 0.962). Therefore, it can be presumed that congo red was adsorbed in a single monolayer with the theoretical maximum adsorption capacity of 227.3 (mg/g). The maximum adsorption capacity of the synthesized ZnO/chitosan nanocomposite is comparable with other adsorbents in former studies (Table 3). It can be concluded that the obtained nanocomposite has high potential to be applied for congo red removal.

Comparison among congo red removal efficiencies of ZnO/chitosan nanocomposite, ZnO nanoparticles, and chitosan are quite interesting (Figure 8). It is well known that the adsorption capacity strongly depends on the total surface area and the number of binding sites of adsorbents. Despite the fact that the total surface area of ZnO nanoparticles is approximately 5 times higher than that of chitosan and ZnO/chitosan nanocomposite, ZnO nanoparticles have the lowest congo red removal efficiency. More than 90% of congo red was removed by ZnO/chitosan nanocomposite after 2 hours and 78.1% of congo red was eliminated by chitosan, while only 39.2% of the dye was removed by ZnO nanoparticles. This suggests that the presence of chitosan in the nanocomposite is mainly responsible for the congo red adsorption capability of the material. In ZnO/chitosan nanocomposite, the ZnO may play a role as a rigid support for the thin film of chitosan, which contains –OH/–NH_2 groups. These functional groups probably play a role as binding sites to congo red molecules as proposed in numbers of publications [21, 47]. Further study, however, should be carried out in order to address the exact mechanism of the adsorption process.

4. Conclusions

In the present work, the ZnO/chitosan nanocomposite was successfully generated by direct simple, fast, and eco-friendly in situ precipitation method. XRD results reveal that the nanocomposite has wurtzite structure. The size of the nanocomposite is approximately 20–25 nm. The FESEM and TEM images show the spherical morphology of the material. The similarity in porous structures of chitosan and ZnO/chitosan nanocomposite was observed. BET surface area of ZnO/chitosan nanocomposite is 2.2436 (m^2/g) and the average pore size of the nanocomposite is 12.2 nm. The material was applied as an adsorbent in order to remove congo red from aqueous solutions. According to the Langmuir isotherm model, the

theoretical maximum adsorption capacity of ZnO/chitosan nanocomposite is 227.3 (mg/g). From this result, it can be suggested that ZnO/chitosan nanocomposite could serve as a promising adsorbent for congo red in wastewater treatment technology.

Data Availability

The data used to support the findings of this study are available from the corresponding author upon request.

Conflicts of Interest

The authors declare that they have no conflicts of interest.

Acknowledgments

This study was supported by the Ministry of Science and Technology in South Korea through the International Environmental Research Institute (IERI) of Gwangju Institute of Science and Technology (GIST) in 2019.

References

[1] K. Hunger, *Industrial Dyes: Chemistry, Properties, Applications*, Wiley-VCH, Weinheim, 2003.

[2] S. K. Sharma, *Green Chemistry for Dyes Removal from Wastewater: Research Trends and Applications*, Scrivener Publishing, John Wiley & Sons, USA, 2015.

[3] R. M. Christie, *Environmental Aspects of Textile Dyeing*, Woodhead Publishing Limited, UK, 2007.

[4] E. Alver, M. Bulut, A. Ü. Metin, and H. Çiftçi, "One step effective removal of Congo Red in chitosan nanoparticles by encapsulation," *Spectrochimica Acta Part A: Molecular and Biomolecular Spectroscopy*, vol. 171, pp. 132–138, 2017.

[5] X. Liu, J. Tian, Y. Li et al., "Enhanced dyes adsorption from wastewater via Fe_3O_4 nanoparticles functionalized activated carbon," *Journal of Hazardous Materials*, vol. 373, pp. 397–407, 2019.

[6] T.-H. Kim, C. Park, J. Yang, and S. Kim, "Comparison of disperse and reactive dye removals by chemical coagulation and Fenton oxidation," *Journal of Hazardous Materials*, vol. 112, no. 1-2, pp. 95–103, 2014.

[7] Z. Aslam, M. Qaiser, R. Ali, A. Abbas, Ihsanullah, and S. Zarin, "Al_2O_3/MnO_2/CNTs nanocomposite: synthesis, characterization and phenol adsorption," *Fullerenes, Nanotubes and Carbon Nanostructures*, vol. 27, no. 7, pp. 591–600, 2019.

[8] A.-N. M. Salem, M. Ahmed, and M. El-Shahat, "Selective adsorption of amaranth dye on Fe_3O_4/MgO nanoparticles," *Journal of Molecular Liquids*, vol. 219, pp. 780–788, 2016.

[9] Y. Zhou, L. Jian, Y. Zhou, and Y. Liu, "Recent advances for dyes removal using novel adsorbents: a review," *Environmental Pollution*, vol. 252, pp. 352–365, 2019.

[10] Q. Lu, J. Zheng, J. Yu et al., "Synthesis and adsorption properties for cationic dyes of acrylic acid/vermiculite hydrogel initiated by glow-discharge-electrolysis plasma," *Advances in Polymer Technology*, vol. 37, no. 4, 2018.

[11] S. Ghorai, A. K. Sarkar, A. B. Panda, and S. Pal, "Effective removal of Congo red dye from aqueous solution using modified xanthan gum/silica hybrid nanocomposite as adsorbent," *Bioresource Technology*, vol. 144, pp. 485–491, 2013.

[12] L. Bulgariu, L. B. Escudero, O. S. Bello et al., "The utilization of leaf-based adsorbents for dyes removal: a review," *Journal of Molecular Liquids*, vol. 276, pp. 728–747, 2019.

[13] A. Zahir, Z. Aslam, M. S. Kamal, W. Ahmad, A. Abbas, and R. A. Shawabkeh, "Development of novel cross-linked chitosan for the removal of anionic Congo red dye," *Journal of Molecular Liquids*, vol. 244, pp. 211–218, 2017.

[14] I. Tahira, Z. Aslama, A. Abbas, M. Monim-ul-Mehboob, S. Ali, and A. Asghar, "Adsorptive removal of acidic dye onto grafted chitosan: a plausible grafting and adsorption mechanism," *International Journal of Biological Macromolecules*, vol. 136, pp. 1209–1218, 2019.

[15] M. Vakili, M. Rafatullah, B. Salamatinia et al., "Application of chitosan and its derivatives as adsorbents for dye removal from water and wastewater: a review," *Carbohydrate Polymers*, vol. 113, pp. 115–130, 2014.

[16] J. M. N. dos Santos, C. R. Pereira, L. A. A. Pinto et al., "Synthesis of a novel $CoFe_2O_4$/chitosan magnetic composite for fast adsorption of indigotine blue dye," *Carbohydrate Polymers*, vol. 217, pp. 6–14, 2019.

[17] H. V. Tran, L. T. Bui, T. T. Dinh, D. H. Le, C. D. Huynh, and A. X. Trinh, "Graphene oxide/Fe_3O_4/chitosan nanocomposite: a recoverable and recyclable adsorbent for organic dyes removal. Application to methylene blue," *Materials Research Express*, vol. 4, no. 3, p. 035701, 2017.

[18] H. A. Abdel, A. M. Saad, S. T. Azzam, B. B. El-Wakeel, and M. B. Mostafa, "Removal of toxic metal ions from wastewater using ZnO@Chitosan coreshell nanocomposite," *Environmental Nanotechnology, Monitoring & Management*, vol. 9, pp. 67–75, 2018.

[19] P. Bhadra, M. K. Mitra, G. C. Das, R. Dey, and S. Mukherjee, "Interaction of chitosan capped ZnO nanorods with *Escherichia coli*," *Materials Science and Engineering C*, vol. 31, no. 5, pp. 929–937, 2011.

[20] S. Çınar, Ü. H. Kaynar, T. Aydemir, S. Çam Kaynar, and M. Ayvacıklı, "An efficient removal of RB5 from aqueous solution by adsorption onto nano-ZnO/Chitosan composite beads," *International Journal of Biological Macromolecules*, vol. 96, pp. 459–465, 2017.

[21] M. Blachnio, T. M. Budnyak, A. Derylo-Marczewska, A. W. Marczewski, and V. A. Tertykh, "Chitosan–silica hybrid composites for removal of sulfonated azo dyes from aqueous solutions," *Langmuir*, vol. 34, no. 6, pp. 2258–2273, 2018.

[22] Joint Committee for Powder Diffraction Society (JCPDS), "Powder diffraction database, pattern," pp. 1436–1451, 1972.

[23] L.-H. Li, J.-C. Deng, H.-R. Deng, Z.-L. Liu, and L. Xin, "Synthesis and characterization of chitosan/ZnO nanoparticle composite membranes," *Carbohydrate Research*, vol. 345, no. 8, pp. 994–998, 2010.

[24] K. Raja, P. S. Ramesh, and D. Geetha, "Structural, FTIR and photoluminescence studies of Fe doped ZnO nanopowder by co-precipitation method," *Spectrochimica Acta Part A: Molecular and Biomolecular Spectroscopy*, vol. 131, pp. 183–188, 2014.

[25] E. Selvarajan and V. Mohanasrinivasan, "Biosynthesis andcharacterization of ZnO nanoparticles using Lactobacillus plantarum VITES07," *Materials Letters*, vol. 112, pp. 180–182, 2013.

[26] D. Wu, W. Wang, F. Tan, F. Sun, H. Luand, and X. Qiao, "Fabrication of pit-structured ZnO nanorods and their enhanced photocatalytic performance," *RSC Advances*, vol. 3, no. 43, pp. 20054–20059, 2013.

[27] H. Wang, X. Gong, Y. Miao et al., "Preparation and characterization of multilayer films composed of chitosan, sodium alginate and carboxymethyl chitosan-ZnO nanoparticles," *Food Chemistry*, vol. 283, pp. 397–403, 2019.

[28] Lijun You, Ci Huang, Lu Feifei, Ao Wang, Xiaocui Liu, and Q. Zhang, "Facile synthesis of high performance porous magnetic chitosan—polyethylenimine polymer composite for Congo red removal," *International Journal of Biological Macromolecules*, vol. 107, pp. 1620–1628, 2018.

[29] M. Hasmath Farzana and S. Meenakshi, "Visible light-driven photoactivity of zinc oxide impregnated chitosanbeads for the detoxification of textile dyes," *Applied Catalysis A: General*, vol. 503, pp. 124–134, 2015.

[30] Z. Huang, Z. Li, L. Zheng et al., " Interaction mechanism of uranium (VI) with three-dimensional graphene oxide-chitosan composite: Insights from batch experiments, IR, XPS, and EXAFS spectroscopy," *Chemical Engineering Journal*, vol. 328, pp. 1066–1074, 2017.

[31] E. Zabihi, A. Babaei, D. Shahrampour, Z. Arab-Bafrani, K. S. Mirshahidi, and H. J. Majidi, "Facile and rapid in-situ synthesis of chitosan-ZnO nano-hybrids applicable in medical purposes; a novel combination of biomineralization, ultrasound, and bio-safe morphology-conducting agent," *International Journal of Biological Macromolecules*, vol. 131, pp. 107–116, 2019.

[32] B. Qiu, X.-F. Xu, R.-H. Deng, G.-Q. Xia, X.-F. Shang, and P.-H. Zhou, "Construction of chitosan/ZnO nanocomposite film by in situ precipitation," *International Journal of Biological Macromolecules*, vol. 122, pp. 82–87, 2019.

[33] F. A. López, A. L. R. Mercê, F. J. Alguacil, and A. López-Delgado, "A kinetic study on the thermal behaviour of chitosan," *Journal of Thermal Analysis and Calorimetry*, vol. 91, no. 2, pp. 633–639, 2008.

[34] K. S. W. Sing, "Reporting physisorption data for gas/solid systems with special reference to the determination of surface area and porosity," *Pure and Applied Chemistry*, vol. 54, no. 11, pp. 2201–2218, 1982.

[35] N. Farhadian, R. Akbarzadeh, M. Pirsaheb, T.-C. Jen, Y. Fakhri, and A. Asadi, "Chitosan modified N, S-doped TiO_2 and N, S-doped ZnO for visible light photocatalytic degradation of tetracycline," *International Journal of Biological Macromolecules*, vol. 132, pp. 360–373, 2019.

[36] Y. Zheng, B. Cheng, W. You, J. Yua, and W. Ho, "3D hierarchical graphene oxide-NiFe LDH composite with enhanced adsorption affinity to Congo red, methyl orange and Cr(VI) ions," *Journal of Hazardous Materials*, vol. 369, pp. 214–225, 2019.

[37] H. Haojun, J. Liu, X. Zhihua, L. Zhang, B. Cheng, and W. Ho, "Hierarchical porous Ni/Co-LDH hollow dodecahedron with excellent adsorption property for Congo red and Cr(VI) ions," *Applied Surface Science*, vol. 478, pp. 981–990, 2019.

[38] Y. Zheng, J. Liu, B. Cheng, W. You, W. Hoc, and H. Tang, "Hierarchical porous Al_2O_3@ZnO core-shell microfibres with excellent adsorption affinity for Congo red molecule," *Applied Surface Science*, vol. 473, pp. 251–260, 2019.

[39] R. Huayue Zhu, J. L. Jiang, F. Yongqian, S. Jiang, and J. Yao, "Magnetically recyclable Fe_3O_4/Bi_2S_3 microspheres for effective removal of Congo red dye by simultaneous adsorption and photocatalyticregeneration," *Separation and Purification Technology*, vol. 179, pp. 184–193, 2017.

[40] E. N. Seyahmazegi, R. Mohammad-Rezaei, and H. Razmi, "Multiwall carbon nanotubes decorated on calcined eggshell waste as a novel nano-sorbent: application for anionic dye Congo red removal," *Chemical Engineering Research and Design*, vol. 109, pp. 824–834, 2016.

[41] X. Liang, J. Duan, Q. Xua, X. Wei, A. Lu, and L. Zhang, "Ampholytic microspheres constructed from chitosan and carrageenan in alkali/urea aqueous solution for purification of various wastewater," *Chemical Engineering Journal*, vol. 317, pp. 766–776, 2017.

[42] H. Zhu, M. Zhang, Y. Liu, L. Zhang, and R. Han, "Study of Congo red adsorption onto chitosan coated magnetic iron oxide in batch mode," *Desalination and Water Treatment*, vol. 37, pp. 46–54, 2012.

[43] S. Chawla, H. Uppal, M. Yadav, N. Bahadur, and N. Singh, "Zinc peroxide nanomaterial as an adsorbent for removal of Congo red dye from wastewater," *Ecotoxicology and Environmental Safety*, vol. 135, pp. 68–74, 2017.

[44] C. Lei, M. Pi, B. Chenga, C. Jiang, and J. Qin, "Fabrication of hierarchical porous ZnO/NiO hollow microspheres for adsorptive removal of Congo red," *Applied Surface Science*, vol. 435, pp. 1002–1010, 2018.

[45] P. P. Ratha, S. S. Beheraa, B. Priyadarshini et al., "Influence of Mg doping on ZnO NPs for enhanced adsorption activity of Congo Red dye," *Applied Surface Science*, vol. 491, pp. 256–266, 2019.

[46] C. Lei, M. Pi, C. Jiang, B. Cheng, and J. Yu, "Synthesis of hierarchical porous zinc oxide (ZnO) microspheres with highly efficient adsorption of Congo red," *Journal of Colloid and Interface Science*, vol. 490, pp. 242–251, 2017.

[47] A. Mokhtar, S. Abdelkrim, A. Djelad et al., "Adsorption behavior of cationic and anionic dyes on magadiite-chitosan composite beads," *Carbohydrate Polymers*, vol. 229, p. 115399, 2020.

Hindawi
Advances in Polymer Technology
Volume 2019, Article ID 8132308, 11 pages
https://doi.org/10.1155/2019/8132308

Research Article

Numerical Simulation of Mixing Characteristics in the Eccentric Rotor Extruder with Different Process Conditions and Structural Parameters

De-jun Fan,[1,2,3] **Ming-kai Yang**,[1,2,3] **Zhi-gao Huang**,[4] **and Jin-song Wen**[1,2,3]

[1]*The National Engineering Research Center of Novel Equipment for Polymer Processing, South China University of Technology, Guangzhou, China*
[2]*The Key Laboratory of Polymer Processing Engineering of Ministry of Education, South China University of Technology, Guangzhou, China*
[3]*The Guangdong Provincial Key Laboratory of Technique and Equipment for Macromolecular Advanced Manufacturing, South China University of Technology, Guangzhou, China*
[4]*The State Key Laboratory of Materials Processing and Die & Mould Technology, Huazhong University of Science and Technology, Wuhan, China*

Correspondence should be addressed to Jin-song Wen; jswen@scut.edu.cn

Received 16 May 2019; Revised 24 July 2019; Accepted 29 August 2019; Published 4 December 2019

Guest Editor: Hong Liang

Numerical simulation was performed with the computational fluid dynamics analysis software POLYFLOW to investigate the influence of different process conditions and structural parameters on mixing characteristics of the eccentric rotor extruder. The intensity of shear and elongational flow strengthened when the rotational speed increased, but the time for material to stay in the extruder will be reduced. At the same time, the increase of radius and eccentricity could effectively promote the mixing performance. On the contrary, the mixing capacity reduced with the increase of the pitch. The results can be useful to optimize the structure design and guide production.

1. Introduction

During extrusion processing, the mixing characteristics of the extruder are directly related to the quality of the products. In order to improve the mixing effect of polymer materials and the product performance, the eccentric rotor extruder (ERE) was invented by Qu et al. [1]. Its plasticating and conveying theory are based on elongational rheology which are totally different from the traditional screw extruder [2]. As shown in Figure 1, the ERE consists of a stator and an eccentric rotor disposed in the inner cavity of the stator. The eccentric rotor comprises multiple alternatingly disposed spiral segments and straight segments, and the stator cavity comprises multiple alternatingly disposed spiral segments and straight segments corresponding with that of the rotor. During the polymer processing, the eccentric rotor will be forced to rotate around its own axis and revolves in the long round cavity of the stator at the same speed but in the opposite direction due to the structural limitations of the inner cavity of the stator. The materials between the stator and rotor receive the pulsed volume deformation when periodically compressed and released, thus completing the plasticating and conveying process dominated by the continuous elongation flow.

The present experimental research about the ERE proved that this innovative equipment has the advantages of low energy consumption, positive displacement transportation, strong dispersing mixing ability and wide adaptability. Wu et al. [3, 4] used the ERE to fabricate the poly(L-lactide) (PLLA)/organo-modified montmorillonite (OMMT) nanocomposites in different OMMT concentrations. The results showed that the OMMT nanoparticles were uniformly dispersed in the PLLA matrix and mainly existed in intercalation mode. The intercalation and exfoliation process of OMMT in the ERE may be a double-side exfoliation, which is more effective than the layer-by-layer peeling mechanism based on the shear flow. The OMMT nanoparticles had good dispersion and intercalation effect under the action of tensile deformation, which provided a good processing method to improve

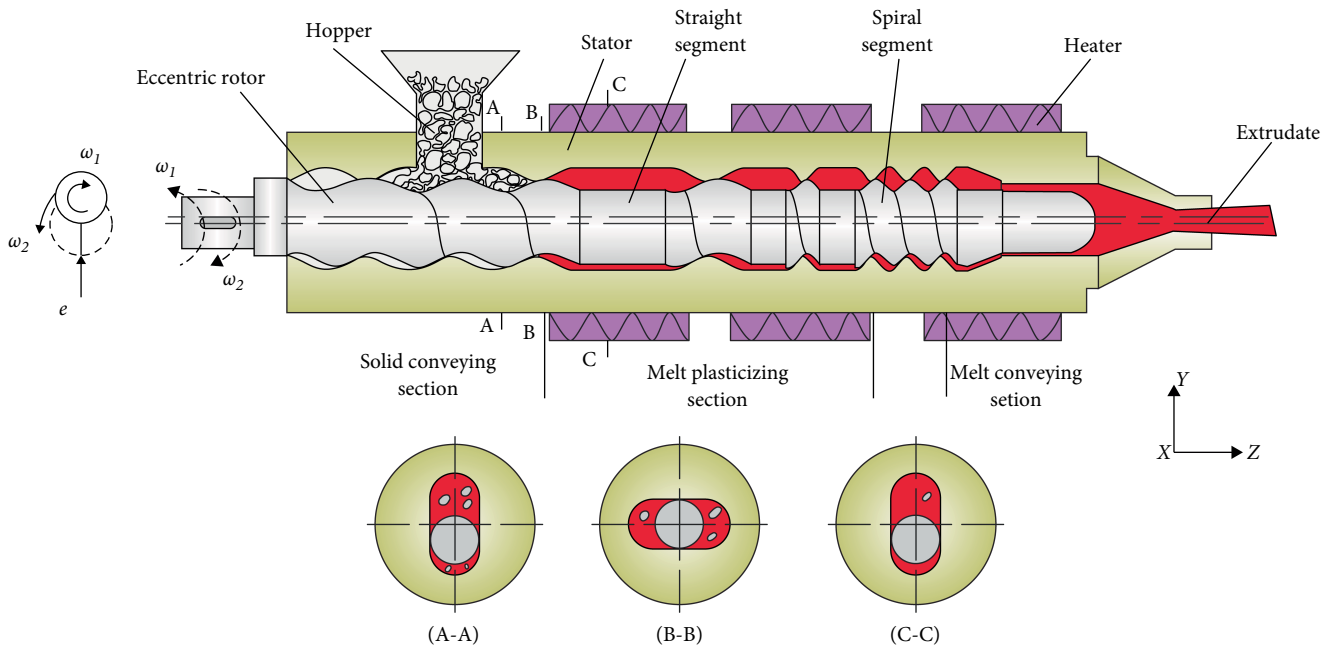

Figure 1: The schematic diagram of the ERE.

the properties of PLLA and expand its application. Cao et al. [5] processed ultrahigh molecular weight polyethylene (UHMWPE) by the ERE without any processing aids and then compared with a conventional rotational batch mixer based on a shear flow. The morphological and rheological characterization verify that the technique based on the elongational flow could effectively reduce melting defects and yield more homogeneous morphology within the extruding samples relative to the conventional bath mixing. The crystallinity for the sample prepared under an elongational flow is lower than that processed under a shear flow. Lin [6] firstly introduced the ERE to prepare PP/POE blends and studied the effect of POE proportions, rotational speed and DCP contents on the structure and properties of PP/POE blends. The results showed that volume fluctuation elongational flow generated by ERE had strong dispersive mixing ability, made that POE could be dispersed evenly in PP matrix. The mechanical tests revealed that PP/POE blends had optimal values of general mechanical properties when POE content was 30% and the rotational speed was 45 r/min. The addition of DCP can both bring POE cross-linking and PP degradation. With the increase of DCP contents, the crystal size of PP increased gradually and crystallization was more and more complete. The numerical simulation method is an important method for studying extrusion processing. Chen et al. [7] used POLYFLOW to analyze the velocity profile and the flow stretching in three rotor cross sections with different geometries to reveal the relationship between the geometry and mixing ability of rotor cross section. The rotor geometry was quantified with pressurization coefficient S and the distribution was evaluated numerically with the particle tracking technology. The results showed that the rotor cross-section with larger S would have stronger mixing ability. Decreasing wedge angle a or width of wing tip e, as well as increasing maximum clearance H0, would induce the increase of S, and further resulting in the improvement of the mixing ability. Rotor geometry quantification with S would intuitionally reveal the relationship between rotor geometry and the mixing ability. Xu [8] proposed a new mapping method for the numerical simulation of melt flow in the complicated forward conveying element of a corotating twin screw extruder. After inputting the exported data of the flow field from POLYFLOW, used the self-developed code to characterize the mixing behavior under different rotation speeds of the screw elements. Advection evolution of passive particle groups was simulated by a fourth-order Runge–Kutta tracking method and examined the effect of screw rotation speed on distributive mixing. The results showed that the mixing was highly dependent on the initial position whether the particle groups were first placed close to or far away from the intermeshing zone. Cheng et al. [9] carried out particle tracking technique to simulate mixing process of a highly viscous Newtonian fluid in a horizontal self-cleaning twin-shaft kneader. The result of finite element method proved that the horizontal twin-shaft kneader is efficient for mixing highly viscous fluids due to the intermeshing of kneading bars. There exists a strong intermeshing interaction between the kneading bars mounted on the rotating shafts in the overlapping zone, which can disrupt the cluster and promote the material exchange in the angular position.

Prior research on the ERE has mainly focused on the theoretical description of processing, preparation and researching the composite materials formed by the ERE. However, we knew of no research on the mixing numerical simulation for the ERE and visualization of mixing process have been performed. It is desirable to use numerical simulation to study the relationship between unique structure and mixing performance. In this study, the finite element Computational Fluid Dynamics (CFD) analysis software POLYFLOW (ANSYS, Inc.,

USA) was used to perform the numerical simulation of polymeric melts flow characteristics for melt conveying section in the ERE. The numerical simulation of mixing characteristics for the ERE was performed based on the polymeric melt flow characteristics through particle tracking applied. Dispersive mixing and distributive mixing characteristics were evaluated by using the statistical post-processor program of POLYSTAT (ANSYS, Inc., USA). By modifying rotational speed, radius, pitch and eccentricity in the numerical simulation model, the effects of process conditions and structural parameters on the mixing characteristics of the ERE were studied. We suggest that the results of the study can be used for optimizing the structure design and guiding production.

2. Numerical Simulation

2.1. Models and Governing Equation. Considering the symmetry and periodicity of the model, only the 2 pitches length of the rotor geometric model was built to decrease the computational costs of the simulations. The simplified geometry model is illustrated in Figure 2.

The initial position of a rotor with radius R is located at the top of the stator inner cavity which is the fluid field. The distance between the center of the rotor and the center of the stator is 2 times the eccentricity e. The pitch of the stator inner cavity is 2 times the rotor pitch p. The clearance between the rotor and the stator h is 0.3 mm. The influence of structural parameters on mixing properties is explored by changing radius R, eccentricity e and pitch p.

As described above, the eccentric rotor rotates clockwise around its axis in the right-hand coordinate system, and counterclockwise around the center of the stator. The rotational speed ω and revolution speed have the opposite direction but the same size. The relationship between velocity v at the center point of rotor and time t can be described as follows:

$$v = \pm 2e \cdot (\cos \omega t - 1). \quad (1)$$

This complex motion can be specified using a user-defined function (UDF). Meanwhile, the model was meshed into hexahedral elements with the pre-processor GAMBIT from ANSYS, Inc., as shown in Figure 3.

The model, whose mesh was processed with the mesh superposition technique both to simplify the mesh generation and to avoid any remeshing technique or sliding meshes. It is necessary to refine the whole mesh as much as possible to improve the quality of the mesh, because the spiral structure of the stator cavity and the rotor models are easy to cause the high distortion of the three-dimensional mesh. In addition, the gap thickness in the local boundary area during the rotor movement is only 0.3 mm. In order to ensure the accuracy of simulation, the boundary layer size should increase along the radial direction of the stator cavity wall and the rotor outer surface. Finally, the stator cavity mesh of 512000 elements and 526305 vertices, and the rotor mesh of 327680 elements and 338065 vertices. The "EquiAngle Skew" in Gambit is 0–0.45 and 0–0.4, respectively, which shows that the mesh quality is well. "EquiAngle Skew" is an index for evaluating mesh quality.

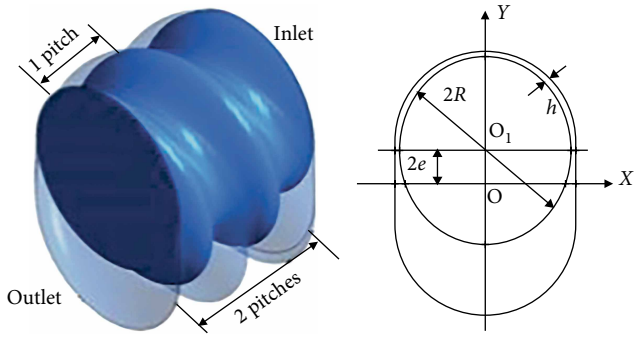

Figure 2: Geometry model of rotor and flow domain in melt conveying section.

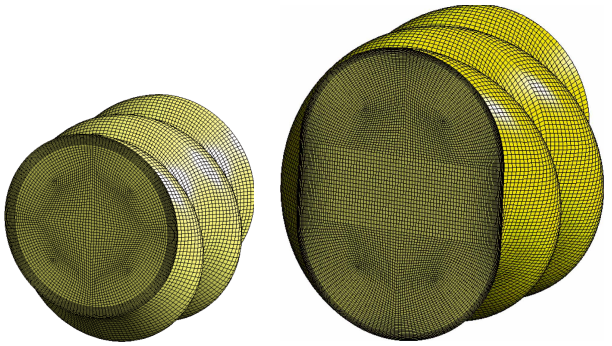

Figure 3: Mesh models of melt conveying in the ERE rotor (a) and stator cavity (b).

The closer it approaches 0, the better the mesh quality. At the initial time, the POLYFUSE module is used to combine the rotor mesh and stator cavity mesh, and the rotor mesh is moved to the top of the stator cavity as the initial position, with a gap between the two. The flow domain consists of stator and ERE rotor is filled by polymer melt in the simulation.

To perform numerical simulation of the melt flow characteristics in the ERE, some assumptions were made as follows:

(1) The flow is laminar.
(2) The flow is isothermal.
(3) The fluid is incompressible and purely viscous, nonnewtonian.
(4) No-slip near the wall.
(5) Neglecting the inertia and gravitational forces.

Based on the assumptions for the numerical simulation, the governing equations could be described as follows:

Based on the assumptions above the control equations are as follows:

$$\text{Continuity equation}: \quad \nabla \cdot \boldsymbol{u} = 0, \quad (2)$$

$$\text{Momentum equation}: \quad \nabla \cdot \boldsymbol{\tau} - \nabla p = 0, \quad (3)$$

$$\text{Constitutive equation}: \quad \boldsymbol{\tau} = 2\eta \boldsymbol{D}, \tag{4}$$

$$\boldsymbol{D} = \left(\frac{\nabla \boldsymbol{u} + (\nabla \boldsymbol{u})^T}{2} \right), \tag{5}$$

where $\boldsymbol{u}$ is the velocity vector; $\boldsymbol{\tau}$ is the stress tensor; p is the melt pressure; η is the melt viscosity; $\boldsymbol{D}$ is the deformation rate tensor; T is transpose. And the boundary conditions of the flow domain simulation were as follows:

Inflow and outflow: $F_n = 0$, $F_t = 0$;
Inner wall of stator: $V_n = 0$, $V_t = 0$;
Rotor: defined as moving part, the law of motion is defined by UDF.

Where F_n is normal force, F_t is tangential force, V_n is normal velocity, V_t is tangential velocity. In mixing simulation task, 1000 material points were located initially at the inflow, the inner wall of stator was nonpenetrable.

2.2. Material and Methods. In this paper, we select PP (N-Z30S, Sinopec Guangzhou branch) as simulation material. As an initial approximation, the PP melt was simplified as an isothermal and generalized newtonian fluid with a Bird–Carreau law relationship describing its shear-thinning behavior.

$$\eta = \eta_\infty + (\eta_0 - \eta_\infty)\left(1 + {\lambda_t}^2 \dot{\gamma}^2\right)^{(n-1)/2}, \tag{6}$$

where η is the shear viscosity, η_∞ is infinite-shear-rate viscosity, η_0 is zero-shear-rate viscosity, λ_t is natural time, $\dot{\gamma}$ is shear rate and n is the power-law index. The parameters in the Bird–Carreau law were determined in a rotary rheometer as follows: $\eta_0 = 1162\text{Pa} \cdot \text{s}$, $\eta_\infty = 0.23 \times 10^{-3}$, $\lambda_t = 0.67$ s and $n = 0.64$. The shear viscosity curve and the fitting curve of the Bird–Carreau model as shown in Figure 4.

In this paper, using the transient, isothermal model and iteration solution, mini-element interpolation was used for the velocity, linear interpolation for the pressure, Pichard interpolation for the viscosity. Discretize the Equations (2)–(6) and solve the discretized equations using the implicit Euler method.

Many ways of characterizing mixing have been proposed over the years, with no one method being able to quantify all aspects of mixing for every process. Given a motion $\boldsymbol{x} = \chi(\boldsymbol{X}, t)$ where initially $\boldsymbol{X} = \chi(\boldsymbol{X}, 0)$ for an infinitesimal material line segment $d\boldsymbol{x} = \boldsymbol{F} \cdot d\boldsymbol{X}$ located at position $\boldsymbol{x}$ at time t where the deformation tensor is $\boldsymbol{F} = \nabla \boldsymbol{\chi}$, the length of stretch of a material line is defined as $\lambda = |d\boldsymbol{x}|/|d\boldsymbol{X}|$. Then the local efficiency of mixing e_λ is then defined as [10, 11]:

$$e_\lambda = \frac{\dot{\lambda}/\lambda}{(\boldsymbol{D} : \boldsymbol{D})^{1/2}} = \frac{D\ln\lambda/Dt}{(\boldsymbol{D} : \boldsymbol{D})^{1/2}}, \tag{7}$$

where the rate of strain tensor $\boldsymbol{D}$ is the symmetric part of the velocity gradient tensor. This efficiency quantitatively characterizes the stretching rate during mixing and can be thought of as the fraction of the energy dissipated locally that is used to stretch fluid elements. The time averaged efficiency is defined as [12]:

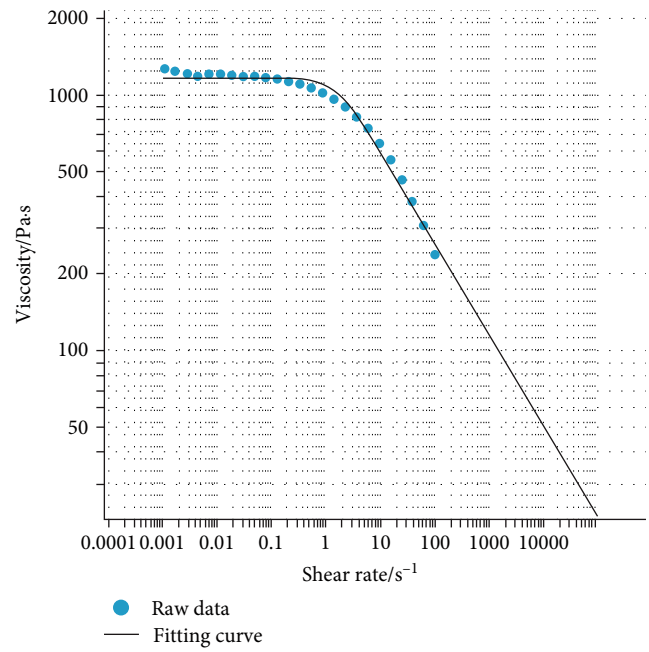

Figure 4: The fitting curve of PP melt under the Bird–Carreau model.

$$\langle e_\lambda \rangle = \frac{1}{t} \int_0^t e_\lambda dt. \tag{8}$$

For 3D flows, let define an infinitesimal surface "dA" with a normal direction $\hat{N}$. With time, this surface deforms; at time t, this surface is noted "da", with a new normal direction $\hat{n}$. The area stretch S is the ratio of the deformed surface "da" at time t, over the initial surface "dA", $S = S(X, \hat{N}, t) = da/dA$, then we have [13, 14]:

$$e_S(X, \hat{N}, t) = \frac{\dot{S}/S}{D}, \tag{9}$$

$$\langle e_S \rangle (X, \hat{N}, t) = \frac{1}{t} \int_0^t e_S(X, \hat{N}, t) dt. \tag{10}$$

Extensional flow is much more efficient to break up droplets than shear flow. In order to estimate the fraction of the matter going through extension, the mixing index M was defined as follows [15, 16]:

$$M = \frac{\dot{\gamma}}{\dot{\gamma} + \omega}, \tag{11}$$

where $\dot{\gamma}$ the equivalent shear rate, ω is the magnitude of the vorticity vector. The mixing index can range from 0 to 1. At 0, the flow is locally a plug flow; at 0.5, the flow is locally a pure shear flow; while at 1, the flow is locally a pure extensional flow [17, 18].

The flow field inside the mixing section of the ERE was simulated by POLYFLOW. After the flow field was computed,

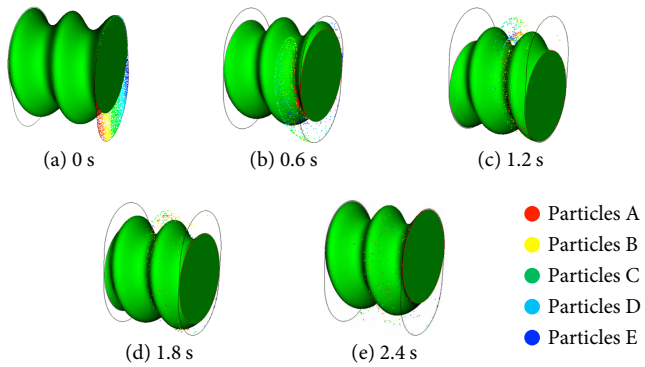

Figure 5: Dispersion of particles in one rotation cycle.

a mixing task was executed by using the mixing module program to calculate the trajectories of 1000 material points which were located initially at the entrance of melt conveying in the ERE. Then, the mixing characteristic parameters inside the flow domain were analyzed using POLYSTAT statistical module to evaluate the local value of the mixing characteristic parameters respectively.

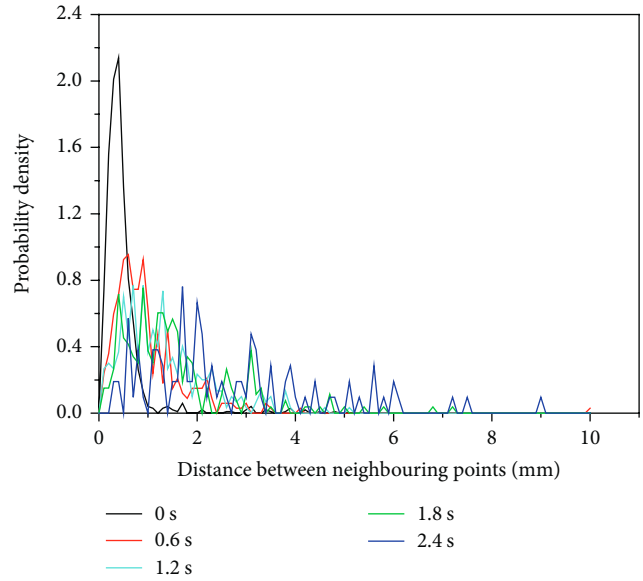

Figure 6: Distribution functions of distance between neighbouring points at different times.

3. Results and Discussion

3.1. Visualization of Mixing Process. The EXTRACT function of POLYSTAT can be used to observe the trajectory of the tracking particles at every moment and the results can be used to evaluate the dispersion of particles in the flow field. The images of the tracking particles in one rotation cycle shown in Figure 5. The parameters for this simulation are as follows: radius R = 17 mm, pitch p = 16 mm, eccentricity e = 3 mm, rotational speed n = 25 r/ min. The 1000 tracking particles with different colors were fed instantaneously in the inflow of the melt at 0 s. Five different colors of particles represent different materials. The particles gradually began to disperse with the rotation of the rotor. After a rotation period, the particles with different colors have a good dispersion effect. This indicates that the ERE had a great dispersive capability.

The distribution functions of distance between neighbouring points at different times could be calculated in the Figure 6.

At start, all points were close together: this corresponds to the black peak curve in the left chart. Next, as points distributed, the distance between particles increased with the rotation of the rotor. Their inter-distance increased leading to a widening and a flattening of the distribution functions. This shows that as distribution improves, the distribution of particles is random in the extruder.

The percentile shows the results of the application of mathematical statistics to the mixing characteristic parameters. In statistics, a percentile is the value of a variable below which a certain percent of observations fall. For example, If the maximum shear rate corresponding to the 10th percentile is 100/s, it means that the maximum shear rate experienced by 10% of the particles is less than or equal to 100/s, and the maximum shear rate experienced by 90% of the particles is greater than 100/s. In this paper, the influence of different rotor rotational speed and structural parameters on mixing performance was studied based on the maximum shear rate, stretching rate, time averaged efficiency, mixing index and the residence time distribution. The results shown as 10%, 50%, 90% percentile curves to give a clearer distribution of the mixing characteristic parameters. Three percentiles represent the largest, middle and smaller values, respectively.

3.2. The Influence of Rotor Rotational Speed on Mixing Properties. The percentile of the mixing characteristic parameters with different rotational speeds was selected after a rotation cycle. The speed was set to 15, 25, 35, 45, and 55 r/min, respectively. And the basic dimensions of the model are as follows: radius R = 17 mm, pitch p = 13 mm, eccentricity between the stator and rotor e = 3 mm. The mixing characteristic parameters with different values for rotational speed are shown in Figure 7.

Figure 7 shows the maximum shear rate and maximum stretching rate in various percentiles of the particles experienced under the different rotational speeds. With the increase of the rotational speed, the maximum shear rate and stretching rate gradually increased for each of the three percentiles. When the percentile is 50%, the maximum shear rate and stretching rate increased the most from 35 r/min to 45 r/min. This shows that half of the particles experienced the fastest increase in the maximum stretching rate and shear rate. When the percentile is 90%, the increase of the maximum shear rate and stretching rate experienced from 35 r/min to 45 r/min and from 45 r/min to 55 r/min were the fastest. The speed of improving the mixing performance through comparative analysis three percentiles is the most obvious when the rotational speed is 45 r/min.

The maximum time averaged efficiency and mixing index experienced by the particles in the three percentiles under the different rotational speeds are shown in Figure 8. All the maximum time averaged efficiency cures in the graph were larger

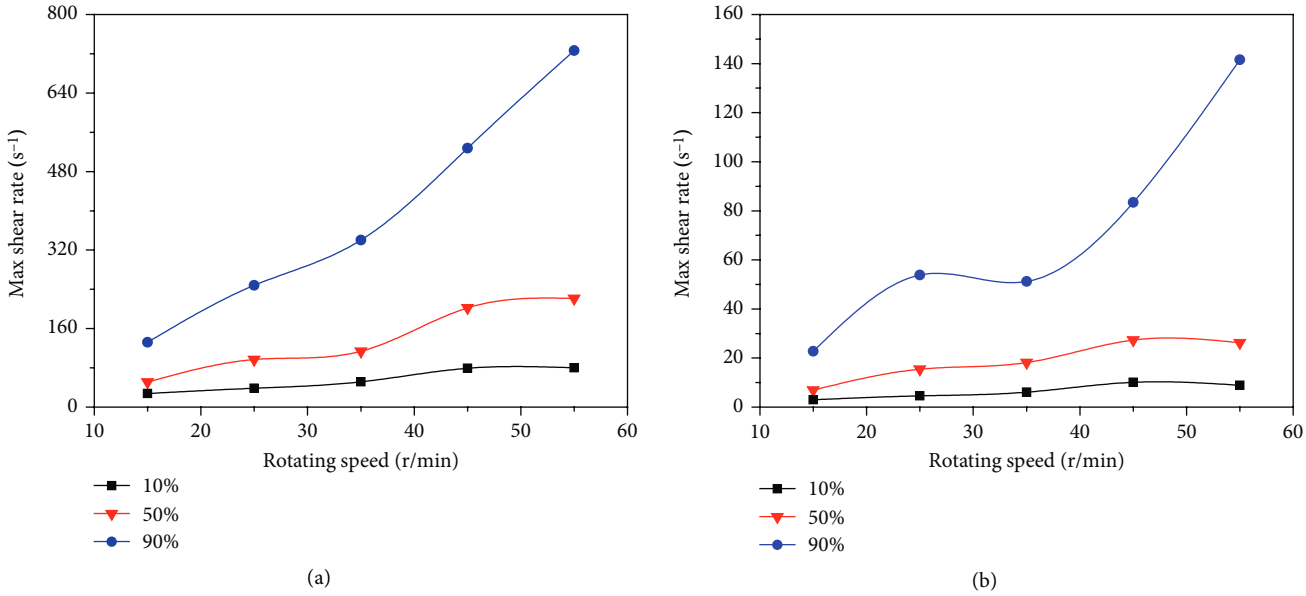

FIGURE 7: Influence of rotor rotational speed on the maximum shear rate (a) and stretching rate (b).

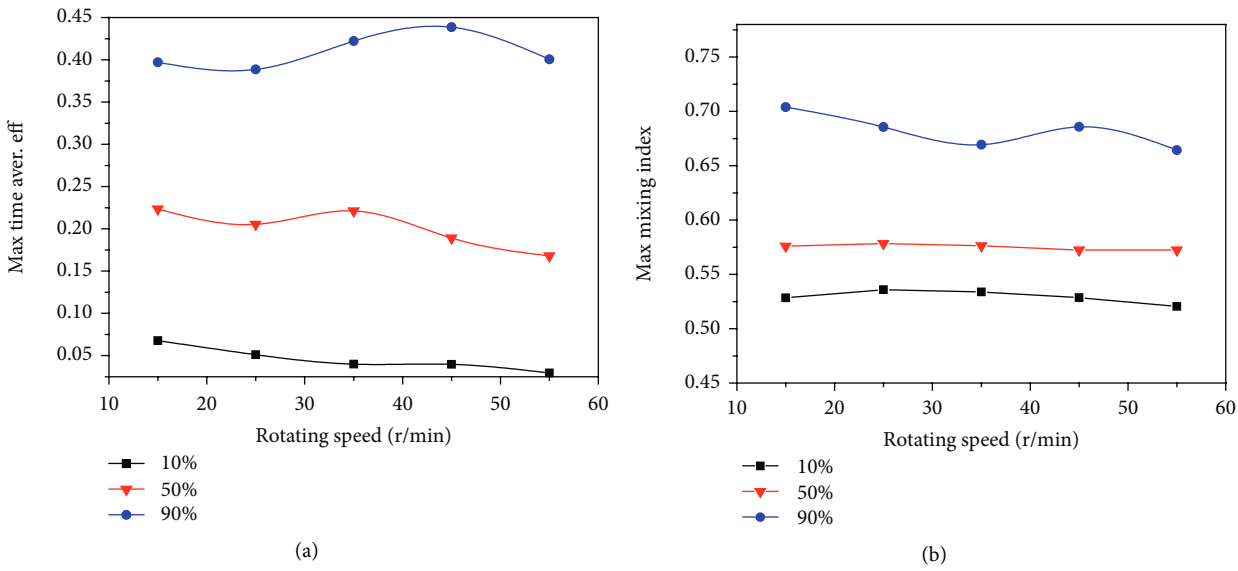

FIGURE 8: Influence of rotor rotational speed on the maximum time averaged efficiency (a) and mixing index (b).

than 0, indicating that almost all particles experienced the stretching flow. In the 90th percentile, the maximum time averaged efficiency were larger than 0.37 at the end of one cycle, which means in these particles about 37% of the mechanical energy was used to generate stretching. When the speed is 45 r/min, the mechanical energy used to stretch the melt is most. The maximum mixing indexes for rotational speed were close in the 10th percentile and the 50th percentile. The maximum mixing indexes under different speeds were greater than 0.67 in the 90th percentile, which means that more particles experienced extensional flow. In the 90th percentile, the maximum mixing index showed a zigzag change with the speed increased, and reached the maximum at the speed of 45 r/min.

When the rotational speed increased, the intensity of flow field strengthened, but the time for the material to stay in the extruder will be reduced. Therefore, the residence time distribution should be taken into account in evaluating the mixing performance.

There were more than one wave peak in each residence time distribution curve, indicating that the particles left the exit in a batch. And the time of the first wave peak on each curve was about in the 3/4 rotation period. In addition, the overall width of residence time distribution narrowed with the rotational speed increased. The residence time distribution of 15 r/min and 25 r/min was obviously better than other rotational speeds, and the residence time distribution width of 45 r/min was greater than 35 r/min or 55 r/min by observing

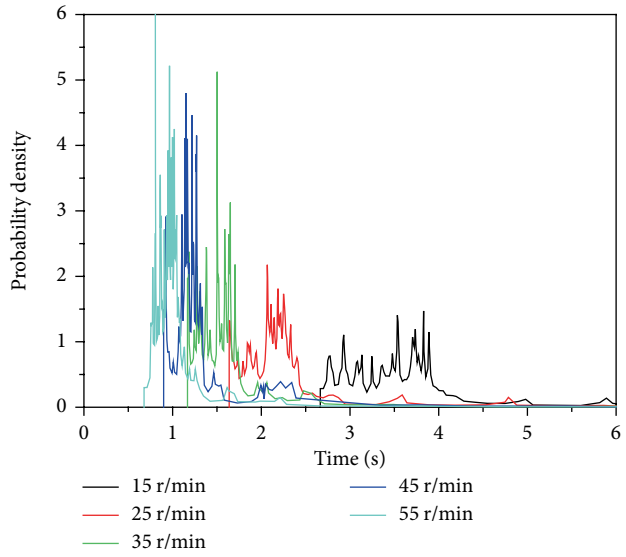

FIGURE 9: Influence of rotor rotational speed on residence time distribution.

the width of the peak residence time distribution curve in the Figure 9.

In general, the shear rate and the stretching rate increased with the increase of the rotational speed, and the fastest increase from 35 r/min to 45 r/min. The mixing index and the time average mixing efficiency were not obviously affected by the rotational speed, and the mixing index and the time averaged mixing efficiency reached maximum near the 45 r/min. The residence time of the material in the ERE was shortened as the speed increased. The residence time of 45 r/min is longer when compared to 35 r/min and 55 r/min. In summary, the ERE has the best mixing performance when the rotational speed is 45 r/min. The result of numerical simulation is in agreement with the experimental results of Lin [6]. He used eccentric rotor extruder to process PP/POE (70/30) blends. The mixing of POE elastomer particles in PP matrix was characterized by SEM and mechanical properties test. Through the experiment, it found that the mixing effect was the best when the rotating speed was 45 r/min, which was consistent with the numerical simulation results in this paper. It validated the reliability of the numerical simulation method to study the mixing performance of eccentric rotor extruder.

3.3. The Influence of Rotor Radius on Mixing Properties. The structural factors of the equipment have an important influence on the practical application of the plastic processing equipment. In order to observe the influence of the rotor radius on the mixing performance of the ERE, select different values for radius such as 13, 15, 17, 19, and 21 mm. The rotational speed was 45 r/min and other structural factors were the same as those of the previous basic models. The influence of rotor radius on the maximum shear rate and stretching rate is shown in Figure 10.

There was an evident increase for the maximum shear rate and stretching rate increased in the 90th percentile, and slight change in the 10th and 50th percentiles. The proportion of

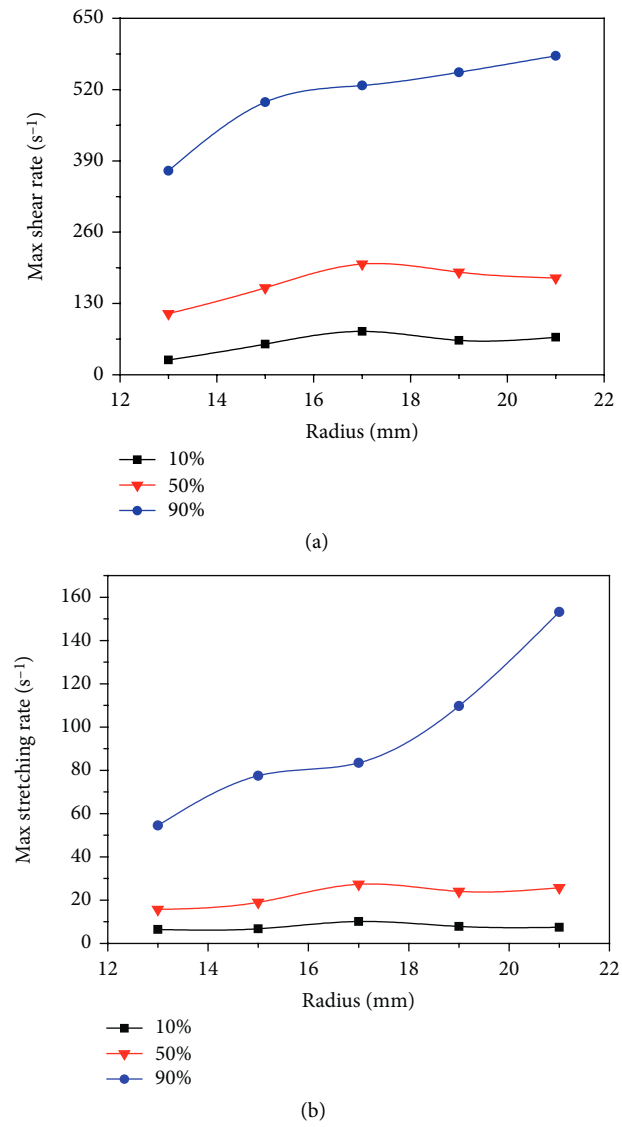

FIGURE 10: Influence of rotor radius on the maximum shear rate (a) and stretching rate (b).

particles at high shear rate and stretching rate increased with the increase of the radius, especially the stretching rate increased more obvious. This is because the increase of the radius will increase the radial length of the rotor while the rotational speed and other structural parameters remain unchanged. The volume and weight of the rotor will become larger, and the force of the rotor on the melt will be greater at the same speed, so the maximum shear rate and stretching rate experienced by the particles will increase. High shear rate and stretching rate are good for the breaking up of the material particles into small ones.

The effect of radius on the maximum time averaged efficiency and mixing index, as shown in Figure 11. In the 10th percentile and the 50th percentile, the maximum time averaged mixing efficiency and mixing index did not change significantly with the increase of rotor radius. But the maximum time-averaged mixing efficiency and mixing index in the 90th percentile showed an upward trend as a

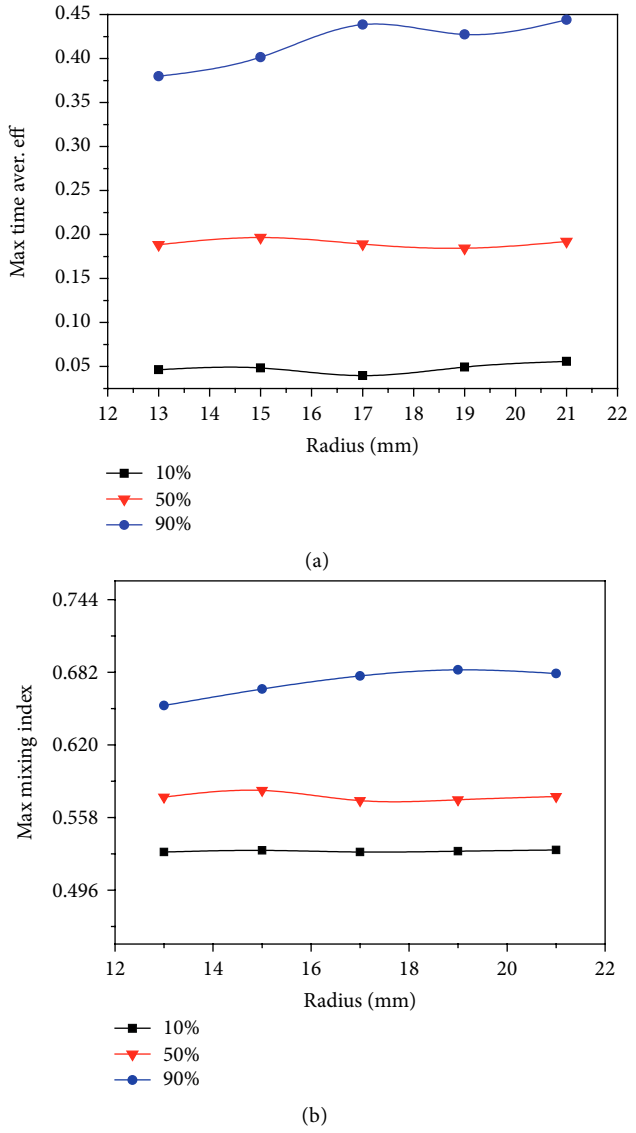

Figure 11: Influence of rotor radius on the maximum time averaged efficiency (a) and mixing index (b).

whole. Meanwhile, the maximum time averaged mixing efficiency and mixing indexes of various percentiles were almost all above 0 and 0.5 respectively, illustrating that there was a strong stretching flow field in ERE with different radius. Because although the size of the geometric model changed, a strong stretching flow field could still be generated based on topological structure and motion law remain unchanged.

It can be seen from the Figure 12 that the cures of residence time distribution under different radius almost coincided. Thus, we can make the conclusion that the change of the radius had little impact on residence time distribution. In summary, the maximum shear rate, stretching rate, time averaged efficiency and mixing index increased in the 90th percentile, but changed slightly in the 10th and 50th percentiles when the radius increases. The change of the radius can significantly affect the upper limit of the mixing characteristic

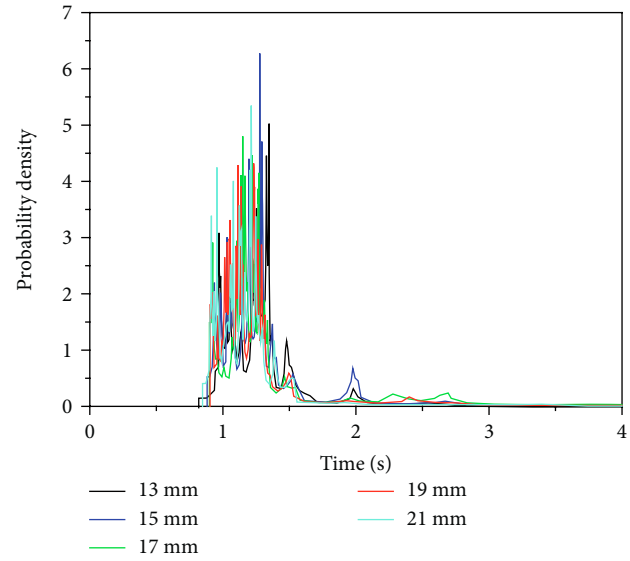

Figure 12: Influence of rotor radius on residence time distribution.

parameters which indicates that the increase of radius can promote the mixing performance of the ERE. At the same time, there was a particularly small impact on residence time distribution with the change of radius.

3.4. The Influence of Rotor Pitch on Mixing Properties. For the sake of studying the influence of pitch on the mixed performance of ERE, the pitch was selected as 12, 14, 16, 18, and 20 mm, respectively. Just as the control variable method which previous mentioned, other conditions remained unchanged. For example, there were rotational speed 45 r/min, radius $R = 17$ mm, pitch $p = 13$ mm, eccentricity $e = 3$ mm. Influence of rotor pitch on the maximum shear rate and stretching rate as shown in Figure 13.

With the change of pitch, the maximum shear rate and stretching rate changed a little in the 10th and 50th percentile. It can be seen that the maximum shear rate and stretching rate in the 90th percentile declined and the rate of decline was various which indicated that the increase of pitch reduced the mixing performance of the ERE. This is due to the fact that the curvature of the helical surface in the rotor and stator cavity decreases and the force on the melt decreases with the increase of the pitch of the rotor while the eccentricity and the radius of the rotor remain unchanged.

The maximum time averaged efficiency and mixing index experienced by the particles under different pitches shown in Figure 14. The maximum time averaged efficiency decreased fluctuated but did not change significantly. The maximum mixing index under the different pitches decreased in 90th and 50th percentiles, which means that the proportion of extensional flow in melt decreased gradually. This may be associated with the spiral lines of the stator and the rotor soothed from steep with the increase of pitch. When the pitch increased infinitely, the geometric shape of the rotor and stator cavity is closer to the cylinder. At this time, the pressure fluctuation of the melt decreased, which made the volume tension deformation and extensional flow decrease.

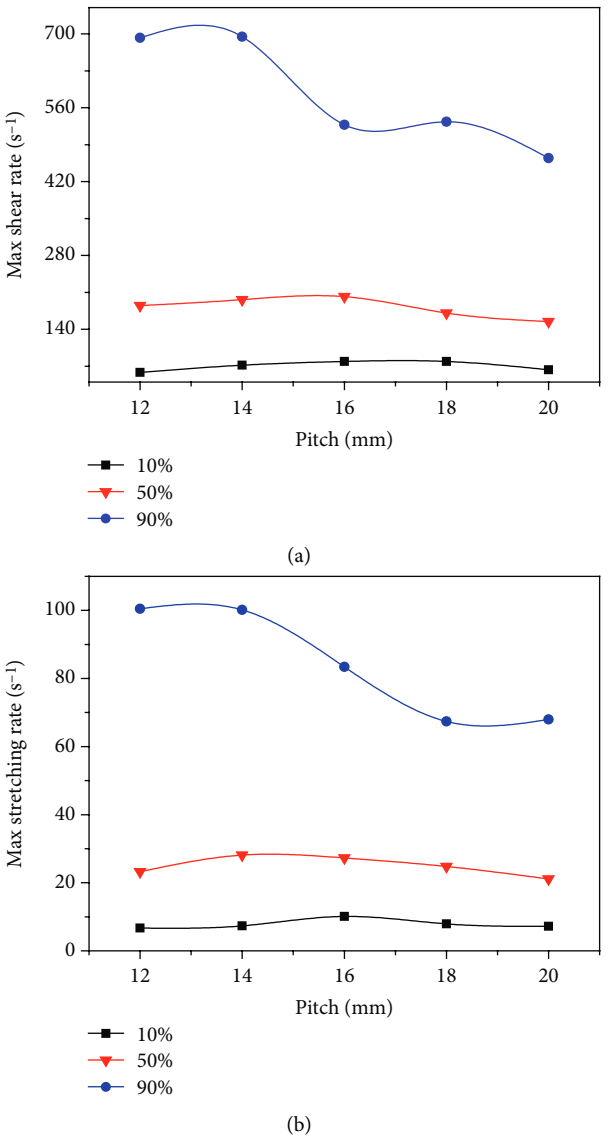

Figure 13: Influence of rotor pitch on the maximum shear rate (a) and stretching rate (b).

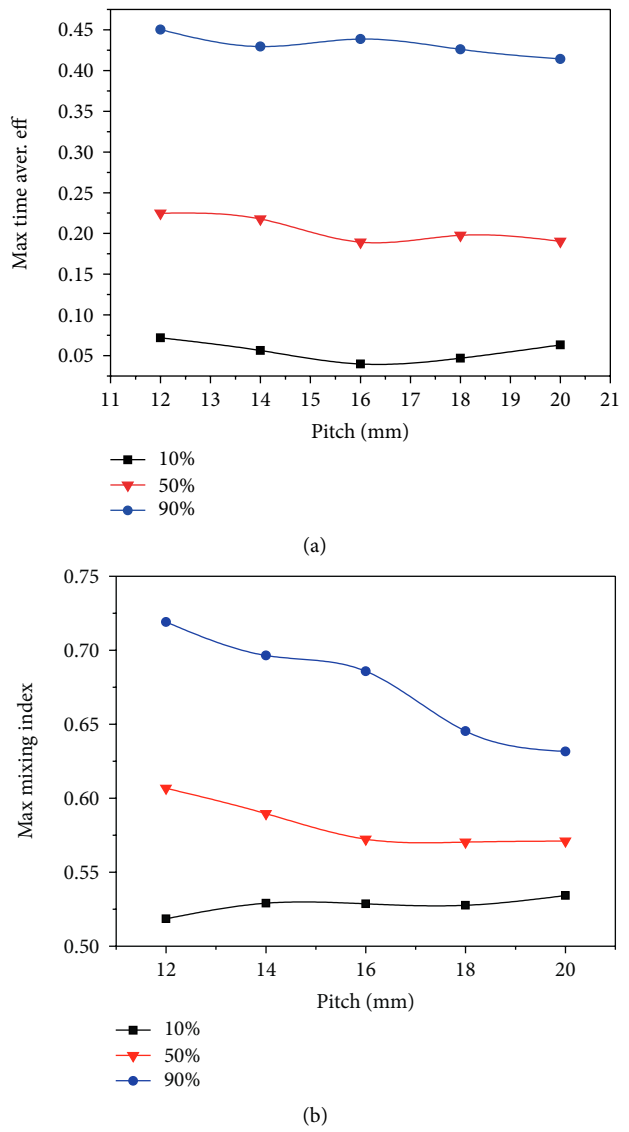

Figure 14: Influence of rotor pitch on the maximum time averaged efficiency (a) and mixing index (b).

There was little change about the curves of residence time distribution under different pitches in Figure 15. As a result, no matter how the pitch changed, the residence time distribution was almost the same. In summary, the maximum shear rate, stretching rate, and mixing index showed a stepped downward trend in the 90th percentile, which indicates that the increase of pitch can reduce the mixing performance of the ERE.

3.5. The Influence of Eccentricity on Mixing Properties. The eccentricity e between the rotor and stator is one of the key structural parameters for the ERE. The size of the eccentricity directly affects plastic melt volume changing during the machining process. The eccentricity was selected as 1.0, 1.5, 2.0, 2.5, and 3.0 mm. Influence of eccentricity on the maximum shear rate and stretching rate as shown in Figure 16.

There was an evident increase for the maximum shear rate increased in the 50th and 90th percentiles. It is not obvious for the maximum shear rate changed in the 10th percentile. The maximum stretching rate increased obviously in the 90th percentile. The proportion of particles at high shear rate and stretching rate increased with the increase of the eccentricity. When the eccentricity increases, the height of chambers between the rotor and stator cavity increases along the radial direction, and the geometric shape of the rotor and stator cavity becomes more sharp and convex. Therefore, the force produced by ERE on the melt increases and improves blending effect with the increase of eccentricity.

The maximum time averaged efficiency and mixing index under different eccentricities are shown in Figure 17. It can be found clearly from the figure that the maximum time averaged efficiency and mixing index increased in various percentiles. When the eccentricity increased, the radial travel and centrifugal inertia force of the rotor increased, so the maximum time averaged mixing efficiency increased due to the mechanical dissipation acting on the tensile flow field raised. The increase of eccentricity would increase the axial eccentricity of the cross

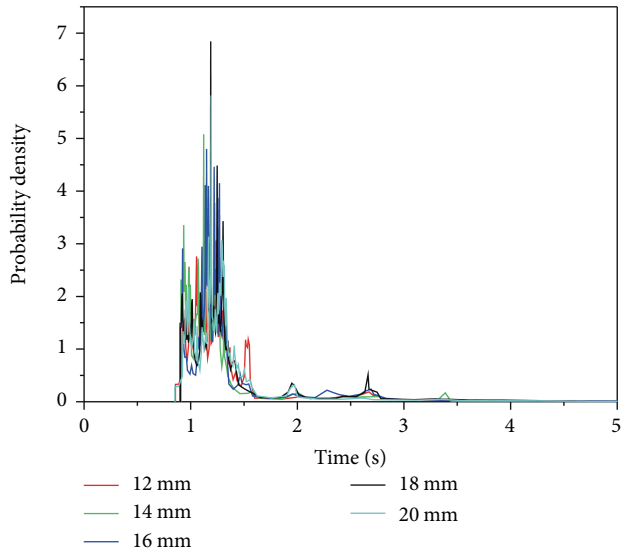

Figure 15: Influence of rotor pitch on residence time distribution.

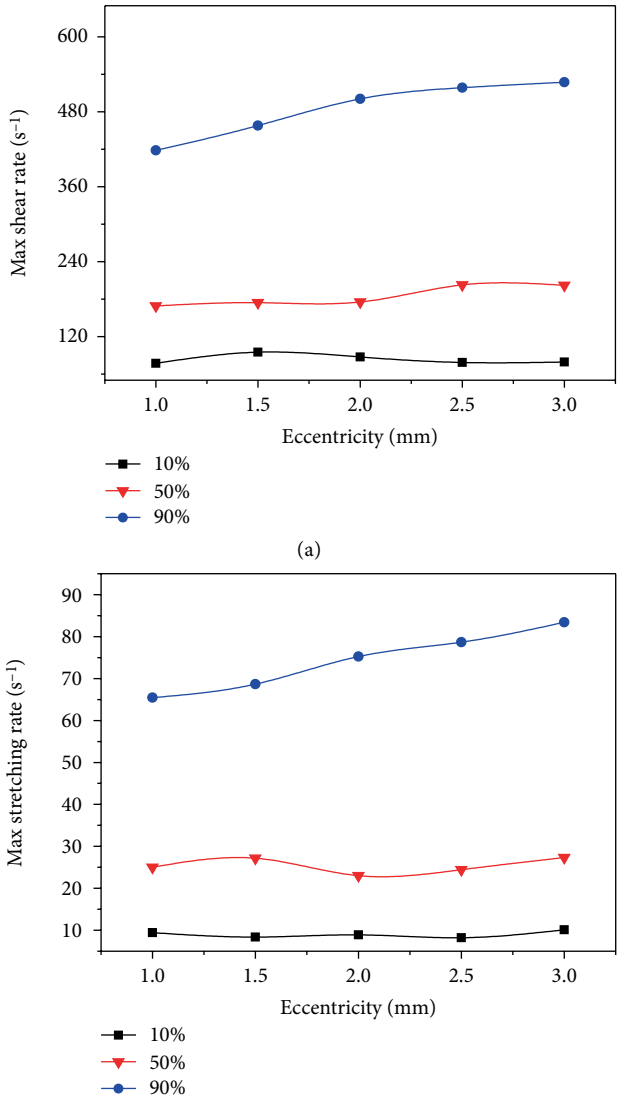

Figure 16: Influence of eccentricity on the maximum shear rate (a) and stretching rate (b).

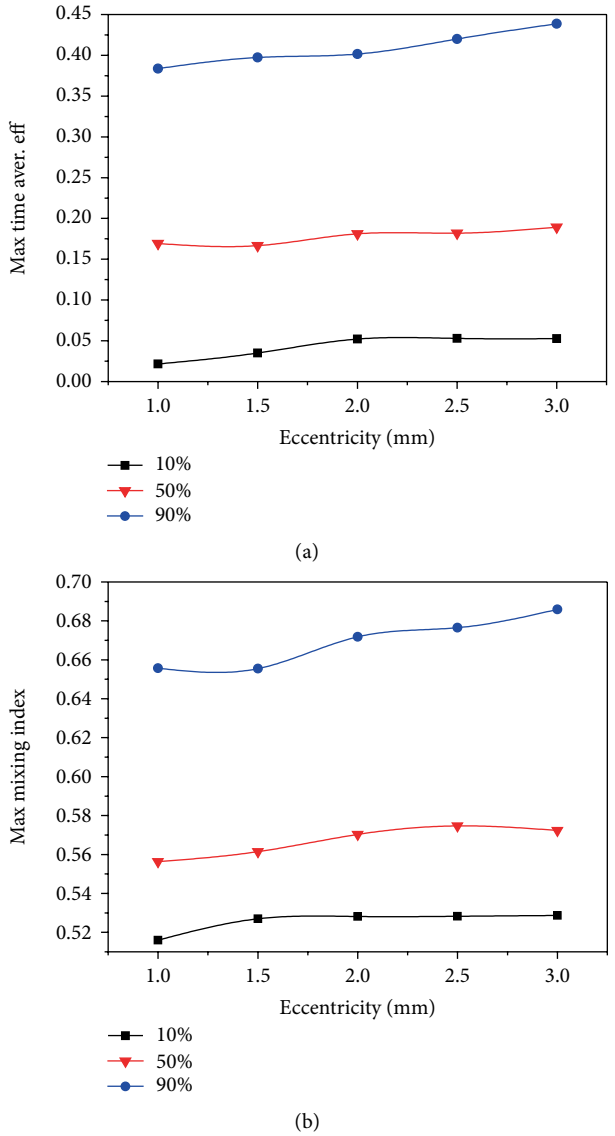

Figure 17: Influence of eccentricity on the maximum time averaged efficiency (a) and mixing index (b).

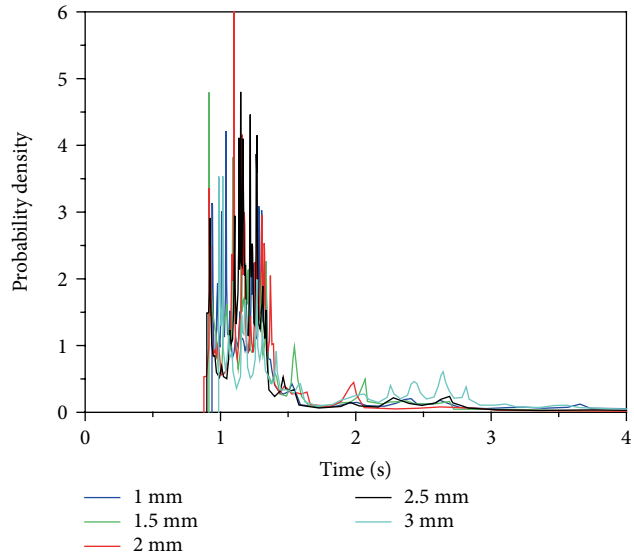

Figure 18: Influence of eccentricity on residence time distribution.

section of the rotor and stator cavity, and the rate of volume change of the enclosed chamber increased could strength the pulsed volume deformation of melt, so the stretching flow increased. Above explanation suggests that increasing the eccentricity is beneficial to improve the mixing performance.

It can be seen from the Figure 18 that the eccentricity had little effect on the residence time distribution. The distribution of the residence time is almost irrelevant to the structural factors, but greatly influenced by the rotational speed.

4. Conclusions

The influence of different rotor rotational speed and structural parameters on mixing performance was studied based on some mixing characteristic parameters such as the maximum shear rate, stretching rate, mixing index, time averaged efficiency and the residence time distribution. The intensity of shear and elongational flow strengthened when the rotational speed increased, but the time for material to stay in the ERE will be reduced. The ERE has the best mixing performance when the rotational speed is 45 r/min overall consideration, because it has the highest flow intensity and the optimal residence time distribution. In the aspect of structural parameters, the increase of radius and eccentricity can promote the mixing performance of the ERE. On the contrary, the mixing capacity reduced with the increase of the pitch. At the same time, there was a particularly small impact on residence time distribution with the change of structural parameters.

Data Availability

All data included in this study are available upon request by contact with the corresponding author.

Conflicts of Interest

The authors declare that they have no conflicts of interest.

Acknowledgments

This work was supported by the National Key Research and Development Program of China under Grant No. 2016YFB0302302 and the State Key Laboratory of Materials Processing and Die & Mould Technology Huazhong University of Science and Technology under Grant P2018-009.

References

[1] J. P. Qu, G. Z. Zhang, and X. C. Yin, "Volume pulsed deformation plasticating and conveying method and device by eccentric rotor," 2017, US2017/0080619 A1.

[2] W. Zou, R. Y. Chen, G. Z. Zhang, H. C. Zhang, and J. P. Qu, "Mechanical, thermal and rheological properties and morphology of poly (lactic acid)/poly (propylene carbonate) blends prepared by vane extruder," *Polymers for Advanced Technologies*, vol. 27, no. 11, pp. 1430–1437, 2016.

[3] T. Wu, R. R. Tong, F. Qiu, D. Yuan, G. Z. Zhang, and J. P. Qu, "Morphology, rheology property, and crystallization behavior of PLLA/OMMT nanocomposites prepared by an innovative eccentric rotor extruder," *Polymers for Advanced Technologies*, vol. 29, no. 1, pp. 41–51, 2018.

[4] T. Wu, D. Yuan, F. Qiu, R. Y. Chen, G. Z. Zhang, and J. P. Qu, "Polypropylene/polystyrene/clay blends prepared by an innovative eccentric rotor extruder based on continuous elongational flow: analysis of morphology, rheology property, and crystallization behavior," *Polymer Testing*, vol. 63, pp. 73–83, 2017.

[5] C. L. Cao, X. C. Chen, J. X. Wang et al., "Structure and properties of ultrahigh molecular weight polyethylene processed under a consecutive elongational flow," *Journal of Polymer Research*, vol. 25, no. 1, p. 16, 2018.

[6] X. K. Lin, "*Study on properties of PP/POE composites based on fluctuation [Master Degree]*," South China University of Technology, 2012.

[7] T. Chen, Y. Hao, X. Chen et al., "Mixing ability examination of three different rotor cross sections and rotor geometry quantification with pressurization coefficient," *Journal of Applied Polymer Science*, vol. 135, no. 37, p. 46623, 2018.

[8] B. Xu, H. Yu, and L. S. Turng, "Distributive mixing in a corotating twin screw channel using Lagrangian particle calculations," *Advances in Polymer Technology*, vol. 37, no. 6, pp. 1–15, 2017.

[9] W. Cheng, Y. Ye, S. Jiang, J. Wang, X. Gu, and L. Feng, "Mixing intensification in a horizontal self-cleaning twin-shaft kneader with a highly viscous Newtonian fluid," *Chemical Engineering Science*, vol. 201, pp. 437–447, 2019.

[10] S. K. Jia, J. P. Qu, W. F. Liu et al., "Thermoplastic polyurethane/polypropylene blends based on novel vane extruder: a study of morphology and mechanical properties," *Polymer Engineering and Science*, vol. 54, no. 3, pp. 716–724, 2014.

[11] T. L. Liu and Y. X. Du, "Numerical simulation on the mixing behavior of pin unit under vibrant enhancement," *Polymer-Plastics Technology and Engineering*, vol. 50, no. 12, pp. 1231–1238, 2011.

[12] Z. B. Xu, Z. Y. Xu, J. P. Cao, X. D. Ruan, and R. J. Chen, "Development and characterization of a novel polymer microchannel tube," *Polymer-Plastics Technology and Engineering*, vol. 53, no. 14, pp. 1442–1449, 2014.

[13] Polystat User's Guide, *Chapter 2: The Mixing Theory*, pp. 11–19, Fluent Inc., Lebanon, New Hampshire, 2005.

[14] Polyflow Examples Manual, *Example 37: Mixer 2-D*, pp. 1–3, Fluent Inc., Lebanon, New Hampshire, 2005.

[15] H. L. Xie, J. S. Wen, D. J. Fan, S. K. Lei, S. C. Jiang, and X. L. Zhou, "Numerical simulation of mixing characteristics and energy consumption in vane extruders with different structure parameters," *Journal of Macromolecular Science, Part B Physics*, vol. 56, no. 6, pp. 395–408, 2017.

[16] R. K. Connelly and J. L. Kokini, "Examination of the mixing ability of single and twin screw mixers using 2D finite element method simulation with particle tracking," *Journal of Food Engneering*, vol. 79, no. 3, pp. 956–969, 2007.

[17] J. S. Wen, Y. H. Liang, and Z. M. Chen, "Numerical simulation of elongational flow in polymer vane extruder," *Advanced Materials Research*, vol. 421, pp. 415–418, 2012.

[18] S. Yamada, K. Fukutani, K. Yamaguchi et al., "Analytical and experimental evaluation of dispersive mixing performance of special rotor segments in a corotating twin-screw extruder," *Polymer – Plastics Technology and Engineering*, vol. 55, no. 15, pp. 1577–1585, 2016.

Hindawi
Advances in Polymer Technology
Volume 2019, Article ID 2318347, 11 pages
https://doi.org/10.1155/2019/2318347

Research Article

Enhancing Mechanical and Thermal Properties of Polyurethane Rubber Reinforced with Polyethylene Glycol-g-Graphene Oxide

Li Wang,[1] **Wen Fu**,[2] **Wenlong Peng**,[2] **Haotuo Xiao**,[2] **Shenglin Li**,[2] **Jianning Huang**,[2] **and Cuiwen Liu**[2]

[1]*College of Chemical Engineering, Guangdong University of Petrochemical Technology, Maoming 525000 Guangdong, China*
[2]*College of Material Science, Guangdong University of Petrochemical Technology, Maoming 525000 Guangdong, China*

Correspondence should be addressed to Wen Fu; a449192213@163.com

Received 5 June 2019; Accepted 21 July 2019; Published 5 August 2019

Guest Editor: Hong Liang

This paper attempted to achieve the purpose of increasing the tensile strength and toughness of polyurethane rubber (PUR) simultaneously by introducing polyethylene glycol (PEG) onto the surface of graphene oxide (GO) to introduce hydrogen bond interactions into the PUR-GO system. GO was grafted with PEG and added to PUR by mechanical blending. The polyethylene glycol-g-graphene oxide (MGO) was characterized by infrared spectroscopy, Raman spectroscopy, X-ray diffraction, and thermogravimetric analysis. The PUR/MGO composites were tested by tensile testing machine, thermogravimetric analysis, dynamic thermal analysis, and scanning electron microscopy. The results demonstrated that PEG was successfully grafted onto the surface of GO and the grafting rate was about 37%. The grated PEG did not affect the crystalline structure of GO. The addition of MGO could improve the thermal stability of PUR vulcanizate. After the addition of GO, the glass transition temperature (T_g) of vulcanizate was shifted to higher temperature. However, the T_g of vulcanizate reinforced by MGO was shifted to lower temperature. The strength and toughness of vulcanizate were significantly improved by adding MGO. The reason was that the hydrogen bond interactions between MGO and PUR were destroyed and the hidden length was released during the strain process. A lot of energy was consumed, and thus the strength and toughness of PUR vulcanizate were improved.

1. Introduction

Generally, raw rubber without reinforcer has poor mechanical properties. For most practical applications, the rubber should be reinforced with some additives. Carbon black and silica are the commonly used reinforcing agents. In recent years, graphene has been studied as a new type of reinforcing agent for rubber. The Young's modulus of monolayer graphene is about 1.1 TPa and the fracture strength is 125 GPa [1]. Hence, graphene should have promising prospect in the field of rubber reinforcement [2–4]. However, it was reported that graphene could increase the strength of rubber matrix but will damnify the toughness and ductility [5–7]. How to optimize the strength and toughness of graphene reinforced rubber is still an important issue in the field of material science.

Natural biomaterials such as spider silk and animal bone always exhibit an amazing balance among the strength, toughness, and ductility. Studies have revealed that it is due to the sacrificial bonds and hidden length at the soft-hard interface, so these natural biomaterials can achieve both high strength and ductility [8–10]. Inspired by the structure of these natural biomaterials, some reports about constructing sacrificial bonds at the interface between inorganic filler and elastomer to increase the strength and toughness of materials have emerged recently. The strength of noncovalent sacrificial bonds, such as hydrogen bond [11, 12], π-π conjugate interactions [13], π-cation interactions [14], and ionic bonds [15], are weak, however, through the breaking of reasonable sacrificial bonds and sliding of some chain segments the interfacial load could be transferred and the strength could be enhanced.

Tang [16] constructed a network of sacrificial metal-ligand bonds in pyridyl styrene-butadiene rubber (VPR) and achieved 27.8 MPa tensile strength of the vulcanizate, which was higher than that of VPR reinforced by carbon black and silica. Huang [17] modified solution polymerized

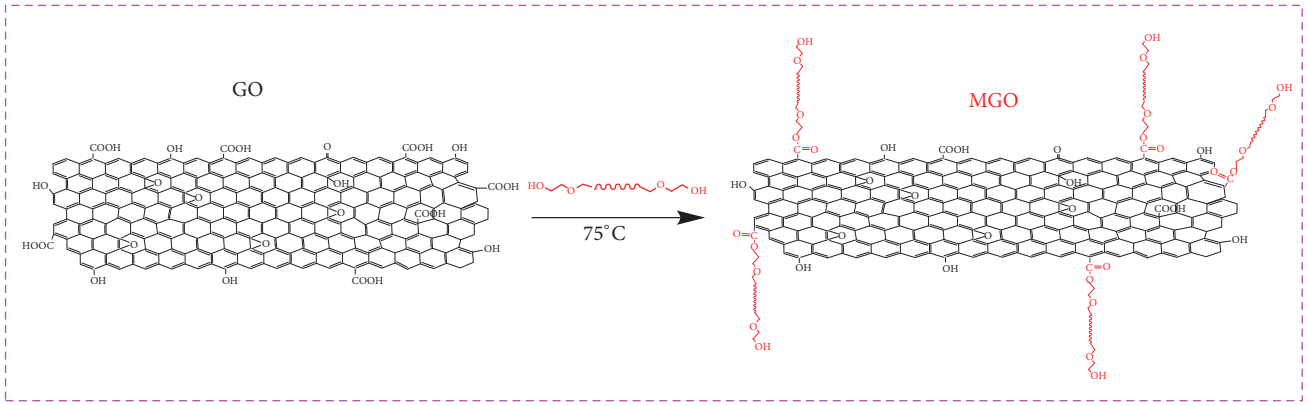

Figure 1: Preparation of polyethylene glycol graft modified graphene oxide.

styrene butadiene rubber (SSBR) with triazolidinedione by click chemistry and introduced the urezo groups to SSBR to provide hydrogen bonds; thereby, the sacrificial bonds were constructed in the system. The tensile strength of the modified SSBR had been significantly enhanced to 7.64 MPa, which was higher than that of the pure SSBR. Wu [18] used the maleic anhydride-modified polyisoprene rubber and aminomodified carbon nanodots to construct the network of sacrificial bonds and used unsaturated bonds to construct the chemically cross-linked network. The tensile strength approached 30.5 MPa when the dosage of carbon nanodots was only 3 phr, which was stronger than that of the polyisoprene rubber reinforced by 40 phr N330 carbon black. Mao [19] added a kind of VPR into GO/styrene butadiene rubber (SBR) system and constructed ionic bond interaction between pyridine group (positive) in the vinyl pyridine unit of VPR and oxygen-containing functional group (negative) on the surface of GO. Wu [20] characterized the interfacial interaction of VPR/GO composites by the dielectric relaxation spectra of the vulcanizates with different interactions (ionic bond, hydrogen bond). The results revealed that the velocity of segmental relaxation and interfacial relaxation of VPR/GO composite bonded by ionic bond was higher than that of composites bonded by hydrogen bond, indicating that the internal interaction of GO/VPR composites bonded by ionic bond was stronger. Li [21] found that the dissociation energy of hydrogen bond in polyurethane was about 16.7 kJ/mol. In general, the bonding energy of C-C covalent is over 300 kJ/mol. It means that the hydrogen bond is likely to be destroyed during the strain process and additional strain energy will be consumed, so the strength and toughness of material are guaranteed.

In the present paper, graphene oxide was grafted with polyethylene glycol 600 by means of the reaction between the carboxyl groups on the surface of graphene oxide and the hydroxyl groups at the end of polyethylene glycol and then added to PUR. The grafted graphene oxide reinforced the PUR significantly through hydrogen bonds on the filler-rubber interfaces. Additional strain energy was dissipated by destructing the hydrogen bond sacrificial unit during the strain process, thereby the strength and toughness were improved simultaneously.

2. Experiment

2.1. Materials. Polyurethane rubber (PUR, type of HA-5) was purchased from Shanxi Institute of Chemistry Industry, China. Graphene oxide (GO, lamellar size of 10-50 μm, layers of 6~10) was purchased from SuZhou Tanfeng Co., Ltd., China. Polyethylene glycol (PEG, AR, number-average molecular weight of 600), 4-dimethylaminopyridine (DMAP, AR), N, N'-dicyclohexylcarbodiimide (DCC, AR), and dicumyl peroxide (DCP, AR) were purchased from Sigma Aldrich Company, USA. All materials were used directly without further treatment.

2.2. Sample Preparation

2.2.1. Preparation of Grafted Graphene Oxide with Polyethylene Glycol. 600 mg GO and 350 ml toluene were added to a 500 ml single-neck flask at room temperature and dispersed by ultrasound for 30 minutes. Then 2.0 g PEG, 0.58 g DMAP, and 1.19 g DCC were added to the flask successively and dispersed by ultrasound for 30 minutes; thereafter, the content was stirred by magnetic force for 24 h at temperature 75°C. The reaction product was filtered by polytetrafluoroethylene filter paper with 0.2 μm aperture. Filter cake was washed with 50 ml of toluene and 700 ml of deionized water in turn and then was dried in vacuum oven at 60°C. The product was denoted as MGO. The preparation process was depictured in Figure 1.

2.2.2. Preparation of PUR/MGO. A mill (type of XK-150, Zhanjiang Machinery Factory, China) was used to mix the raw materials. The roller gap of mill was adjusted to about 0.1 mm, then PUR, GO (or MGO), and DCP were added in turn. After each addition, the PUR compounds were side-cut both sides in turn 5 times and then triangle-packed 5 times and thin-passing 5 times; finally, the rubber compounds were rolled into 2 mm sheet. After being parked for 24 h, the sheet was vulcanized on a press (type of KSH-R100, Dongguan Kesheng Industrial Co., Ltd., China) with 16 MPa for t_{90}+2 min at 175°C. The mass ratio of PUR: DCP was 100: 2. The amount of GO or MGO was variable. For example, if the amount of MGO was 0.5 phr, the sample was marked as PUR/MGO-0.5%.

2.3. Characterizations. The chemical structure of samples was characterized by an 8400S FTIR spectrometer (Shimadzu, Japan). The scanning range was 4000~400 cm^{-1}, the scanning time was 32, and the sample was produced by pressing potassium bromide troche.

Raman spectrum was determined by a LabRAM Aramis Raman microscope (HORIBA Jobin Yvon, France). The excitation source was He-Ne laser and the excitation wavelength was 532.0 nm.

The crystalline structure was analyzed using a D8 X-ray diffractometer (Bruker, Germany). The radiographic source was Cu-Kα, the accelerated voltage was 40 kV, the emission current was 40 mA, the scanning speed was 0.1 s/step, and the scanning range was 2θ=5~60°.

The thermal stability was characterized by a 209 F3 thermogravimetric analyzer (Netzsch, Germany). The examination range was 50~900°C for GO and MGO fillers, and the examination range was 50~800°C for PUR rubber. The heating rate was 30 K/min and the nitrogen stream was 20 ml/min.

The GO/PEG samples for FTIR, Raman spectra, X-ray diffraction test (XRD), and thermogravimetric test (TGA) were purified by reflux condensation with toluene for 2 h, then washed with 50 ml toluene and dried.

The dynamic mechanical properties were performed on a 214E dynamic mechanical analyzer (Netzsch, Germany) at stretching mode with a heating rate of 3 K/min from -80~60°C. The exciting frequency was 5 Hz and the amplitude was 60 μm.

The tensile properties were measured with a 2080 tensile testing machine (UC, Taiwan) according to the GB/T 528-2009, the thickness of specimens was 1.0 mm, the tensile speed of cyclic tension-recovery test was 50 mm/min, and the tensile speed of tensile strength test was 200 mm/min. The sample shape was a dumbbell-shaped strip.

The structure and morphology were recorded by a TM3030 scanning electron microscopy (Hitachi, Japan). The acceleration voltage was 15 kV and the samples were first sputtered with platinum film before measurement. The investigated surface was the tensile fracture surface.

3. Results and Discussion

3.1. Interface Structures of GO/PEG. The FTIR analyses were used to detect the molecular bonds' details of the GO, MGO, and PEG. MGO, GO, and PEG were analyzed with FTIR and the obtained spectra were shown in Figures 2(a) and 2(b). Compared with GO, the peak intensity of MGO at 3440 cm^{-1}, 2921 cm^{-1} and 1105 cm^{-1} was bigger. These three peaks correspond to the stretching vibration of the O-H bond, C-H bond, and C-O-C bond, respectively [22]. At 1257 cm^{-1} and 831 cm^{-1}, two new peaks appeared in MGO, which resulted from the stretching vibration of the C-O bond and the out-of-plane bending of O-H bond. All of these changes came from the grafting of PEG, which indicated that the PEG interacted with GO and successfully grafted on the surface of GO.

Raman spectroscopy can effectively characterize the crystal structure and charge transfer of GO. The Raman spectra of GO and MGO were shown in Figure 2(c). It can be seen from the figure that GO had two distinct characteristic peaks at 1580 cm^{-1} and 1342 cm^{-1}, which correspond to G-band and D-band of GO, respectively [23]. MGO also exhibited the G-band and D-band peaks, but the peak position of these two peaks shifted to 1589 cm^{-1} and 1334 cm^{-1}, respectively. This is because the interaction between PEG and GO leads to electron transfer [24]. In addition, the D-band is related to the vibration of sp^3 hybridized carbon and defects on the edges of GO formed during the oxidation. The G-band is caused by the vibration of sp^2 hybridized carbon in the graphite lattice. The intensity ratio of D-band and G-band (I_D/I_G) is commonly used to characterize the defects of graphene and monitor the functionalization of graphene [23]. The larger the I_D/I_G is, the more the C atomic lattice surface's defects exist. The smaller the I_D/I_G is, the less the C atomic lattice surface's defects exist. The I_D/I_G of GO was 0.23, while that of MGO was 0.83, which was significantly higher than that of GO. This is because PEG was randomly grafted on the GO surface by covalent bonds, resulting in the increase of the surface defects.

Figure 2(d) showed the TGA analysis curves of GO and MGO. The weight loss rate of GO at 200~900°C was only 2.01%, which was caused by the decomposition of oxygen-containing functional groups in the sample, while the weight loss rate of MGO at 50~200°C was 12.5%, which was caused by the loss of adsorbed water in the sample. The weight loss rate at 200~900°C was 38.9%, which was mainly due to the ablation of polyethylene glycol molecules grafted on the surface of the sample. Secondly, it also includes the decomposition of oxygen-containing functional groups on the surface of the sample. Therefore, the graft ratio of polyethylene glycol on the surface of GO was about 37%.

XRD can characterize the crystalline structure before and after GO modification. The XRD diagrams of GO and MGO were shown in Figure 2(e). A narrow and strong diffraction peak appeared at 26.4° in the diagram of GO, corresponding to the interlayer spacing of 0.337 nm. In addition, two weaker diffraction peaks appeared at 44.6° and 54.6°, which were the typical peaks of the multilayer grapheme [25]. Compared with GO, MGO also showed diffraction peaks at these three places, which indicated that the addition of PEG on the surface of GO did not affect the crystalline structure of GO, nor did it affect the interlayer spacing of GO sheets. What is more, MGO had a diffuse peak near 22°, which could ascribe to the addition of PEG. PEG was an amorphous substance, which was grafted to the surface of GO by the covalent bond and led to the appearance of diffuse peak [26].

3.2. Thermal Stability of PUR/MGO Composites. The thermogravimetric analyses of PUR, PUR/GO, and PUR/MGO vulcanizates were shown in Figure 3 and Table 1. Compared with the pure PUR vulcanizate, the initial decomposition temperature (T_i), maximum decomposition temperature (T_{max}), and termination decomposition temperature (T_t) of the vulcanizate added with 0.5% GO were increased by 1.9°C, 16.8°C, and 17.8°C, respectively. Meanwhile, the T_i, T_{max}, and T_t of the vulcanizate added with 0.5% MGO were increased by 2.7°C, 18.9°C, and 22.9°C, respectively. When the addition

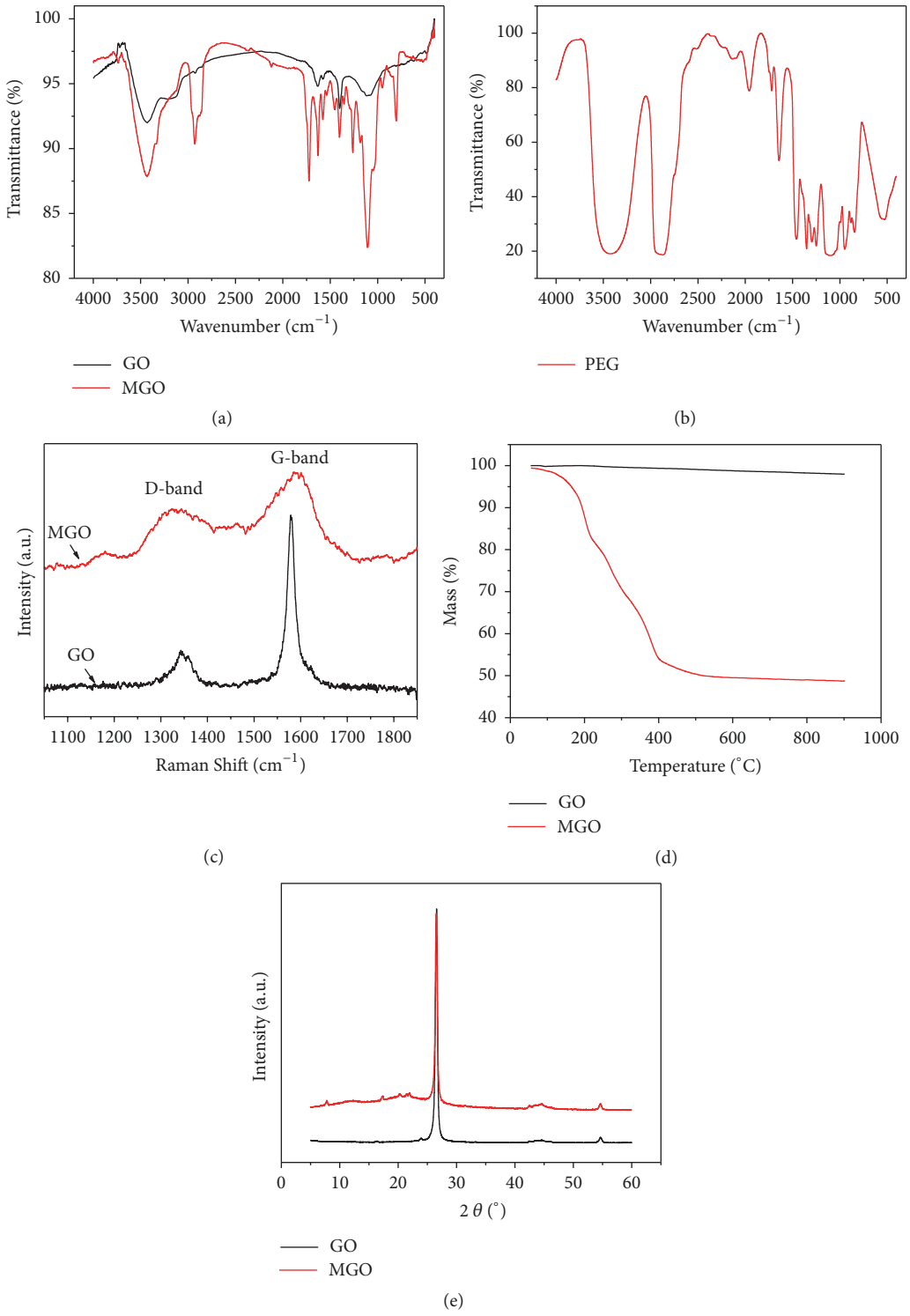

Figure 2: Structural characterizations of GO, MGO, and PEG. (a) FTIR characterization of GO and MGO; (b) FTIR characterization of PEG. (c) Raman spectra characterization of GO and MGO; (d) TGA characterization of GO and MGO; (e) XRD characterization of GO and MGO.

of GO or MGO were increased to 1%, the T_i, T_{max}, and T_t of the vulcanizates were increased again. This indicated that the addition of GO or MGO was helpful for improving the thermal stability of the vulcanizates. This improvement phenomenon was the same as the addition of a filler such as carbon black to the rubber matrix to improve the thermal stability of the vulcanizate [27]. In addition, the thermal stability of MGO-added compounds was better than that of GO-added compounds at the same dosage, because MGO was dispersed better in the rubber matrix after the graft

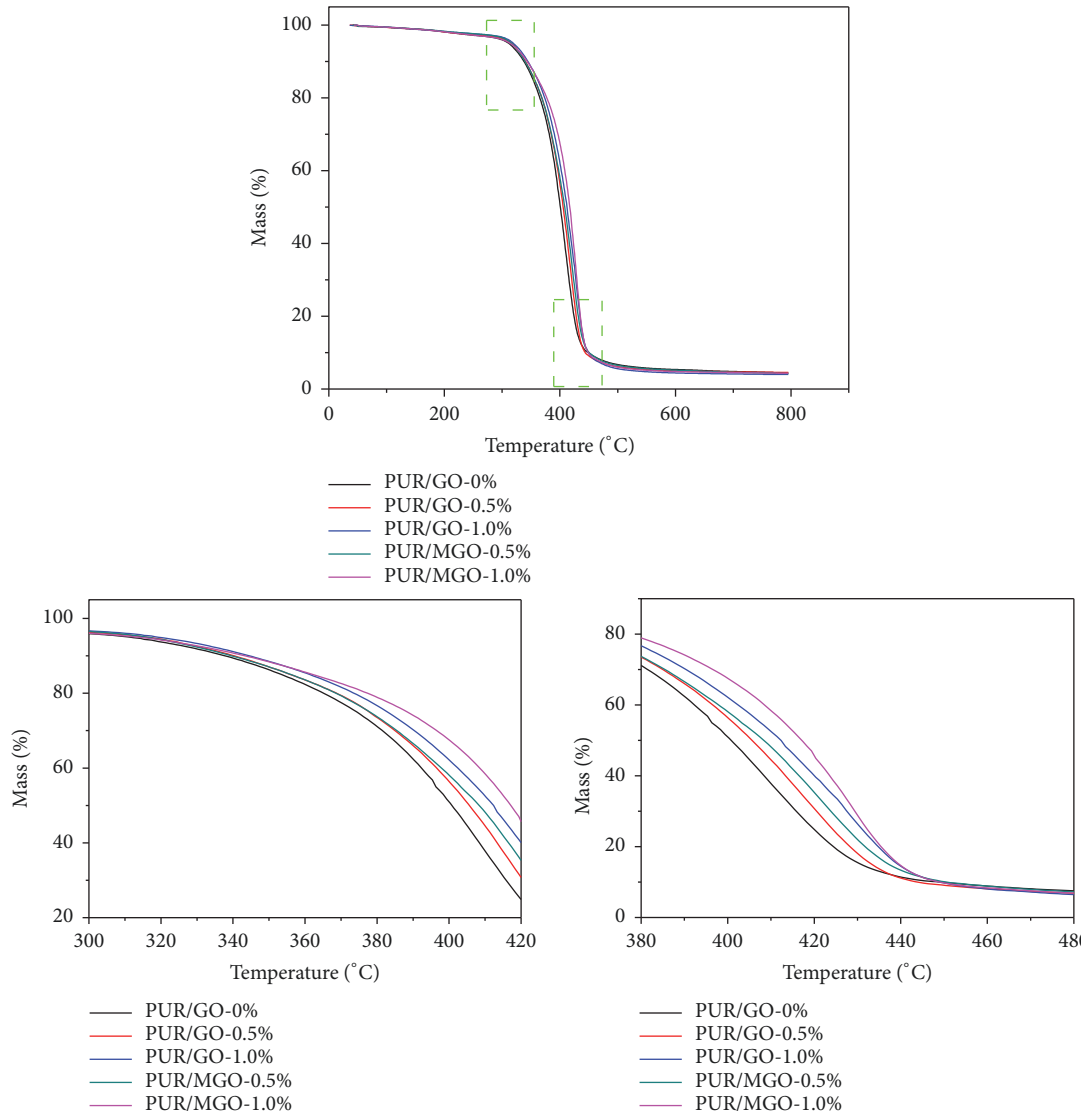

Figure 3: Thermogravimetric analyses of PUR, PUR/GO, and PUR/MGO composites.

Table 1: The key data of thermogravimetric analyses of PUR, PUR/GO, and PUR/MGO composites.

Sample	T_i(°C)	T_{max} (°C)	T_t(°C)
PUR/GO-0%	388.8	395.7	404.4
PUR/GO-0.5%	390.7	412.5	422.2
PUR/GO-1.0%	402.4	418.9	439.5
PUR/MGO-0.5%	391.5	414.6	427.3
PUR/MGO-1.0%	411.0	420.3	442.8

modification and formed stronger interaction with rubber molecular chains through molecular hydrogen bond [28]. What is more, after adding GO or MGO, the increasing range of the T_{max} and T_t of the vulcanizate was larger than that of the T_i. This is because GO or MGO is a lamellar structure, which would form a physical fire barrier layer in the rubber matrix after high-temperature combustion. The escape of decomposition products was slowed down and the further degradation was delayed because of the existence of this fire barrier [29].

3.3. Dynamic Mechanical Property of PUR/MGO Composites. The dynamic mechanical properties of PUR, PUR/GO, and PUR/MGO vulcanizates were shown in Figure 4. As can be seen from Figure 4(a), compared with the pure PUR vulcanizate, the initial storage modulus of the vulcanizate with GO or MGO was significantly increased. This is because the rigidity of the filler phase is much larger than that of the rubber phase, and the addition of a rigid filler phase to the flexible rubber phase produces a significant reinforcing effect

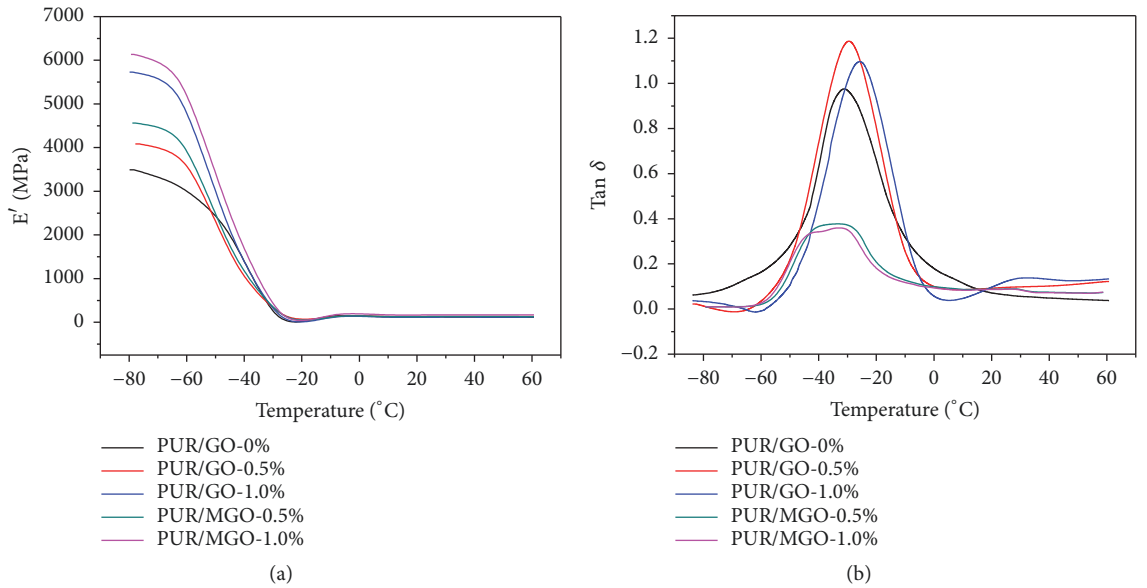

Figure 4: Dynamic mechanical properties of PUR, PUR/GO, and PUR/MGO composites.

[28]. This effect caused the initial storage modulus of vulcanizate to continue to increase when the filler phase content was increased from 0.5% to 1.0%. In addition, the storage modulus of PUR/MGO was larger than that of PUR/GO with the same filler content. This is due to the stronger interaction between MGO and PUR molecular chains [28].

The glass transition temperature (T_g) of elastomer can generally be obtained from the peak of the tan δ-temperature curve. It can be seen from Figure 4(b) that the T_g of the pure PUR vulcanizate was -30.8°C, and after adding 0.5% and 1.0% of GO, the T_g rose to -29.2°C and -25.5°C, respectively. It was shown that the addition of GO caused the T_g of vulcanizate to shift to higher temperature. This indicated that the low temperature resistance of vulcanizate decreased when GO was added. This is because the glass transition temperature is the reflection of the transition of the chain segments and the molecular chains motion form, and it is the lowest temperature for the molecular chain segments to have the motion ability in polymer. GO had a strong interaction with the rubber molecular chains, limiting the ability of the molecular chain to move, resulting in the increase of T_g. After the addition of MGO, the peak shape of the vulcanizate near the glass transition temperature had changed significantly, from the original high and sharp peak shape to a low and wide peak shape. In general, crystalline polymers exhibit a wide temperature range during the melting process. This temperature range is called the melting range, which is related to the melting of crystals with different crystallinity at different temperatures. Similarly, PUR/MGO composites also exhibit a wide temperature range during the glass transition process. This temperature range can be called the glass transition range of the polymer, which should be related to the multiple motion mechanisms of the molecular chains in PUR/MGO composites. During the dynamic strain process of PUR/MGO, besides the movement of microrubber molecular chain segments, the destruction and recombination of hydrogen bonds between rubber molecular chains and MGO surfaces were also included. This destruction and recombination of hydrogen bonds will dissipate a portion of the energy, resulting in the change of the tan δ peak shape. In addition, the glass transition range of PUR/MGO-0.5% was -30.4~-40.3°C, and the glass transition range of PUR/MGO-1.0% was -31.6~-42.7°C. Unlike the movement rule of the glass transition temperature of the vulcanizate with GO, the glass transition temperature of the vulcanizate was shifted to lower temperature, and the low temperature resistance of the material was increased after the addition of MGO. This is because the movement of hydrogen bonds is a kind of secondary transformation and can take place at lower temperature. This also explains why the glass transition temperature of PUR/MGO-1.0% was lower than that of PUR/MGO-0.5% because more hydrogen bonds were formed.

3.4. Tensile Properties of PUR/MGO Composites. The introduction of sacrificial hydrogen bonds in PUR matrix could improve the toughness of the material, which could be proved by the cyclic tension-recovery curve of vulcanizate. When the PUR, PUR/MGO-0.5%, and PUR/MGO-1.0% samples were respectively stretched to a preset strain of 100%, the values of the hysteresis loops were 33.03, 38.66, and 42.99, respectively (Figure 5(a)). It can be seen that the obvious hysteresis loss occurred after adding MGO, and the value of hysteresis loss was increased with the increase of MGO content. This is because the hydrogen bonds will be produced when MGO was added to the PUR matrix, and the hydrogen bonds in the PUR matrix were destroyed during the stretching process and a large amount of energy was dissipated, which led to the increase of hysteresis loss.

However, hydrogen bond is reversible, and it can be regenerated during the storage or heat treatment of material

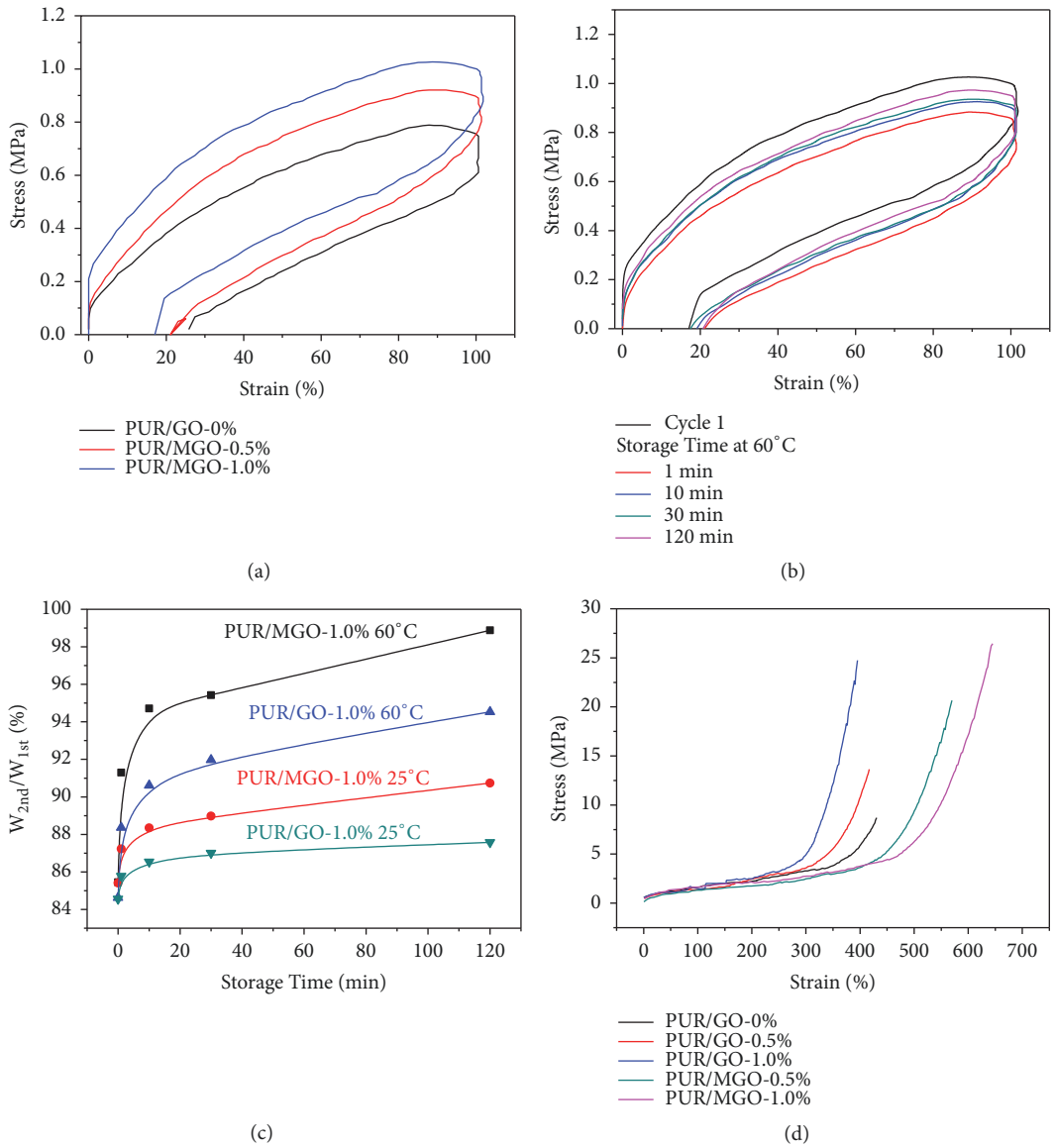

Figure 5: Tensile properties of PUR, PUR/GO, and PUR/MGO composites.

to achieve dynamic reversibility. In general, the recovery of hydrogen bond is dependent on the time and temperature. Taking PUR/MGO-1.0% as an example, the cyclic tension-recovery curves of PUR/MGO-1.0% vulcanizate with different recovery time at 60°C were discussed (Figure 5(b)). It can be found that hydrogen bonds can spontaneously recover during high-temperature storage, which leaded to a gradual increase of hysteresis loss.

The hysteresis loss recovery of PUR/GO-1.0% and PUR/MGO-1.0% under different conditions was quantitatively compared in Figure 5(c). W_{1st} was the initial tension-recovery hysteresis loss of the sample, and the W_{2nd} was the tension-recovery hysteresis loss of the samples after it had recovered for a certain time at a certain temperature. Firstly, with the prolongation of storage time, the hysteresis loss of PUR/GO-1.0% gradually recovered, which was related to the recrimping, reentanglement of microrubber molecular chains and the interaction recovery of filler-rubber molecular chains. Under the same storage time, the recovery rate of hysteresis loss of PUR/MGO-1.0% was higher than that of PUR/GO-1.0%. This was because, for PUR/MGO-1.0% sample, besides the recrimping, reentanglement of microrubber molecular chains and the interaction recovery of filler-rubber molecular chains, the regeneration of hydrogen bonds also led to an increase of recovery rate. Secondly, the recovery rate was increased with the increase of the storage temperature. The recovery rate of PUR/GO-1.0% was 87.58% after storage at 25°C for 120 min, and the recovery rate was increased to 94.53% after storage at 60°C for 120 min. The recovery rate of PUR/MGO-1.0% was 90.74% after storage at 25°C for 120 min, and the recovery rate was increased to 98.88% after storage at 60°C for 120 min. In addition, under the same storage temperature, the recovery rate of the samples with MGO was higher than that of samples with GO. This is not

only related to the recrimping, reentanglement of microrubber molecular chains and the recovery of the interaction between fillers and rubber molecular chains, but also to the faster spontaneous recovery of dissociated hydrogen bonds at higher temperature.

The stress-strain curves of PUR, PUR/GO, and PUR/MGO vulcanizates were shown in Figure 5(d). The tensile strength and elongation at break of pure PUR vulcanizate were 8.65 MPa and 431%. After adding 0.5% GO, the tensile strength of the vulcanizate was increased to 13.64 MPa and the increase rate was 57.7%, but the elongation at break was decreased to 417%, and the decrease rate was 3.2%. When the amount of GO was increased by 1%, the tensile strength of the vulcanizate continued to rise to 24.75 MPa, the rate of increase was 186.1%, the elongation at break was decreased to 395%, and the decrease rate was 8.4%. It was shown that the tensile strength of vulcanizate was improved with the increase of GO content, but the elongation at break was decreased. That is, the strength of vulcanizate was increased and the toughness was decreased when GO was added. However, after adding 0.5% MGO, the tensile strength of the vulcanizate was increased to 20.65 MPa, the increase rate was 138.7%, the elongation at break was increased to 570% at the same time, and the increase rate was 32.2%. When the amount of MGO was increased by 1%, the tensile strength of the vulcanizate continued to rise to 26.44 MPa, the increase rate was 205.7%, the elongation at break continued to rise to 645%, and the increase rate was 49.6%. It can be seen that the addition of MGO is helpful for improving the strength and toughness of vulcanizate simultaneously.

3.5. SEM Analyses of PUR/MGO Composites. SEM can be used to analyze the dispersion of fillers in rubber matrix and the interactions between the filler and rubber matrix. The tensile fracture surface of PUR, PUR/GO, and PUR/MGO vulcanizates were shown in Figure 6. As can be seen from the figures, the pure PUR vulcanizate had a relatively simple cross-section structure and the fracture surfaces were smooth in each fault (Figure 6(a)). After adding 0.5% GO or MGO, the fracture surfaces of the vulcanizates were rough, and the height difference between the cross-section layers was reduced. Moreover, the cross-section layers were parallel-peeled (Figures 6(b) and 6(c)). This indicated that there should be a kind of force perpendicular to the direction of tensile stress during the fracture of vulcanizate. This force should originate from the sheet exfoliation of graphene oxide lamellae from rubber matrix by the tensile force (as shown in the red circle in Figure 6(c)). When the amount of GO or MGO was added to 1%, the sense of layering of the cross-section tented to be more obvious (Figures 6(d) and 6(e)), because the filler and rubber matrix produced more sheet exfoliation. Comparing PUR/GO and PUR/MGO with 1% fillers (comparing Figure 6(d) with Figure 6(e)), it can be found that the sense of layering of the cross-section of the PUR/MGO was stronger than that of PUR/GO and the section of the PUR/MGO vulcanizate was rich and scattered. The reason was that the compatibility between the rubber matrix and GO was improved when GO was modified with PEG, and the dispersibility of MGO in the rubber matrix was also improved. Therefore, the interaction points between the fillers and the rubber molecular chains were increased, and the interaction force was improved.

3.6. Mechanism on Strengthening and Toughening PUR/MGO Composites. The strengthening and toughening mechanism of PUR/MGO composites was shown in Figure 7. In PUR/MGO system, continuous hydrogen bonds were formed between the PUR molecular chains and the PEG molecular chains which was grafted on the surface of GO by covalent bonds ($\lambda=\lambda_0$). During the stretching process, the PUR molecular chains were firstly oriented along the stress direction ($\lambda=\lambda_1$). If the strain was increased continuously ($\lambda=\lambda_2$, λ_3), the hydrogen bonds between PUR and PEG would be gradually dissociated, and the hydrogen bond interactions would be destroyed gradually with the increase of strain. A large amount of strain energy was consumed and the hidden length hid between the PUR molecular chains and the PEG molecular chains was released during the strain process. Thus, the tensile strength and toughness of the rubber material could be improved simultaneously. In PUR/MGO system, the PUR molecular chains had been cross-linked because of the presence of DCP vulcanizing agent. If the vulcanizate was not broken at the macroscopic level during the strain process, it will show macrorecovery under the action of the DCP permanent cross-linking bonds when the stress was removed. Meanwhile, the PEG molecular chains and the PUR molecular chains were close to each other at the microscopic level, which made it possible to regenerate hydrogen bonds between the PEG molecular chains and the PUR molecular chains during the storage or heat treatment process, and thereby the reversible recovery of hydrogen bonds was realized ($\lambda=\lambda'_0$).

4. Conclusions

The hydrogen bond sacrificial units were introduced into the PUR-MGO system by grafting PEG onto the surface of GO. The FTIR analysis showed the PEG was successfully grafted onto the surface of GO. The TGA analysis indicated the grafting rate was about 37%. The XRD analysis determined the addition of PEG did not affect the crystalline structure of GO. The hydrogen bond sacrificial units of PUR/MGO composites were destroyed and the hidden length was released during the stretching process, thereby the tensile strength and elongation at break were improved simultaneously. Compared with pure PUR vulcanizate, the tensile strength and elongation at break of PUR/MGO-1.0% were increased by 205.7% and 49.6%, respectively, while the tensile strength of PUR/GO-1.0% was increased by 186.1%, but the elongation at break was decreased by 8.4%. In addition, the addition of GO or MGO can improve the thermal stability of PUR, and the improvement of MGO was better. The T_g of PUR/GO-1.0% was increased by 5.3°C. However, the T_g of PUR/MGO-1.0% was shifted to lower temperature. What is interesting was that a kind of glass transition range appeared due to the introducing of hydrogen bonds. What is more, increasing

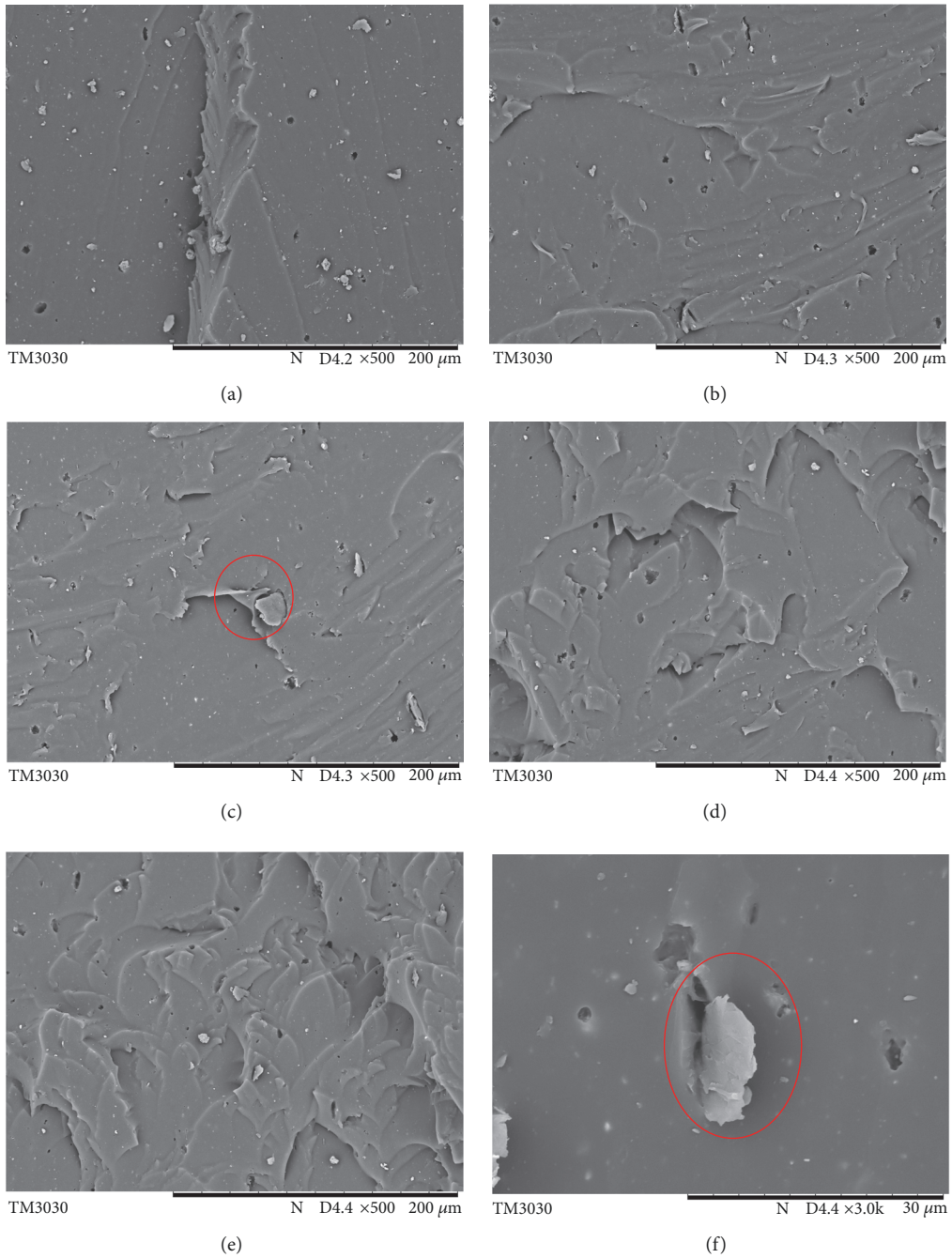

Figure 6: SEM analyses of PUR, PUR/GO, and PUR/MGO composites. (a) PUR/GO-0%; (b) PUR/GO-0.5%; (c) PUR/MGO-0.5%; (d) PUR/GO-1.0%; (e) PUR/MGO-1.0%; (f) PUR/MGO-1.0%.

the heat treatment temperature and prolonging the heat treatment time were helpful for the reversible recovery of hydrogen bonds.

Data Availability

The figure and table data used to support the findings of this study are included within the article.

Conflicts of Interest

The authors declare that they have no conflicts of interest.

Authors' Contributions

Li Wang and Wen Fu contributed equally to this paper.

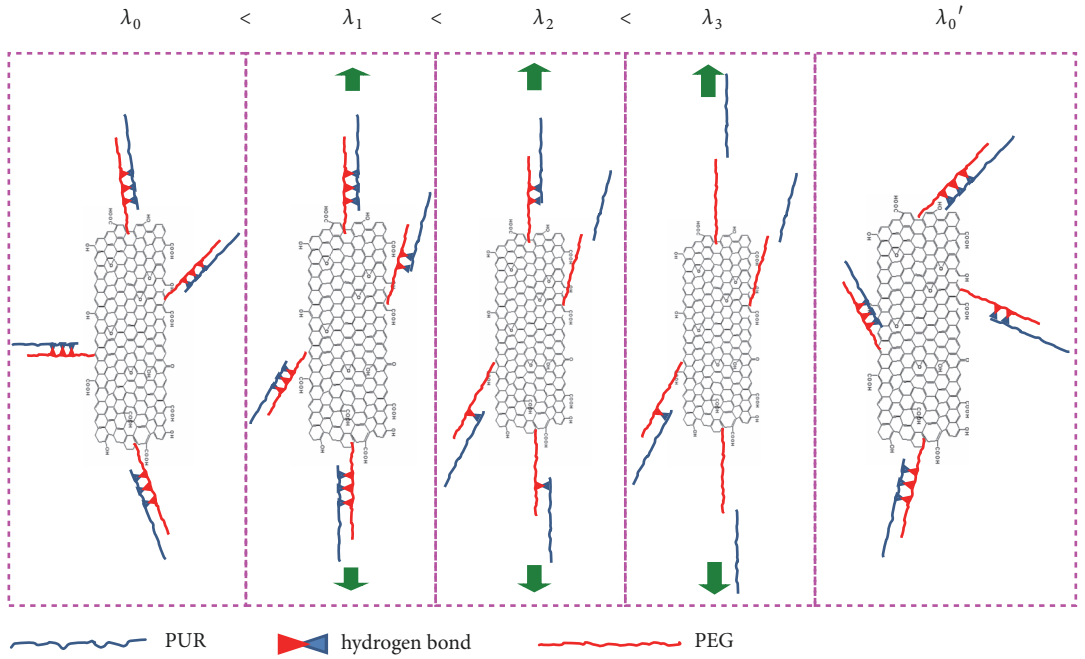

Figure 7: Strengthening and toughening mechanism of PUR/MGO composites.

Acknowledgments

This research was supported by Natural Science Foundation of Guangdong Province (2017A030310663, 2018A030307018, and 2018A0303070003), Distinguished Young Talents in Higher Education of Guangdong (2016KQNCX107), Guangdong Research Center for Unconventional Energy Engineering Technology (GF2018A005), and Maoming Science and Technology Project (Maokezi 2019 (33)).

References

[1] C. Lee, X. Wei, J. W. Kysar, and J. Hone, "Measurement of the elastic properties and intrinsic strength of monolayer graphene," *Science*, vol. 321, no. 5887, pp. 385–388, 2008.

[2] V. D. Punetha, S. Rana, H. J. Yoo et al., "Functionalization of carbon nanomaterials for advanced polymer nanocomposites: A comparison study between CNT and graphene," *Progress in Polymer Science*, vol. 67, pp. 1–47, 2017.

[3] S. He, N. D. Petkovich, K. Liu, Y. Qian, C. W. Macosko, and A. Stein, "Unsaturated polyester resin toughening with very low loadings of GO derivatives," *Polymer Journal*, vol. 110, pp. 149–157, 2017.

[4] M. Suominen, P. Damlin, S. Granroth, and C. Kvarnström, "Improved long term cycling of polyazulene/reduced graphene oxide composites fabricated in a choline based ionic liquid," *Carbon*, vol. 128, pp. 205–214, 2018.

[5] J. Wang, H. Jia, Y. Tang et al., "Enhancements of the mechanical properties and thermal conductivity of carboxylated acrylonitrile butadiene rubber with the addition of graphene oxide," *Journal of Materials Science*, vol. 48, no. 4, pp. 1571–1577, 2013.

[6] C. Wu, X. Huang, G. Wang et al., "Hyperbranched-polymer functionalization of graphene sheets for enhanced mechanical and dielectric properties of polyurethane composites," *Journal of Materials Chemistry*, vol. 22, no. 14, pp. 7010–7019, 2012.

[7] X. She, C. He, Z. Peng, and L. Kong, "Molecular-level dispersion of graphene into epoxidized natural rubber: morphology, interfacial interaction and mechanical reinforcement," *Polymer Journal*, vol. 55, no. 26, pp. 6803–6810, 2014.

[8] S. Keten, Z. Xu, B. Ihle, and M. J. Buehler, "Nanoconfinement controls stiness, strength and mechanical toughness of beta-sheet crystals in silk," *Nature Materials*, vol. 9, no. 4, pp. 359–367, 2010.

[9] M. E. Launey, M. J. Buehler, and R. O. Ritchie, "On the mechanistic origins of toughness in bone," *Annual Review of Materials Research*, vol. 40, no. 1, pp. 25–53, 2010.

[10] A. Gautieri, M. J. Buehler, and A. Redaelli, "Deformation rate controls elasticity and unfolding pathway of single tropocollagen molecules," *Journal of the Mechanical Behavior of Biomedical Materials*, vol. 2, no. 2, pp. 130–137, 2009.

[11] M. Hayashi, S. Matsushima, A. Noro, and Y. Matsushita, "Mechanical property enhancement of ABA block copolymer-based elastomers by incorporating transient cross-links into soft middle block," *Macromolecules*, vol. 48, no. 2, pp. 421–431, 2015.

[12] B. J. Gold, C. H. Hövelmann, C. Weiss et al., "Sacrificial bonds enhance toughness of dual polybutadiene networks," *Polymer Journal*, vol. 87, pp. 123–128, 2016.

[13] M. C.R., L. M., J. Y.L., S. L., and R. K. R.T., "Adsorption behaviour of reduced graphene oxide towards cationic and anionic dyes: Co-action of electrostatic and $\pi - \pi$ interactions," *Materials Chemistry and Physics*, vol. 194, pp. 243–252, 2017.

[14] J. Yuan, H. Zhang, G. Hong et al., "Using metal–ligand interactions to access biomimetic supramolecular polymers with adaptive and superb mechanical properties," *Journal of Materials Chemistry B*, vol. 37, no. 1, pp. 4809–4818, 2013.

[15] L. Zhang, L. R. Kucera, S. Ummadisetty et al., "Supramolecular multiblock polystyrene–polyisobutylene copolymers via ionic interactions," *Macromolecules*, vol. 47, no. 13, pp. 4387–4396, 2014.

[16] Z. Tang, J. Huang, B. Guo, L. Zhang, and F. Liu, "Bioinspired engineering of sacrificial metal–ligand bonds into elastomers with supramechanical performance and adaptive recovery," *Macromolecules*, vol. 49, no. 5, pp. 1781–1789, 2016.

[17] J. Huang, L. Zhang, Z. Tang et al., "Bioinspired design of a robust elastomer with adaptive recovery via triazolinedione click chemistry," *Macromolecular Rapid Communications*, vol. 38, no. 7, pp. 1600678–1600684, 2017.

[18] S. Wu, M. Qiu, Z. Tang, J. Liu, and B. Guo, "Carbon nanodots as high-functionality cross-linkers for bioinspired engineering of multiple sacrificial units toward strong yet tough elastomers," *Macromolecules*, vol. 50, no. 8, pp. 3244–3253, 2017.

[19] Y. Y. Mao, S. P. Wen, Y. L. Chen et al., "High performance graphene oxide based rubber composites," *Scientific Reports*, vol. 3, no. 3, pp. 2508–2514, 2013.

[20] W. Wu, C. Wan, S. Wang, and Y. Zhang, "Physical properties and crystallization behavior of ethylene-vinyl acetate rubber/polyamide/graphene oxide thermoplastic elastomer nanocomposites," *RSC Advances*, vol. 3, no. 48, pp. 26166–26176, 2013.

[21] S. M. Liff, N. Kumar, and G. H. McKinley, "High-performance elastomeric nanocomposites via solvent-exchange processing," *Nature Materials*, vol. 6, no. 1, pp. 76–83, 2007.

[22] D. Luo, F. Wang, B. V. Vu et al., "Synthesis of graphene-based amphiphilic Janus nanosheets via manipulation of hydrogen bonding," *Carbon*, vol. 126, pp. 105–110, 2018.

[23] X. Liu, W. Kuang, and B. Guo, "Preparation of rubber/graphene oxide composites with in-situ interfacial design," *Polymer Journal*, vol. 56, pp. 553–562, 2015.

[24] H. Sun, G.-L. Xu, Y.-F. Xu et al., "A composite material of uniformly dispersed sulfur on reduced graphene oxide: aqueous one-pot synthesis, characterization and excellent performance as the cathode in rechargeable lithium-sulfur batteries," *Nano Research*, vol. 5, no. 10, pp. 726–738, 2012.

[25] J. Zhang, Y. Xu, L. Cui et al., "Mechanical properties of graphene films enchanced by homo-telechelic functionalized polymer fillers via π–π stacking interactions," *Composites Part A: Applied Science and Manufacturing*, vol. 71, pp. 1–8, 2015.

[26] L. Zhang, R. Jamal, Q. Zhao, M. Wang, and T. Abdiryim, "Preparation of PEDOT/GO, PEDOT/MnO_2, and PEDOT/GO/MnO_2 nanocomposites and their application in catalytic degradation of methylene blue," *Nanoscale Research Letters*, vol. 10, pp. 148–156, 2015.

[27] Z. X. Ooi, H. Ismail, and A. A. Bakar, "A comparative study of aging characteristics and thermal stability of oil palm ash, silica, and carbon black filled natural rubber vulcanizates," *Journal of Applied Polymer Science*, vol. 130, no. 6, pp. 4474–4481, 2013.

[28] H. Lian, S. Li, K. Liu, L. Xu, K. Wang, and W. Guo, "Study on modified graphene/butyl rubber nanocomposites. I. Preparation and characterization," *Polymer Engineering & Science*, vol. 51, no. 11, pp. 2254–2260, 2011.

[29] J. R. Potts, D. R. Dreyer, C. W. Bielawski, and R. S. Ruoff, "Graphene-based polymer nanocomposites," *Polymer Journal*, vol. 52, no. 1, pp. 5–25, 2011.

Hindawi
Advances in Polymer Technology
Volume 2019, Article ID 4523696, 11 pages
https://doi.org/10.1155/2019/4523696

Research Article

Mechanical Properties and Mullins Effect in Natural Rubber Reinforced by Grafted Carbon Black

Wen Fu,[1] **Li Wang**,[2] **Jianning Huang**,[1] **Cuiwen Liu**,[1] **Wenlong Peng**,[1] **Haotuo Xiao**,[1] **and Shenglin Li**[1]

[1]*College of Material Science, Guangdong University of Petrochemical Technology, Maoming, Guangdong 525000, China*
[2]*College of Chemical Engineering, Guangdong University of Petrochemical Technology, Maoming, Guangdong 525000, China*

Correspondence should be addressed to Li Wang; wanglihaha@126.com

Received 18 June 2019; Accepted 11 July 2019; Published 1 August 2019

Guest Editor: Zhiwei Qiao

The obvious polarity difference between the carbon black (CB) and the natural rubber (NR) causes the CB hard to be dispersed in the NR matrix when the addition amount is large. In this paper, polyethylene glycol (PEG) was grafted onto the surface of CB by the liquid phase. The grafted carbon black (GCB) was prepared and applied to reinforce NR. The main physical and mechanical properties of NR were improved because of the better compatibility between GCB and NR. The Mullins effect of the vulcanizate was calculated by the cyclic stress-strain experiment. The results showed that the Mullins effect both existed in the virgin NR system and filled NR system. The degree of Mullins effect was increased with the increase of the filler addition, but that was different for CB and GCB. When the filler addition was below 20 phr, the Mullins effect of NR/GCB was stronger than that of NR/CB. However, when the filler addition was over 30 phr, the Mullins effect of NR/CB was stronger than that of NR/GCB. The Mullins effect was affected by the heat treatment temperature and time. The mechanisms of the Mullins effect were analyzed.

1. Introduction

Because the rubber materials have high elasticity, damping, and other excellent properties, they have been widely used in tires, electronics, military, aerospace, and other fields [1–3]. In general, the physical and mechanical properties of the pure rubber are not very good, so the rubber materials need to be reinforced in order to improve their comprehensive performance. Carbon black is the main reinforcement agent in the rubber industry [2–4]. Since CB is a polar material and NR is a nonpolar material, the polarity difference between CB and NR is obvious, so the dispersion of CB in the NR matrix is difficult when the amount of CB is large, thereby causing the decrease of the physical and mechanical properties of NR. Grafting some polymer chains on the surface of CB to reduce the polarity difference between CB and the matrix is a good strategy, thereby enhancing the reinforcing effect of CB.

Chen [5] used the radiation grafting method to graft the polyethylene (PE) on the surface of carbon black. The grafting ratio of PE onto the carbon black surface proceeded and the percentage of grafting exceeded 90% when the irradiation dose reached 200 kGy. Tsubokawa [6] investigated the surface grafting of hyperbranched poly(amidoamine) onto the surface by using dendrimer synthesis methodology. The percentage of poly(amidoamine) grafting reached 96.2% after 10th generation. Richner [7] grafted the isocyanate prepolymers on the surface of CB. This crosslinked carbon black was designed as a new active material for electrochemical electrodes, and the active material for electric double-layer capacitor electrodes was produced which had a specific capacitance of up to 200 F/g. Yang [8] first synthesized the polystyrene, poly(styrene-co-maleic anhydride), poly[styrene-co-(4-vinylpyridine)], and poly(4-vinylpyridine). Then, the resultant polymers were grafted onto the surface of carbon black through a radical trapping reaction. It was found that the carbon black grafted with polystyrene and poly(styrene-co-maleic anhydride) could be dispersed in tetrahydrofuran, chloroform, dichloromethane, N, N-dimethylformamide, etc., and the carbon black

grafted with poly(4-vinylpyridine) and poly[styrene-co-(4-vinylpyridine)] could be well dispersed in ethanol.

The required stress at the same certain strain was decreased after cyclic tension treatment for several times in the vulcanized rubber composites, which was called the strain softening effect or Mullins effect [9]. This effect was discovered by Bouasse and Carriere [10]. More following works by Mullins pointed out that the Mullins effect not only existed in the filled rubber system, but also in the unfilled rubber system. However, the Mullins effect of the unfilled rubber system was weaker than that of the filled rubber system [11, 12]. Other similar researches about the Mullins effect had been conducted, for example, the rubber matrix (nitrile rubber [13], ethylene propylene diene rubber [14], natural rubber [15], and styrene butadiene rubber [16]) with carbon black [17], silica [18], and other fillers [19].

Some explanatory models were proposed to explain the Mullins effect. Bueche [20] pointed out that it was a proportional relationship between the space change of microparticles and the macroscopic deformation. With the increase of the macroscopic deformation, the rubber molecular chains among filler particles achieved their ultimate elongation, and some molecular chains would be broken away from the filler surfaces, leading to a decrease of the interaction force between the molecular chains and fillers, finally causing the Mullins effect. Houwink [21] put forward that the Mullins effect resulted from the slipping of the molecular chains adsorbed on the filler surface during the stretching process. Mullins [11] insisted that the filled vulcanized rubber was a hybrid system consisted of the high filler content region (hard phase) and low filler content region (soft phase). During the deformation process, the hard phase would be transferred to the soft phase, which led to the Mullins effect. This view was further perfected by Johnson [22]. He pointed out that the short molecular chains in the vulcanized rubber system would be tangled to form the molecular chain clusters, followed by the formation of hard phase in the internal. Some molecular chains of the hard phase were pulled out and transferred into the soft phase during the deformation process. Kraus [23] thought that the Mullins effect was the combination of several effects, including the destruction of the filler aggregate network and the destruction of the filler-rubber molecular interaction. Hamed [24] noted that the rubber molecular chains could adsorb on the filler surface to form a rubber shell layer. Under the external force, the rubber molecular chains adsorbed on the surface of fillers would be desorbed, thus reducing the thickness of the rubber shell and weakening the interaction between the rubber and carbon black. Roozbeh [12] mentioned that the filled rubber system contained two kinds of cross-linking networks, the molecular chains cross-linking network of the rubber matrix, and the interaction network of the filler-filler and filler-matrix. The Mullins effect was the result of the interaction between these two kinds of cross-linking networks. Until now, these models are still controversial, none of which can provide a reasonable and complete explanation for the Mullins effect. Table 1 showed the related diagrams of mechanism models of the Mullins effect.

In this work, in order to reduce the polarity difference between CB and NR and improve the dispersion of CB in the NR matrix, CB was graft modified with PEG and applied to reinforce NR. The comprehensive performance of NR has been increased with the addition of GCB. More importantly, the Mullins effect mechanisms were deduced by comparing the effects of GCB and CB on the Mullins effect of NR under different conditions.

2. Experiments

2.1. Materials. Natural rubber (NR, type of 3L) was purchased from Guangzhou Beishite Company, China. Carbon black (CB, type of N330, the average diameter size of 25~30 nm, the specific surface area of 103 m^2/g) was obtained from Cabot Corporation, USA. Concentrated nitric acid, toluene, thionyl chloride, dibutyl dilaurate, zinc oxide (ZnO), stearic acid (SA), and polyethylene glycol (PEG, number-average molecular weight of 400) were analytically pure and purchased from Sigma Aldrich Company, USA. Poly(1,2-dihydro-2,2,4-trimethyl-quinoline (antioxidant RD), 2,2′-dibenzothiazole disulfide (accelerator DM) and sulfur (S) were purchased directly from the market and used as received.

2.2. Sample Preparation

2.2.1. The Preparation of Grafted Carbon Black. 50 g of CB and 350 ml of concentrated nitric acid were added to a 1000 ml three-neck flask, the samples were reacted at 60°C for 2 h using the mechanical stirring, and then the reaction product was filtered, washed with deionized water, dried at 95°C to obtain the intermediate A. 50 g of the intermediate A, 12.5 g of thionyl chloride, and 350 ml of toluene were placed in a 1000 ml three-neck flask, and the samples were reacted at 0°C for 30 min and then at 120°C for 30 min using the mechanical stirring. The reaction product was rotary evaporated at 80°C to remove the unreacted thionyl chloride; the intermediate B was prepared. Subsequently, 50 g of the intermediate B, 25 g of PEG, 0.1 ml of dibutyl dilaurate, and 350 ml of toluene were added to a 1000 ml three-neck flask; the samples were reacted 0°C for 30 min and then at 120°C for 1 h using the mechanical stirring. The reaction product was filtered, washed with deionized water, dried at 95°C to obtain the grafted carbon black, denoted as GCB.

2.2.2. The Preparation of NR/CB and NR/GCB Vulcanizates. The roller gap of two-roll mill was adjusted to about 2 mm, NR was added and plasticated for 8 minutes, and then CB (or GCB), ZnO, SA, RD, DM, and S were added to the two-roll mill in turn, followed by 5 times side cuts on the left and right, and then a triangle package was implemented 7 times and thin-passing for 8 times. Subsequently, the compounds were stored for 24 h and were cured by a press vulcanizer at 150°C for (t_{90}+2) min. The mass ratio of NR, ZnO, SA, RD, DM, and S was 100: 5: 2: 1: 1: 2. The filler contents were varied from 0 to 60 phr.

Table 1: Schematic diagrams of Mullins effect mechanisms.

Models	Schematic diagrams
Detachment of the molecular chains [20]	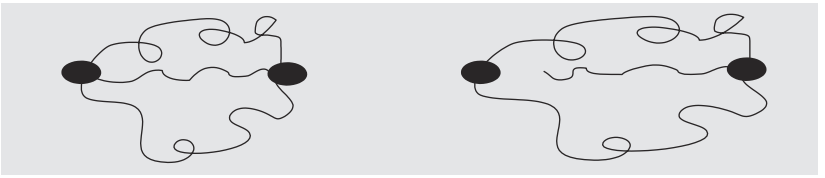
Slippage of the molecular chains [21]	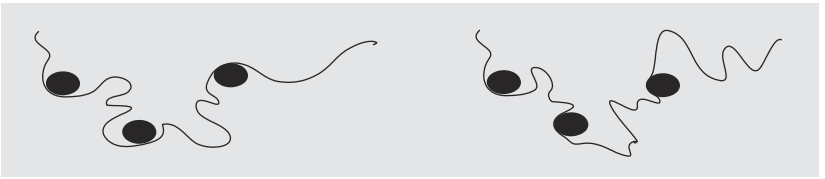
Disentanglement of the rubber molecular chains [11, 22]	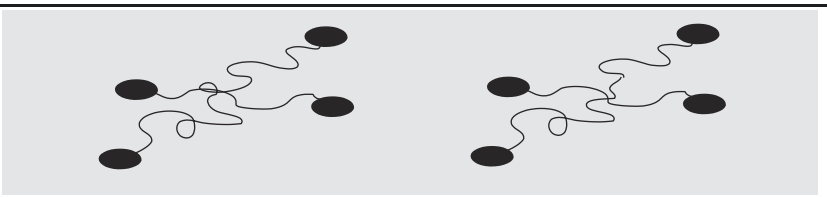
Destruction of the filler aggregates [23]	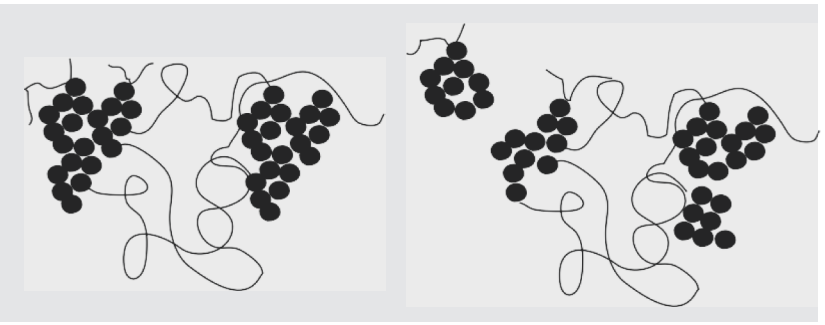
Rubber shell model [24]	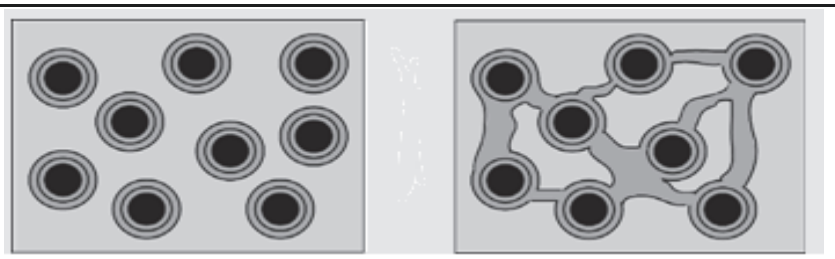

2.3. Characterization

2.3.1. Thermogravimetric Analysis. The thermogravimetric analyzer (TGA, 209 F3, Netzsch, Germany) was used to test the graft ratio of PEG on CB. The temperature range was 30~850°C, the heating rate was 50 K/min, and the test atmosphere was nitrogen. In order to remove the PEG adsorbed on the surface of CB through physical adsorption, GCB was purified by reflux condensation for 0.5 h with toluene and then dried.

2.3.2. Physical and Mechanical Properties Test. The electronic tensile testing machine (GT-TCS-2000, Gaotie, China) was used to test the tensile and tear properties. The tensile strength was characterized according to GB/T 528-2009, the tensile speed was 200 mm/min, the thickness was 2.0 mm, and the sample shape was dumbbell-shaped. The tear strength was tested according to GB/T 529-2008; the sample shape was right angle. The Shore A hardness was determined according to GB/T 531-1999. The wear resistance was measured according to GB/T 9867-2008. The apparent crosslink density was tested by the swelling method. About 1 g of the vulcanizate was weighed and cut into small strips about 2 mm wide and 1 mm thick and the treated samples were stored in a container with toluene for 7 d at room temperature. After completing the swelling process, these strips were taken out, and then the toluene adsorbed on the surface of these strips was removed using the filter paper; subsequently, these strips were weighed. The crosslink density was calculated according to the Nory-Rehner formula [25] as follows:

$$\nu_r = \frac{1}{v}\left[\frac{\ln\left(1-\nu_2\right)+\nu_2+\chi{\nu_2}^2}{{\nu_2}^{1/3}-\nu_2/2}\right] \quad (1)$$

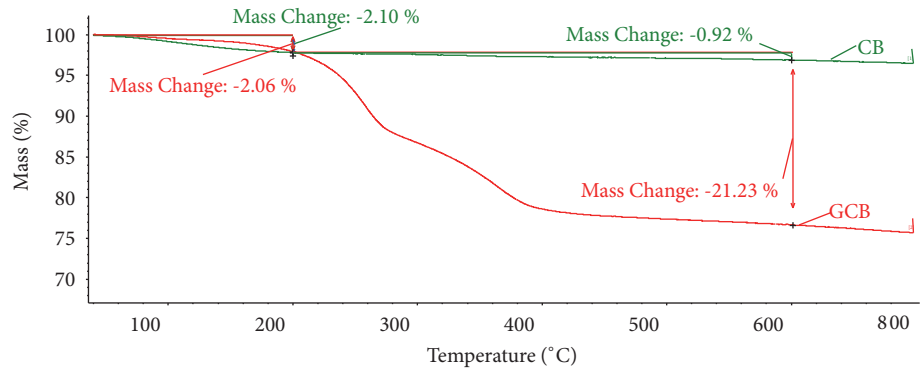

Figure 1: TGA analysis of carbon black before and after modification.

v_r is the apparent crosslink density of the vulcanizate, v_2 is the volume fraction of the rubber phase in the vulcanizate, χ is the interaction parameters between the rubber and solvent, v is the molar volume of the solvent.

where v_2 was calculated according to the formula

$$v_2 = \frac{m_3/\rho}{m_3/\rho + (m_2 - m_1)/\rho_s} \quad (2)$$

ρ_s is the density of the solvent, ρ is the density of the rubber phase, m_1 is the quality of the vulcanizate before swelling, m_2 is the quality of the vulcanizate after swelling, m_3 is the quality of the rubber phase.

2.3.3. Mullins Effect Test. The Mullins effect of the vulcanizate was calculated by the cyclic stress-strain experiment [26]. The sample was stretched to the specified strain for the first time and the required energy was recorded as W_1; the same sample was stretched to the same strain for the second time and the required energy was recorded as W_2. Generally speaking, the value of W_2 was less than that of W_1, the phenomenon was called the strain softening or Mullins effect, and the value of W_2/W_1 was used to represent the degree of the Mullins effect. In this work, the same sample was stretched to the specified strain at room temperature for the first, second, third, and fourth times and the required energies were recorded as W_1, W_2, W_3, and W_4, respectively. According to some repetitive experiments, it was found that the value of W_4 was similar to that of W_3. Hence, after the sample was stretched three times, the Mullins effect was stabilized. In order to test the effect of the treatment temperature and storage time on the Mullins effect, after the sample was stretched three times, the sample was stored for 2 h at 60°C, and then the sample was stretched to the same specified strain at room temperature and the required energy was recorded as W_s. The Mullins effects in different cases were calculated using the following formulas:

$$M_1 = \frac{[(W_1(\varepsilon) - W_3(\varepsilon)]}{W_1(\varepsilon)} * 100\% \quad (3)$$

$$M_2 = \frac{[(W_1(\varepsilon) - W_s(\varepsilon)]}{W_1(\varepsilon)} * 100\% \quad (4)$$

M_1 is the degree of the Mullins effect after stretching for three times at room temperature and M_2 is the degree of the Mullins effect after recovery at 60°C for 2 h.

3. Results and Discussion

3.1. The Graft Ratio of PEG on CB. Due to the large difference in polarity between CB and NR, it is difficult for CB to be uniformly dispersed in the rubber matrix, especially when the amount of CB is large, thereby affecting the physical and mechanical properties of the rubber. The difference in polarity between CB and NR can be reduced by the graft modification of CB. Hence, the dispersibility of CB in the rubber matrix is improved significantly, so the physical and mechanical properties of the rubber are improved. The graft ratio of PEG on CB was measured through the TGA curves of CB and GCB (Figure 1). It can be seen from the figure that the mass loss of CB from 30°C to 200°C was 2.1%. It was due to the loss of the water adsorbed on the surface of CB. The mass loss of CB from 200°C to 650°C was 0.92%. It was attributed to the carbonization of the organic components in CB. While for the GCB sample, the mass loss from 200°C to 650°C was 21.23%, which was obviously higher than that of CB. The reason was the PEG was grafted on the surface of CB and it was burned down during the high temperature process, so the graft ratio of PEG on CB could be measured according the TGA curve; the value was about 20%.

3.2. Physical and Mechanical Properties of NR/CB and NR/GCB. Figures 2(a)–2(f) were the physical and mechanical properties of the NR/CB and NR/GCB composites at different filler contents. It can be seen from Figures 2(a)–2(e) that with the increase of the addition amount of CB, the tear strength and shore A hardness were increased gradually, the elongation at break was decreased gradually, and the modulus at 300% and tensile strength of the vulcanizate were first increased and then decreased. When the CB content was 50 phr, the modulus at 300% and tensile strength reached the highest; the values were 6.3 Mpa and 21.2 Mpa, respectively. However, when the CB content was increased to 60 phr, the modulus at 300% and tensile strength were decreased. Since CB was hard to be dispersed in the rubber matrix when the addition amount was large, hence the filler 3D network

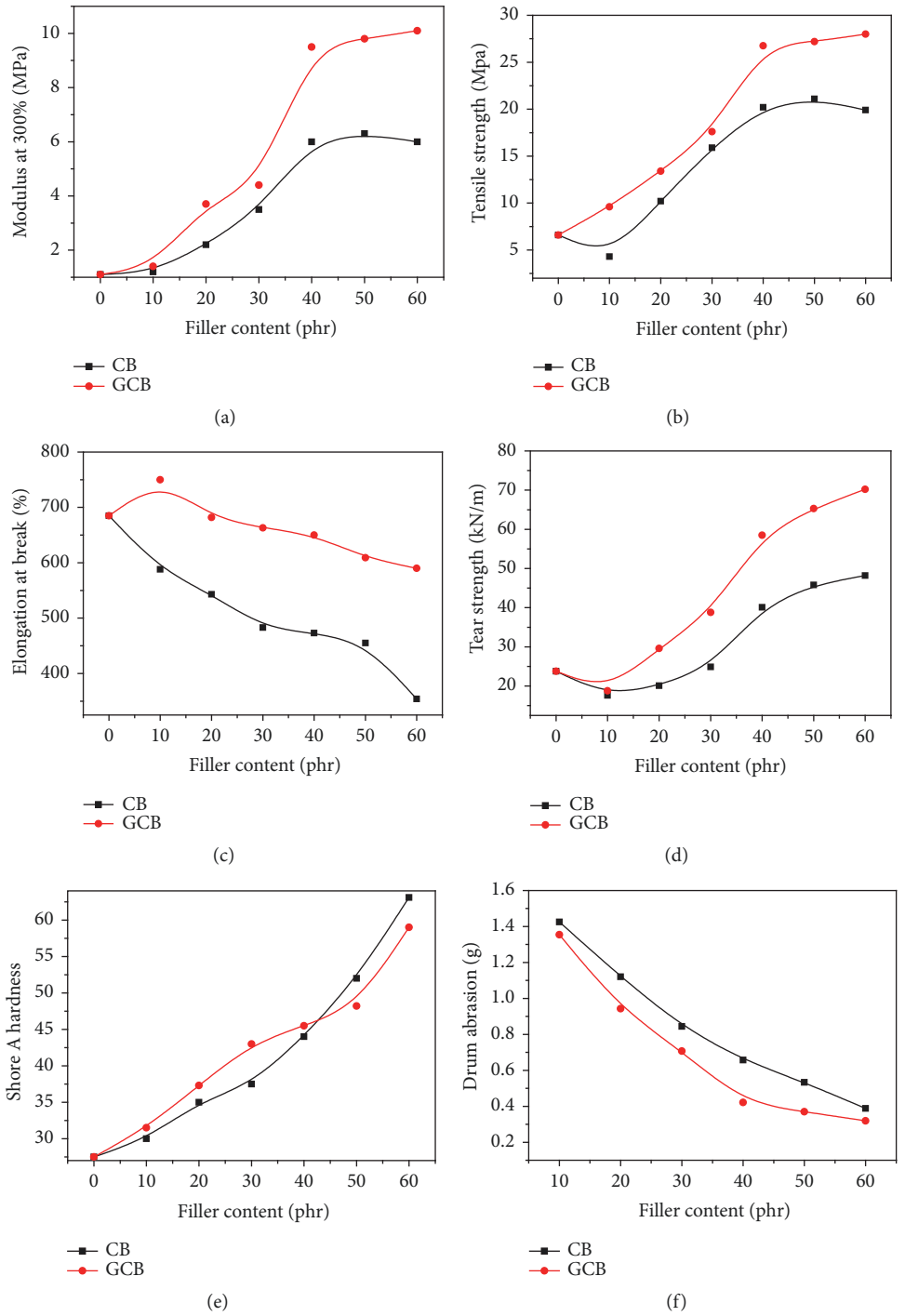

Figure 2: Physical and mechanical properties of NR/CB and NR/GCB.

structure was formed and the aggregation of fillers occurred; the mechanical properties were affected [27].

For the NR/GCB composites, with the increase of the addition amount of GCB, the modulus at 300%, tensile strength, tear strength, and shore A hardness were increased gradually. Unlike the NR/CB composites, the optimum values of the modulus at 300%, tensile strength, tear strength, and shore A hardness were shown when the addition amount of GCB was 60 phr. In addition, the modulus at 300%, tensile strength, elongation at break, and tear strength of NR/GCB were always bigger than that of NR/CB at the same filler content. Compared with the NR/CB composites, the increase rates of the modulus at 300%, tensile strength, elongation at break, and tear strength of NR/GCB were 55.6%, 28.3%, 33.8%, and 42.6%, respectively, when the filler content was 50 phr. It indicated that the addition of GCB could greatly improve the comprehensive physical and mechanical properties of the rubber. Since GCB can be better dispersed in the

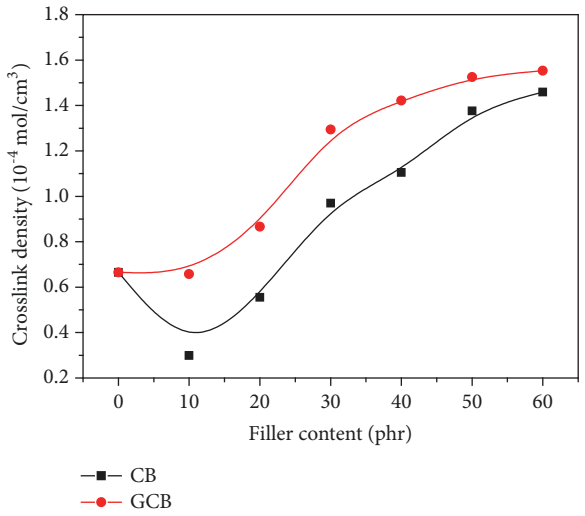

Figure 3: Apparent crosslink densities of NR/CB and NR/GCB.

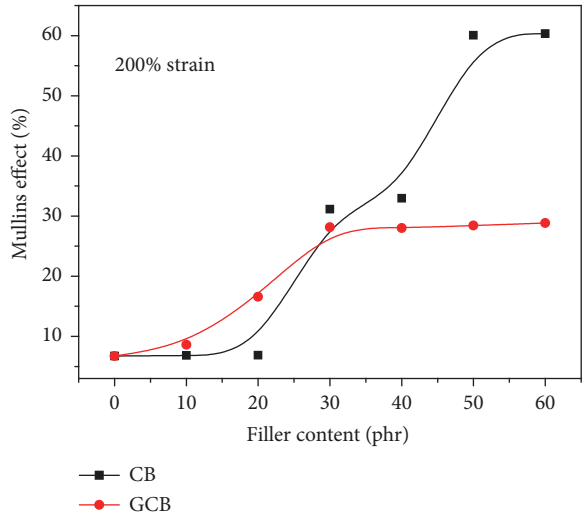

Figure 4: Effect of filler content on Mullins effect of NR/CB and NR/GCB.

rubber matrix, it is less likely to form filler aggregation, and the interaction between GCB and NR was stronger; thereby the physical and mechanical properties were improved.

The wear resistances of NR/CB and NR/GCB with the different filler content were shown in Figure 2(f). With the increase of filler content, the mass of absolute abrasion was decreased gradually, which indicated that the addition of CB or GCB was helpful for improving the wear resistance of NR. The wear resistance of NR/GCB was better than that of NR/CB when the filler content was the same. It is mainly because the NR/GCB has better dispersibility of the filler, larger filler-rubber interaction, and better tear resistance, which is beneficial to hinder the generation of cracks and branch cracks and thus improve the wear resistance [28].

3.3. Apparent Crosslink Densities of NR/CB and NR/GCB. The apparent crosslink density is a representation of the degree of vulcanization, including the chemical crosslinks (polysulfidic, disulfidic, and monosulfidic), as well as the physical crosslinks (rubber-filler interaction and filler-filler network) [29]. The apparent crosslink densities of the NR/CB and NR/GCB vulcanizates at different filler additions were shown in Figure 3. It can be seen from the figure that the apparent crosslink density of the virgin NR vulcanizate was 0.67×10^{-4} mol/cm^3. When the amount of the filler was 10 phr, the apparent crosslink densities of the NR/CB and NR/GCB vulcanizates were decreased to 0.30×10^{-4} mol/cm^3 and 0.66×10^{-4} mol/cm^3, respectively. This is because the N330 carbon black is alkaline, but the accelerator DM is acidic. When CB is added to the rubber system, DM is adsorbed by CB, resulting in a decrease of DM involved in the crosslinking reaction, thereby causing a decrease of the crosslink density. Thereafter, the apparent crosslink densities of the NR/CB and NR/GCB vulcanizates were increased gradually as the amount of filler increased. It is due to more and more rubber-filler interaction and filler-filler network generation with the increase of the filler content [29]. In addition, the apparent crosslink density of NR/GCB was bigger than that of NR/CB at the same amount of filler. This is because GCB has better dispersion in the rubber matrix and thus more filler-rubber interaction was created.

3.4. Effect of Filler Content on Mullins Effect of NR/CB and NR/GCB. The effect of filler content on Mullins effect of NR/CB and NR/GCB composites was shown in Figure 4. It can be seen from the figure that when the sample was stretched after three times at room temperature to make the Mullins effect stability, the degree of Mullins effect of the virgin NR was 6.12%. It is mainly due to the physical disentanglement of rubber molecular chains during the stretching process [11].

In addition, the degree of Mullins effect was increased as the increase of filler addition amount whatever CB or GCB was added to the rubber matrix, but the increase rate in the Mullins effect of adding CB or GCB was different. When the filler addition was below 20 phr, the Mullins effect of NR/GCB was stronger than that of NR/CB. This is because when the amount of filler is smaller than 20 phr, the filler particles are only dispersed in the rubber matrix in isolation and they are unlikely to form a filler-filler 3D network structure [12]. The Mullins effect at this time should be resulted from the disentanglement of rubber molecular chains and destruction of the filler-rubber interaction during the stretching process. In the case of the same amount of rubber matrix, the Mullins effect caused by the disentanglement of rubber molecular chains is similar, so the Mullins effect should be mainly caused by the destruction of the filler-rubber interaction [20]. The destruction is mainly achieved by the rubber molecular chains' shedding and slippage from the surface of fillers. That is, the mechanism of the Mullins effect at low filler content is due to the molecular chains' shedding and slippage mechanism. The dispersion of GCB in the rubber matrix is improved compared to CB, and the compatibility with the rubber matrix is also increased. Hence, more filler-rubber interactions are formed on the microscopic level. These

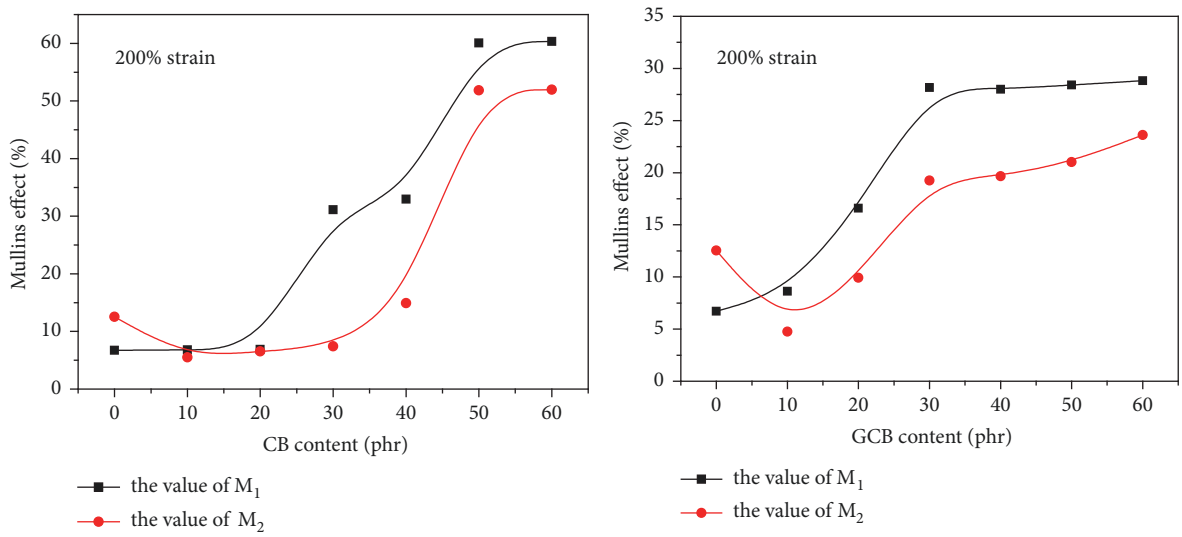

Figure 5: Effect of storage on Mullins effect of NR/CB and NR/GCB.

interactions are destroyed during the stretching process, thus resulting in greater Mullins effect.

However, when the filler addition was over 30 phr, the Mullins effect of NR/CB was stronger than that of NR/GCB. Particularly, when the filler addition was 60 phr, the degree of Mullins effect of NR/GCB was only 47% of that of NR/CB. This is because when the amount of CB is over 30 phr, the filler-filler 3D network structures as a new factor affecting the Mullins effect began to appear, and when the amount of CB reached to 60 phr, these filler-filler 3D network structures were already intense. The filler-filler 3D network structure can be destroyed during the stretching process, thus leading to obvious Mullins effect [23]. Nevertheless, for NR/GCB, fewer filler-filler 3D network structures were generated because GCB has better dispersion in the rubber matrix, so the Mullins effect of NR/GCB was not serious even if the amount of filler was large.

Moreover, when the amount of CB was increased from 40 phr to 50 phr, the Mullins effect rose sharply from 33% to 60%. Some authors called this phenomenon a percolation transition of filler reinforcement [30]. At this time, various isolated filler-filler 3D network structures are connected to each other as a whole. This whole is destroyed during the stretching process, which leads to a sharp rise in the Mullins effect. However, this sudden increase of the Mullins effect did not occur in NR/GCB when the amount of filler was increased from 40 phr to 50 phr, nor did it occur when the amount of filler was increased from 50 phr to 60 phr. It was also shown that CB can be dispersed more uniformly after the graft modification, and it is more difficult to form the filler-filler 3D network structure in the rubber matrix.

3.5. Effect of Storage on Mullins Effect Recovery of NR/CB and NR/GCB. Studying the changes in the Mullins effect during the storage is helpful for further understanding the mechanism of the Mullins effect. According to formula (3) and formula (4), the values of M_1 and M_2 of the NR/CB and NR/GCB samples were calculated and shown in Figures 5(a) and 5(b). It can be seen from the figure that when no filler was added, the value of M_2 of the virgin NR vulcanizate was bigger than that of M_1. According to the previous analysis, the factor that causes the Mullins effect at this time is only the physical disentanglement of rubber molecular chains during the stretching process. So it means that the high temperature treatment is good for re-entanglement of the rubber molecular chains [31]. This is because the activity of the rubber molecular chains rises; thus more re-entanglements are generated during the high temperature treatment process. More re-entanglements are destroyed during the stretching process and lead to bigger Mullins effect.

In addition, when the filler content is from 10 phr to 60 phr, with the increase of the filler content, the Mullins effect was increased gradually during the high temperature treatment process. But the values of M_2 of the NR/CB and NR/GCB samples were smaller than the values of M_1 of their counterparts. It indicates that the high temperature treatment is beneficial for the regeneration of the filler-rubber interaction and filler-filler 3D network structure [31]. However, it is only partial regeneration, and it is hard to return to the initial state of the filler-rubber interaction and filler-filler 3D network structure, so the value of M_2 is always smaller than the value of M_1 at the same filler addition.

3.6. Effect of Storage on Mullins Effect Recovery of NR/CB and NR/GCB. The phenomenological theory is a research method of rubber elasticity theory. The Mooney-Rivlin equation is one of the most commonly used expressions in the phenomenological theory [32], which is shown as follows:

$$\frac{\sigma}{\lambda - \lambda^{-2}} = 2C_{10} + 2C_{01}\left(\frac{1}{\lambda}\right) \quad (5)$$

In formula (5), σ is the stress, $\sigma/(\lambda - \lambda^{-2})$ is defined as the reduced stress, λ is the strain along the stress direction, and C_{10} and C_{01} are constants without clear physical meaning [33].

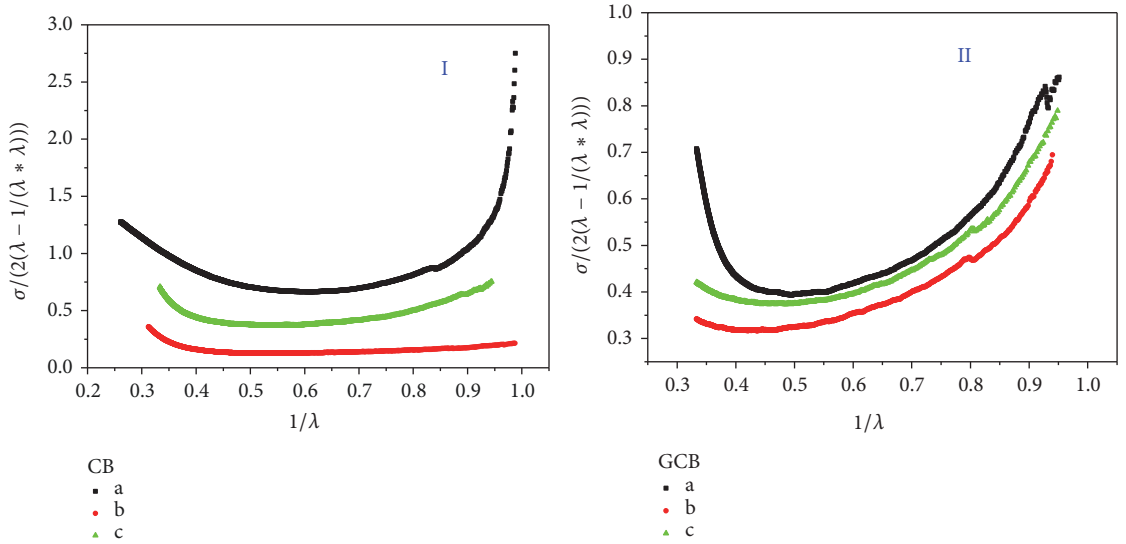

Figure 6: Mooney curves of NR/CB and NR/GCB at different conditions.

According to the formula (5), the stress-strain curve of a sample can be transferred to the Mooney-Rivlin curve (hereinafter referred to as Mooney curve). The Mooney curves of the sample being directly stretched to break, the sample being repeatedly stretched to 200% strain for 3 times and then stretched to break, and the sample being repeatedly stretched to 200% strain for 3 times and then placed in an oven at 60°C for 2 h and then stretched to break were shown in Figure 6. The CB or GCB filler content was 60 phr in this experiment. According to the formula (5), the ideal Mooney curve should be a straight line. But it can be seen from the Figure 6 that the real Mooney curve was not a straight line. The reduced stress $\sigma/(\lambda - \lambda^{-2})$ first fell and then rose with the increase of the strain λ (look from the right to left of the curves), presented a "U-shaped" trend. The difference of the ideal Mooney curve and real Mooney curve reflects two additive effects during the stretching process: (1) in the low strain region (the right side of the curve), the reduced stress decrease with the increase of strain is due to the Mullins effect of the material. (2) In the high strain region (the left side of the curve), the reduced stress increases with the increase of strain is because of the non-Gaussian behavior of the polymer chains. The upturning phenomenon of the reduced stress in high strain region indicates that the polymer chains are stretched to their ultimate elongation [33].

The Mooney curve of the NR/CB sample being directly stretched to break (Figure 6(I-a)) showed a very obvious decline in the low strain region. It indicated an obvious Mullins effect occurred. However, when the sample was repeatedly stretched to 200% strain for 3 times and then stretched to break, the Mooney curve in the low strain region (Figure 6(I-b)) did not show a significant decline. This is because the repeated stretching leads to the disentanglement of rubber molecular chains, the destruction of the filler-rubber interaction, and filler-filler 3D network structure, thus leading to the decrease of the Mullins effect. The destruction of the filler-filler 3D network structure should be the main cause of the decline of the Mullins effect. When the sample was treated in an oven at 60°C for 2 h after it has been stretched for 3 times, the Mooney curve in the low strain region (Figure 6(I-c)) presented a relatively significant decline compared to Figure 6(I-b). The reason is that the rubber molecular chains are re-entangled; the filler-rubber interaction and filler-filler 3D network structure are regenerated during the high temperature treatment process. In addition, Figure 6(I-b) curve was always below Figure 6(I-a) curve and Figure 6(I-c) curve was always above Figure 6(I-b) curve. It meant that the stress required for Figure 6(I-b) curve was smaller than that of Figure 6(I-a) curve and the stress required for Figure 6(I-c) curve was bigger than that of Figure 6(I-b) curve at the same strain. It also indicates that the repeated stretching leads to the disentanglement of rubber molecular chains, the destruction of the filler-rubber interaction and filler-filler 3D network structure; the high temperature treatment is helpful for the re-entanglement of rubber molecular chains and the regeneration of the filler-rubber interaction and filler-filler 3D network structure.

The trend of the Mooney curves of the NR/GCB samples under the three different stretching conditions (Figure 6(I-a, b, c)) was similar to that of the NR/CB samples (Figure 6(II-a, b, c)), but there were some differences that had to be mentioned. First, when λ^{-1} was changed from 1.0 to 0.9, the value of $\sigma/2(\lambda - \lambda^{-2})$ of NR/CB was changed from 2.72 to 0.98. However, the value of $\sigma/2(\lambda - \lambda^{-2})$ of NR/GCB was changed from 0.86 to 0.76, which was obviously smaller than that of NR/CB. This also showed that the Mullins effect of NR/GCB was lower when the filler content was 60 phr. Second, whatever being directly stretched to break (Figure 6(II-a)), being repeatedly stretched to 200% strain for 3 times and then stretched to break (Figure 6(II-b)), and being repeatedly stretched to 200% strain for 3 times and then placed in an oven at 60°C for 2 h and then stretched to break (Figure 6(II-c)), the Mooney curves of the samples in the low strain region all presented a relatively significant decline. It

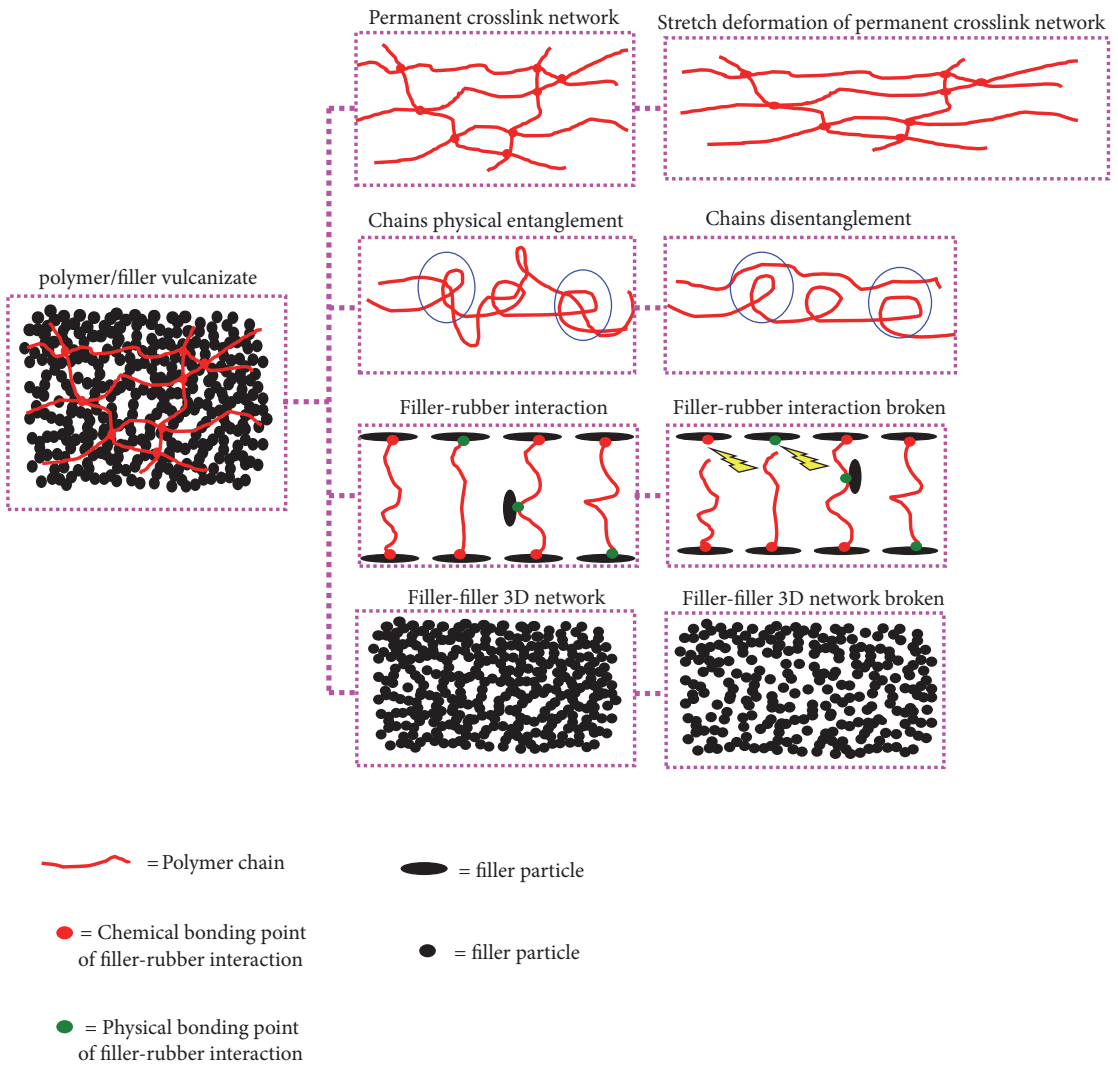

Figure 7: Filler reinforcement and Mullins effect mechanisms.

illustrates that the reason causing the Mullins effect of NR/CB and the Mullins effect of NR/GCB is different. The main reason causing the Mullins effect of NR/CB is the destruction of the filler-filler 3D network structure, while the main reason causing the Mullins effect of NR/GCB is the destruction of the filler-rubber interaction.

3.7. Filler Reinforcement and Mullins Effect Mechanisms. Combining the previous analyses and drawing on Roozbeh's viewpoint [12], the polymer/filler vulcanizate system can be divided into four parts: the permanent crosslink network of polymer chains crosslinked by the vulcanizing agents (Figure 7, row 1), the physical entanglement network of polymer chains (Figure 7, row 2), the filler-rubber interaction system (Figure 7, row 3), and the filler-filler 3D network system (Figure 7, row 4). The combined action of these four parts constitutes the reinforcing mechanisms of polymer/filler vulcanizate system, and the Mullins effect mechanisms are also caused by the changes of these four parts at different situations. The filler reinforcement and Mullins effect mechanisms are analyzed as follows:

(1) For the virgin polymer vulcanizate system with no filler, the strength of the vulcanizate is derived from the orientation and fracture of the polymer permanent crosslink network and the crystallization owing to the orientation of the polymer chains during the stretching process [34]. While the Mullins effect should be mainly attributed to the disentanglement of the polymer chains during the stretching process (Figure 7, row 2), and the Mullins effect caused by this disentanglement is weak.

(2) For the polymer vulcanizate system with low filler content, the orientation and fracture of the polymer permanent crosslink network and the crystallization can result in the strength improvement; the filler-rubber interaction is another factor to lead to the strength improvement of the vulcanizate. The external force acting on the rubber matrix is transferred to the rigid filler through the filler-rubber bonding points, so the strength of the vulcanizate is improved. The filler-rubber bonding points are including the filler-rubber physical bonding points connected through the noncovalent bonds and filler-rubber chemical bonding points connected through the covalent bonds. The Mullins

effect should be mainly attributed to the destruction of the filler-rubber physical bonding points and chemical bonding points and the slippage of the polymer chains on the surface of the fillers (Figure 7, row 3). Under the same filler content, the better the dispersion of the filler in the rubber matrix and the better the compatibility with the rubber matrix exhibit, the more filler-rubber interaction points are formed. The more filler-rubber interaction points are destroyed during the stretching process, the more obvious Mullins effect. This is why the Mullins effect of NR/GCB is stronger than that of NR/CB when the filler is below 20 phr.

(3) For the polymer vulcanizate system with high filler content, the more filler-rubber interaction points are formed because of the bigger filler content; thus the strength is improved. But when the addition amount of the filler is too big, the filler-filler 3D network structure will be formed in the rubber matrix, thus causing the filler agglomeration. The agglomeration of the filler in the rubber matrix causes the stress concentration, thereby resulting in a decrease in the tensile strength. This is why the tensile strength of the rubber is lowered when the amount of CB is increased from 50 phr to 60 phr. The Mullins effect at this time should be mainly ascribed to the destruction of the filler-filler 3D network structure during the stretching process (Figure 7, row 4). The Mullins effect resulted from the destruction of the filler-filler 3D network being greater than that caused by the destruction of the filler-rubber interaction. It can be seen from Figure 4.

4. Conclusions

(1) About 20% polyethylene glycol of the total mass was grafted on the surface of the carbon black, thus the dispersion of the carbon black in the rubber matrix and the compatibility with the rubber matrix were improved, thereby the comprehensive performance being increased.

(2) The degree of Mullins effect was increased with the increase of filler. However, when the filler addition was below 20 phr, the Mullins effect of NR/GCB was stronger than that of NR/CB. When the filler addition was over 30 phr, the Mullins effect of NR/CB was stronger than that of NR/GCB. The degree of Mullins effect of NR/GCB was only 47% of that of NR/CB when the filler addition was 60 phr. The Mullins effect was increased gradually during the high temperature treatment process because of the re-entanglement of the rubber molecular chains, regeneration of the filler-rubber interaction and filler-filler 3D network structure.

(3) For the virgin polymer vulcanizate system with no filler, the Mullins effect should be mainly attributed to the disentanglement of the polymer chains during the stretching process. For the polymer vulcanizate system with low filler content, the Mullins effect should be mainly ascribed to the destruction of the filler-rubber interaction during the stretching process. For the polymer vulcanizate system with high filler content, the Mullins effect at this time should be mainly resulted from the destruction of the filler-filler 3D network structure during the stretching process.

Data Availability

The data used to support the findings of this study are included within the article.

Conflicts of Interest

The authors declare that they have no conflicts of interest regarding the publication of this paper.

Acknowledgments

This work was supported by the Natural Science Foundation of Guangdong Province (2017A030310663, 2018A030307018, and 2018A0303070003), the Foundation of Guangdong Province Rubber/Plastic Materials Preparation & Processing Engineering Technology Development Centre (2015B090903083), Distinguished Young Talents in Higher Education of Guangdong (517053), Maoming Science and Technology Project (517055), and Guangdong Research Center for Unconventional Energy Engineering Technology (GF2018A005).

References

[1] X. Fan, H. Xu, Q. Zhang, D. Xiao, Y. Song, and Q. Zheng, "Insight into the weak strain overshoot of carbon black filled natural rubber," *Polymer Journal*, vol. 167, pp. 109–117, 2019.

[2] P. Yuvaraj, J. R. Rao, N. N. Fathima, N. Natchimuthu, and R. Mohan, "Complete replacement of carbon black filler in rubber sole with CaO embedded activated carbon derived from tannery solid waste," *Journal of Cleaner Production*, vol. 170, pp. 446–450, 2018.

[3] B. Sripornsawat, S. Saiwari, and C. Nakason, "Thermoplastic vulcanizates based on waste truck tire rubber and copolyester blends reinforced with carbon black," *Waste Management*, vol. 79, pp. 638–646, 2018.

[4] X. Du, Y. Zhang, X. Pan, F. Meng, J. You, and Z. Wang, "Preparation and properties of modified porous starch/carbon black/natural rubber composites," *Composites Part B: Engineering*, vol. 156, pp. 1–7, 2019.

[5] J. Chen, Y. Maekawa, M. Yoshida, and N. Tsubokawa, "Radiation grafting of polyethylene onto conductive carbon black and application as a novel gas sensor," *Polymer Journal*, vol. 34, no. 1, pp. 30–35, 2002.

[6] N. Tsubokawa, T. Satoh, M. Murota, S. Sato, and H. Shimizu, "Grafting of hyperbranched poly(amidoamine) onto carbon black surfaces using dendrimer synthesis methodology," *Polymers for Advanced Technologies*, vol. 12, no. 10, pp. 596–602, 2001.

[7] R. Richner, S. Müller, and A. Wokaun, "Grafted and crosslinked carbon black as an electrode material for double layer capacitors," *Carbon*, vol. 40, no. 3, pp. 307–314, 2002.

[8] Q. Yang, L. Wang, W. Xiang, J. Zhou, and J. Li, "Grafting polymers onto carbon black surface by trapping polymer radicals," *Polymer Journal*, vol. 48, no. 10, pp. 2866–2873, 2007.

[9] D. Julie, F. Bruno, and G. Pierre, "A review on the Mullins effect," *European Polymer Journal*, vol. 45, no. 3, pp. 601–612, 2009.

[10] H. Bouasse and Z. Carriere, "Sur les courbes de traction du caoutchouc vulcanize," *Annales de la faculte des sciences de Toulouse*, vol. 5, no. 3, pp. 257–283, 1903.

[11] L. Mullins, "Effect of stretching on the properties of rubber," *Rubber Chemistry and Technology*, vol. 21, no. 2, pp. 281–300, 1948.

[12] R. Dargazany and M. Itskov, "A network evolution model for the anisotropic Mullins effect in carbon black filled rubbers," *International Journal of Solids and Structures*, vol. 46, no. 16, pp. 2967–2977, 2009.

[13] E. B. da Rocha, F. N. Linhares, C. F. Gabriel, A. M. de Sousa, and C. R. Furtado, "Stress relaxation of nitrile rubber composites filled with a hybrid metakaolin/carbon black filler under tensile and compressive forces," *Applied Clay Science*, vol. 151, pp. 181–188, 2018.

[14] Q. Liu, K. Zhang, X. Zhang, and Z. Wang, "Strengthening effect of mullins effect of high- density polyethylene/ethylene–propylene–diene terpolymer thermoplastic vulcanizates under compression mode," *Journal of Thermoplastic Composite Materials*, vol. 31, no. 10, pp. 1310–1322, 2017.

[15] A. Ivanoska-Dacikj, G. Bogoeva-Gaceva, S. Rooj, S. Wießner, and G. Heinrich, "Fine tuning of the dynamic mechanical properties of natural rubber/carbon nanotube nanocomposites by organically modified montmorillonite: a first step in obtaining high-performance damping material suitable for seismic application," *Applied Clay Science*, vol. 118, pp. 99–106, 2015.

[16] J. Diani, M. Brieu, and P. Gilormini, "Effect of filler content and crosslink density on the mechanical properties of carbon-black filled SBRs," in *Proceedings of the 10th European Conference on Constitutive Models for Rubber, ECCMR X 2017*, pp. 3–10, Balkema, August 2017.

[17] C. Matthew and S. A. D. F. Davide, "Reversibility of the Mullins effect for extending the life of rubber components," *Plastics, Rubber and Composites*, vol. 5, pp. 24–31, 2018.

[18] R. Yang, Y. Song, and Q. Zheng, "Payne effect of silica-filled styrene-butadiene rubber," *Polymer Journal*, vol. 116, pp. 304–313, 2017.

[19] S. K. Srivastava and Y. K. Mishra, "Nanocarbon reinforced rubber nanocomposites: Detailed insights about mechanical, dynamical mechanical properties, payne, and mullin effects," *Nanomaterials*, vol. 8, no. 11, pp. 945–3021, 2018.

[20] F. Bueche, "Molecular basis for the mullins effect," *Journal of Applied Polymer Science*, vol. 4, no. 10, pp. 107–114.

[21] R. Houwink, "Slipping of molecules during the deformation of reinforced rubber," *Rubber Chemistry and Technology*, vol. 29, no. 3, pp. 888–893, 1956.

[22] M. A. Johnson and M. F. Beatty, "A constitutive equation for the Mullins effect in stress controlled uniaxial extension experiments," *Continuum Mechanics and Thermodynamics*, vol. 5, no. 4, pp. 301–318, 1993.

[23] G. Kraus, C. W. Childers, and K. W. Rollmann, "Stress softening in carbon black reinforced vulcanizates. strain rate and temperature effects," *Rubber Chemistry and Technology*, vol. 39, no. 5, pp. 1530–1543, 1966.

[24] G. R. Hamed and S. Hatfield, "On the role of bound rubber in carbon-black reinforcement," *Rubber Chemistry and Technology*, vol. 62, no. 1, pp. 143–156, 1989.

[25] T. A. Vilgis, J. Sommer, and G. Heinrich, "Swelling and fractal heterogeneities in networks," *Macromolecular Symposia*, vol. 93, no. 1, pp. 205–212, 1995.

[26] M. Cheng and W. Chen, "Experimental investigation of the stress–stretch behavior of EPDM rubber with loading rate effects," *International Journal of Solids and Structures*, vol. 40, no. 18, pp. 4749–4768, 2003.

[27] J. Fröhlich, W. Niedermeier, and H.-D. Luginsland, "The effect of filler-filler and filler-elastomer interaction on rubber reinforcement," *Composites Part A: Applied Science and Manufacturing*, vol. 36, no. 4, pp. 449–460, 2005.

[28] H. H. Hassan, E. Ateia, N. A. Darwish, S. F. Halim, and A. K. Abd El-Aziz, "Effect of filler concentration on the physico-mechanical properties of super abrasion furnace black and silica loaded styrene butadiene rubber," *Materials and Corrosion*, vol. 34, pp. 533–540, 2012.

[29] J. J. Brennan and D. H. Lambert, "Rubber—black interaction influence on cure level of vulcanizates," *Rubber Chemistry and Technology*, vol. 45, no. 1, pp. 94–105, 1972.

[30] J. Zhou, Y. Song, Q. Zheng, Q. Wu, and M. Zhang, "Percolation transition and hydrostatic piezoresistance for carbon black filled poly(methylvinylsilioxane) vulcanizates," *Carbon*, vol. 46, no. 4, pp. 679–691, 2008.

[31] G. Bohm, W. Tomaszewski, W. Cole, and T. Hogan, "Furthering the understanding of the non linear response of filler reinforced elastomers," *Polymer Journal*, vol. 51, no. 9, pp. 2057–2068, 2010.

[32] N. Kumar and V. V. Rao, "Hyperelastic Mooney-Rivlin model: determination and physical interpretation of material constants," *International Journal of Mechanical Engineering*, vol. 6, no. 1, pp. 43–46, 2016.

[33] W. Fu and L. Wang, "Research on Payne effect of natural rubber reinforced by graft-modified silica," *Journal of Applied Polymer*, vol. 133, no. 36, pp. 43891–43898, 2016.

[34] J. Chenal, C. Gauthier, L. Chazeau, L. Guy, and Y. Bomal, "Parameters governing strain induced crystallization in filled natural rubber," *Polymer Journal*, vol. 48, no. 23, pp. 6893–6901, 2007.